

2012

Material Characterization and Computational Simulation of Steel Foam for Use in Structural Applications

Brooks H. Smith

University of Massachusetts Amherst, SmithBH@Members.ASCE.org

Follow this and additional works at: <http://scholarworks.umass.edu/theses>

 Part of the [Structural Engineering Commons](#), and the [Structural Materials Commons](#)

Smith, Brooks H., "Material Characterization and Computational Simulation of Steel Foam for Use in Structural Applications" (2012).

Masters Theses 1911 - February 2014. 813.

<http://scholarworks.umass.edu/theses/813>

This thesis is brought to you for free and open access by the Dissertations and Theses at ScholarWorks@UMass Amherst. It has been accepted for inclusion in Masters Theses 1911 - February 2014 by an authorized administrator of ScholarWorks@UMass Amherst. For more information, please contact scholarworks@library.umass.edu.

**MATERIAL CHARACTERIZATION AND COMPUTATIONAL SIMULATION OF STEEL FOAM FOR USE
IN STRUCTURAL APPLICATIONS**

A Thesis Presented

By

BROOKS HOLDEN SMITH

Submitted to the Graduate School of the
University of Massachusetts Amherst in partial fulfillment
of the requirements for the degree of

MASTER OF SCIENCE IN CIVIL ENGINEERING

May 2012

Civil and Environmental Engineering
Structural Engineering

© Copyright by Brooks Holden Smith 2012
All Rights Reserved

**MATERIAL CHARACTERIZATION AND COMPUTATIONAL SIMULATION OF STEEL FOAM FOR USE
IN STRUCTURAL APPLICATIONS**

A Thesis Presented

by

BROOKS HOLDEN SMITH

Approved as to style and content by:

Sanjay R. Arwade, Chair

Scott A. Civjan, Member

Richard N. Palmer, Department Head
Civil and Environmental Engineering

DEDICATION

This thesis is dedicated to my parents,
Cotten and Phyllis Smith

ACKNOWLEDGMENTS

I gratefully acknowledge the tireless assistance of my adviser, Sanjay Arwade, for helping me far beyond just regular meetings, but also getting his hands dirty in the lab and answering late-night e-mails. I would also like to thank the entire Steel Foam research team, including Jerry Hajjar at Northeastern University, as well as both Ben Schaefer and Stefan Szyniszewski at Johns Hopkins University. Our weekly meetings have helped supply a constant influx of fresh perspectives and new ideas. Additionally, my undergraduate assistants, Marc Fernandez and Michelle Fiorello, have provided useful help through various stages of this research.

For putting up with me as I've been so often working and never ceasing to ramble on talking about my research, I greatly thank my parents, friends, and housemates. They have all not only put up with me, but also provided much-needed moral support along the way.

My thesis committee, including Scott Civjan and Sanjay Arwade, have somehow managed to read through this entire thesis and stay awake during my defense (or even if they don't); thank you very much. None of this would be happening if it weren't for the assistance of Jodi Ozdarski and her help in navigating the intricacies of the university bureaucracy, and for this I am very grateful.

Of course, no research could happen without funding to perform it. For that, I would like to thank the National Science Foundation for providing the grant money, and the University of Massachusetts, Amherst for partially distributing the money to myself. NSF grants CMMI #1000334, #1000167, and #0970059 were awarded to this project.

ABSTRACT

MATERIAL CHARACTERIZATION AND COMPUTATIONAL MODELING OF STEEL FOAM FOR USE IN STRUCTURAL APPLICATIONS

MARCH 2012

BROOKS HOLDEN SMITH, A.B., DARTMOUTH COLLEGE

B.E., THAYER SCHOOL OF ENGINEERING AT DARTMOUTH COLLEGE

M.S., UNIVERSITY OF MASSACHUSETTS AMHERST

Directed by: Professor Sanjay R. Arwade

Cellular metals made from aluminum, titanium, or other metals are becoming increasingly popular for use in structural components of automobiles, aircraft, and orthopaedic implants. Civil engineering applications remain largely absent, primarily due to poor understanding of the material and its structural properties. However, the material features a high stiffness to weight ratio, excellent energy dissipation, and low thermal conductivity, suggesting that it could become a highly valuable new material in structural engineering. Previous attempts to characterize the mechanical properties of steel foam have focused almost exclusively upon uniaxial compression tests, both in experimental research and in computational simulations. Further, computational simulations have rarely taken the randomness of the material's microstructure into account and have instead simplified the material to a regular structure. Experimental tests have therefore been performed upon both hollow spheres and PCM steel foams to determine compressive, tensile, and shear properties. Computational simulations which accurately represent the randomness within the microstructure have been validated against these experimental results and then used to simulate other material scale tests. Simulated test matrices have determined macroscopic system sensitivity to various material and geometrical parameters.

TABLE OF CONTENTS

	Page
ACKNOWLEDGMENTS.....	v
ABSTRACT.....	vi
LIST OF TABLES.....	xii
LIST OF FIGURES.....	xv
CHAPTER	
1. INTRODUCTION.....	1
2. BACKGROUND AND LITERATURE REVIEW.....	3
2.1 Manufacturing Processes.....	3
2.1.1 Hollow Spheres.....	5
2.1.2 Gasar / Lotus-Type.....	5
2.1.3 Powder Metallurgy.....	6
2.1.4 PCM.....	7
2.1.5 Other Methods.....	7
2.2 Effective Macroscopic Properties.....	9
2.2.1 Experimental Material Properties.....	10
2.2.2 Modeling of Mechanical Properties.....	14
2.2.2.1 Computational Microstructure Models.....	15
2.2.2.2 Mathematical Models with Microstructural Parameters.....	18
2.3 Usage in Structural Engineering.....	22
2.3.1 Plasticity Based Models.....	23
2.3.2 Structural Applications.....	24
3. EXPERIMENTAL TESTS.....	29
3.1 Testing Standards.....	29
3.2 Testing Procedure.....	30

3.2.1 Microscopy.....	32
3.2.1.1 Hollow Spheres Foam.....	33
3.2.1.2 PCM Foam	36
3.2.2 Compression Testing.....	39
3.2.2.1 Hollow Spheres Foam.....	39
3.2.2.2 PCM Foam	41
3.2.3 Tension Testing.....	42
3.2.3.1 Hollow Spheres Foam.....	42
3.2.3.2 PCM Foam	44
3.2.4 Shear Testing	46
3.3 Results	49
3.3.1 Microscopy.....	50
3.3.1.1 Hollow Spheres Foam.....	51
3.3.1.2 PCM Foam	51
3.3.2 Compression Testing.....	52
3.3.2.1 Hollow Spheres Foam.....	52
3.3.2.2 PCM Foam	64
3.3.3 Tension Testing.....	67
3.3.3.1 Hollow Spheres Foam.....	68
3.3.3.2 PCM Foam	71
3.3.4 Shear Testing	74
3.3.5 Discussion of Results	77
4. COMPUTATIONAL SIMULATIONS WITH RANDOM MICROSTRUCTURES	80
4.1 Introduction and Motivation.....	80
4.2 Computer Program.....	81

4.2.1 Coding and User Interface.....	82
4.2.2 Code Segments	85
4.3 Finite Element Analysis.....	87
4.3.1 Geometry Generation.....	87
4.3.1.1 Hollow Spheres Geometry.....	89
4.3.1.2 General Closed-Cell Geometry.....	92
4.3.2 Simulation	94
4.3.2.1 Compression and Tension Testing.....	95
4.3.2.2 Shear Testing.....	97
4.3.2.3 Multiaxial Testing.....	98
4.3.3 Post-Processing.....	99
4.3.4 Summary of Assumptions	100
4.4 Results	102
4.4.1 Hollow Spheres Tests.....	103
4.4.1.1 Initial Validation.....	103
4.4.1.2 Validation to Experimental Results	105
4.4.1.3 Post-Yield Behavior Simulation Matrix	108
4.4.1.4 Structural Randomness Analysis.....	112
4.4.1.5 Sensitivity Analysis for Compression Tests.....	125
4.4.2 Gasar Tests	130
4.4.2.1 Initial Validation.....	130
4.4.2.2 Post-Yield Behavior Simulation Matrix	132
4.4.3 PCM Tests.....	136
4.4.3.1 Validation to Experimental Results	137
5. SUGGESTED FUTURE WORK.....	139

5.1 Introduction.....	139
5.2 Experimental	140
5.2.1 Develop New Testing Standards for Metal Foams.....	141
5.2.2 More Testing Types.....	142
5.2.2.1 Connection Testing.....	142
5.2.2.2 Cyclic Testing.....	144
5.2.2.3 Strain Rate Testing.....	145
5.2.2.4 Creep Testing.....	146
5.2.2.5 Multiaxial Testing.....	146
5.2.2.6 Non-Mechanical Testing.....	147
5.2.3 Testing Different Steel Foams.....	147
5.3 Computational.....	148
5.3.1 New Features.....	149
5.3.1.1 Densification Tests.....	150
5.3.1.2 Strain Rate Testing.....	150
5.3.1.3 Thermal Testing.....	151
5.3.1.4 Connection Testing.....	151
5.3.1.5 Cyclic Testing.....	152
5.3.1.6 Creep Testing.....	154
5.3.1.7 Torsional Shear Testing.....	154
5.3.1.8 Other Non-Mechanical Testing.....	156
5.3.2 Geometry Improvements.....	156
5.3.3 Simulation Validation	157
5.3.4 Simulation Test Matrices	159
6. CONCLUSIONS	161

APPENDIX: METAL FOAMS SIMULATOR USER GUIDE	164
BIBLIOGRAPHY	191

LIST OF TABLES

Table	Page
1: The several possible manufacturing methods for steel foam, including basic resultant foam characteristics.....	4
2: Material properties extracted from selected publications.....	12
3: Non-mechanical material properties for steel foam, including thermal, acoustic, and permeability, for optimal manufacturing methods of steel foam.	14
4: Microstructural representations of steel foam used in selected published literature.....	17
5: Equations for mechanical properties of metal foams as set by Gibson and Ashby (2000)	18
6: Experimentally derived expressions for mechanical properties of elastic modulus (first table) and compressive yield (second table). t = sphere thickness, R = outer radius of hollow sphere, r = radius of joined metal between spheres.....	20
7: Prototype and production structural applications for metal foams from selected literature.....	25
8: Prototype and production non-structural applications of metal foams.....	28
9: Table of comparable American and international testing standards for metal foams.....	30
10: Table of the three types of compression tests performed upon hollow spheres foam.	40
11: Summary table of all experimental tests performed.....	50
12: Results of hollow spheres microscopy study, showing mean and standard deviation of values in each sample.	51
13: Results of PCM microscopy study, showing mean and standard deviation of values in each sample.....	52
14: Summary of all compressive hollow spheres properties.....	64
15: Summary of all compressive properties of PCM foam.....	67
16: Summary of all hollow spheres tensile properties.	71
17: Summary of all PCM tensile properties.....	74
18: Summary of hollow spheres shear properties.	77
19: Probabilistic distributions assumed for input parameters in hollow spheres geometries.....	91

20: Probabilistic distributions assumed for general closed-cell input parameters.....	94
21: Table of major assumptions made internally within the Metal Foams Simulator.....	101
22: Input Parameters used in the hollow spheres initial validation simulations.....	103
23: Input parameters used in hollow spheres validations to experimental results.....	105
24: Input parameters for hollow spheres post-yield behavior simulation matrix.....	108
25: Input parameters used in hollow spheres structural randomness analysis.	112
26: Overall summary of all means and variances of elastic modulus for all representations of hollow spheres foams.....	123
27: Input parameters used in hollow spheres sensitivity analysis for compression tests.....	125
28: Normalized results data from sensitivity analysis, normalized to the base value.....	128
29: First-order central difference results from sensitivity analysis, normalized about the base value shown.....	130
30: Input parameters used in gasar initial validation simulations.....	130
31: Gasar foam validation using gasar experimental values. Partially adapted from research by Ikeda, Aoki, and Nakajima (2007).....	132
32: Input parameters used in the gasar post-yield behavior simulation matrix.....	132
33: Input parameters used in the PCM validations to experimental results.....	137
34: Comparison of elastic modulus and yield stress values for PCM validation simulations.....	138
35: Prioritized list of recommended work which could be immediately performed as a follow-up project to this thesis.....	140
36: Prioritized list of longer-term tasks for encouraging industry to begin using steel foams.....	140
37: System requirements for the Metal Foams Simulator.....	165
38: Input variables for the Metal Foam Simulator, including possible values and an explanation of their meaning.....	166
39: Example of working input parameter sets for a general closed-cell and a hollow spheres simulation.....	169
40: Files required for resumption of Simulator runs.....	175

41: Table of variables present in the Simulator's [name]_results.mat file.....	176
42: Table of results graphs generated by the Simulator.....	177
43: Table of exit codes issued by the Metal Foams Simulator, including their meanings and troubleshooting references.....	179

LIST OF FIGURES

Figure	Page
1: Typical stress-strain curve for steel foam in uniaxial compression.....	10
2: Compressive yield strength versus normalized elastic modulus of various types of steel foams, as reported by various researchers (see Table 2). The Gibson & Ashby model's minimum and maximum values are also displayed (see section 2.2.2.2). The lower graph zooms in upon the open-celled foams in the top graph.	13
3: A single tetrakaidecahedron. These shapes stack without gaps, so conglomerations of tetrakaidecahedra are used in simple computational models.	16
4: Comparison of available experimental data with Gibson and Ashby expressions of Table 5. Blue lines indicate Gibson & Ashby expressions with leading coefficients equal to minimum, maximum, and central value.	19
5: Graph comparing the alternative mathematical models for compressive yield with the model of Gibson and Ashby. The graph for alternative elastic modulus models shows similar patterns.	21
6: Sample image of a sphere diameter microscopy measurement.....	34
7: Sample image of a weld size microscopy measurement.....	35
8: Sample image of a sphere wall thickness microscopy measurement.	36
9: Macro photograph of measuring the length of a pore on the PCM material. The full 37mm height of the material is shown.	37
10: Microscopy image of a PCM face cut parallel to pores.....	37
11: Microscopy images depicting how void diameters were measured. The top image shows a tensile fracture surface, while the bottom shows a milled surface. The scale is the same on both images.	38
12: Image of a full-size hollow spheres specimen during a compression test.	41
13: Dimensioned drawing of a hollow spheres tension specimen (all dimensions in mm).	43
14: Photo of epoxying a tension platen. The testing specimen with slot cut into it is located immediately below the platen.	44
15: Dimensioned drawing of a PCM tension specimen (all dimensions in mm).....	45
16: Specimen of PCM foam mounted in the wedge grips and ready for tension testing.....	46

17: Drawing of shear testing apparatus specified in ISO 1922, the shear testing standard for rigid plastics (Image from ISO 1922). All dimensions shown are in mm.....	47
18: The shear testing apparatus, based upon ISO 1922, loaded with a sample and ready for testing. The extensometer is attached in the upper right.	48
19: An elastic unloading modulus test upon a normal-height specimen in progress.	53
20: Stress-strain curve of multiple unloadings test showing the full testing regime (top), where the overlaid black box is the region for which a zoomed view is shown below.....	55
21: Elastic unloading modulus as calculated manually from each unloading shown in the stress-strain curves of Figure 20.	57
22: Validation for the accuracy of crosshead-based stress-strain curves, demonstrating fair accuracy after a strain of about 0.05.	58
23: Engineering stress-strain curve from densification tests.	59
24: A sequence of images of the steel foam during the test at various strains (from left to right then top to bottom: 0.0, 0.10, 0.35, 0.50, 0.65, 0.85). Note that photos use a wide-angle lens; the platens did not rotate during compression.....	59
25: A densified sample which experienced asymmetric smooching.....	60
26: Image of Poisson's ratio compressive test in progress. The extensometer blades are held against the material by pressure	61
27: Engineering Poisson's ratio versus crosshead strain.	62
28: The three stages of specimens used to test the base metal yield strength of the hollow spheres foam.....	64
29: Images of two PCM compression specimens which failed in brittle fractures: longitudinal orientation test #4, performed upon the Tinius Olson testing machine (left), and transverse orientation test #2, performed upon the Instron 3369 testing machine (right). Block arrows indicate the direction in which load was applied.	65
30: Uniaxial compression stress-strain curves with pores oriented longitudinally (left) and transversely (right) to the direction of loading. All tests were performed on an Instron 3369 machine, except test #4 in the longitudinal direction was performed on a Tinius Olson.	66
31: Image of a hollow spheres tension test in progress.	69

32: Stress-strain curves for the three tension tests performed (top), with corresponding photos of failed specimens (below, tests #1 through #3 pictured from left to right).....	70
33: Macro photo of tensile fracture surface. Arrows indicate examples of spheres from which welds have pulled out.	71
34: Image of PCM tension test that had just completed, showing the full test setup on the left and a zoomed image of the grips and specimen on the right.....	72
35: Stress-strain curves for PCM tension tests, with pores oriented longitudinally (top) and transversely (bottom) to the direction of loading.	73
36: Photos of failed PCM tension specimens, with pores oriented longitudinally (top row) and transversely (bottom row) to the direction of loading.	74
37: An image of the full shear test setup, ready to begin load application.	75
38: Image of shear specimens #1 (left) and #2 (right) at about 0.08 strain, clearly showing shear cracks.	75
39: Stress vs shear strain graph for hollow spheres shear tests.	76
40: Two microstructural photos of hollow spheres showing the amount by which spheres are deformed around weld regions, resulting in instability in the spheres walls.....	78
41: Sample screenshot of program during execution.....	83
42: Hollow spheres geometry: sample geometry as generated (left); photograph of the experimentally-tested sintered hollow spheres steel foam (right).....	89
43: Diagram showing the various geometry characteristics of the hollow spheres algorithm, using the straight cylinder method of representing welds (left), and the overlap method of representing welds (right).	92
44: PCM geometry: sample geometry as generated (left); photograph of the experimentally-tested PCM foam (right).	93
45: Diagram of boundary conditions applied in uniaxial simulations. Grey block arrows represent the vertical fixity applied to the entire face, black block arrows represent the horizontal fixities applied along centerlines, and red block arrows indicate applied loads.	96
46: Simplified diagram showing boundary conditions applied to the shear simulation specimen. Grey block arrows indicate fixities applied to the full area of a face, black block arrows indicate fixities applied only along the centerline shown, and red block arrows indicate applied loads.	98

47: Simplified diagram showing boundary conditions applied during a biaxial simulation. Grey block arrow represent fixities applied to the entire face, black block arrows represent fixities applied only along the centerlines shown, and red block arrows represent loads.....	99
48: Stress-strain curves for hollow spheres validation to experimental data.....	107
49: Poisson's ratio vs strain curves for hollow spheres validation to experimental data.....	107
50: Sample results graph from the hollow spheres test matrix: normalized stress and percent of material yielded versus strain at 23% relative density. Note that stress is normalized by the yield stress of the base metal, 316L stainless steel.....	109
51: Yield stress vs relative density, showing a rough decrease in the yield stress as the sphere diameter increases. The elastic modulus plot shows a similar pattern.....	110
52: Sample results graph from the hollow spheres test matrix: incremental Poisson's Ratio, at a low relative density and a high relative density.....	111
53: Drawing of the meaning of each of the variables used in describing hollow spheres foams.....	113
54: Images of the representative unit cells used in the Gasser, Paun, and Bréchet (2004) simulations used to develop Equation 3.....	114
55: Diagram of the meaning of the matrix of unit cells.....	116
56: ADINA image of the geometry of a deterministic model	118
57: Normal probability plot, showing a nearly Gaussian distribution to the elastic modulus of 30 random samples.....	119
58: Typical image of a geometry with random inputs and a 0.39mm weld diameter. Note the particularly long welds, two of which are circled in yellow, which would not have been created with the 0.13mm threshold.	120
59: Image of a typical geometry generated with a 1mm random perturbation radius and a 0.39mm weld threshold. Note that there are two missing welds. There also some particularly long welds, two of which are circled in yellow, which would not exist with a 0.13mm weld threshold.	121
60: Mean values (top) and standard deviations (bottom) of the normalized elastic modulus for increasing perturbation radii.	122
61: Microscopy image showing the two spheres on the left near to each other, but having no physical connection.....	125

62: Sample image of a deterministic, face-centered cubic geometry used in the sensitivity analysis simulations.	127
63: Graph of all simulations performed in sensitivity analysis. Blue points are FCC simulations; red points are the average of the two random simulations performed at each point. The first-order central difference slopes are shown as solid lines, and the second-order curve fits are shown as dashed lines.....	129
64: Image of a typical geometry generated during the post-yield behavior simulation matrix.....	133
65: Sample output graphs from gasar simulation matrix: normalized stress and percent of material yielded vs strain (left); incremental Poisson's Ratio vs strain (right). Note: Stress is normalized to the yield stress of the base metal, 304L stainless steel.....	134
66: Yield stress vs relative density, showing increased yield stress with greater void elongation. A similar pattern may be seen for elastic modulus.	135
67: Poisson's Ratio versus relative density, showing an increasing plastic Poisson's Ratio and decreasing elastic Poisson's Ratio as the relative density increases.	136
68: Image of possible methods of joining metal foams, as diagrammed in (Ashby, et al. 2000)	143
69: Image of an early experimental test, which should be equivalent to an unconfined connection test of a "single finger" joint.	144
70: Simplified diagrams demonstrating the geometric meaning behind hollow spheres input parameters. <i>Left:</i> with 'weld_type' = 'cylinder'. <i>Right:</i> with 'weld_type' = 'overlap'.....	169
71: Simplified diagram of the geometric meaning behind general closed-cell input parameters. Note that 'phi' would be the rotation into the plane on the above diagram.....	169
72: Screenshot of the Metal Foams Simulator during execution, showing all status information.....	174

CHAPTER 1 INTRODUCTION

Cellular metals made from aluminum or titanium are becoming increasingly popular as a stiff but lightweight material for use in structural components of automobiles and aircraft. However, civil engineering applications require stronger and more economical materials than an aluminum or titanium foam can provide. Over the past decade, materials scientists have developed several ways to manufacture cellular steel, and a couple of these methods are now mature. However, the material's mechanical properties are not yet sufficiently defined to use these steel foams in structural applications, nor is it even known if the material can be used in many applications.

Steel foam has strong potential in the structural engineering realm. Traditional structural steel has proven itself invaluable as an engineering material, but the properties of structural steel have remained largely invariant for the past century. Steel foam offers designers the possibility of selecting their own desired elastic modulus and yield stress from a wide range of possible values, making use of excellent energy absorption properties, and employing highly advantageous stiffness to weight ratios. Further, steel foam offers several non-mechanical properties which are advantageous to structural applications, including thermal resistance, sound and vibration absorption, and gas permeability.

Unfortunately, the relationship between microstructural characteristics and the material's effective macroscopic properties remains poorly defined, and the ability to manufacture a steel foam with a given set of properties depends upon this understanding. In particular, steel foams are manufactured using unique processes which produce microstructures that have not previously been explored in other cellular metals. Previous attempts to characterize the mechanical properties of steel foam have focused almost exclusively upon uniaxial compression tests, both in experimental research and in computational simulations.

Computational simulations have also rarely taken the randomness of the material's microstructure into account and have instead simplified the material to a regular structure.

This thesis features research performed both experimentally and computationally to establish compressive, tensile, and shear properties of steel foams produced by at least two major manufacturing methods.

Experimental research has included uniaxial compression, tension, and shear tests upon a hollow spheres foam, and uniaxial compression and tension upon a PCM foam. These tests include the first known measurement of the shear properties of a steel foam, and among the first tensile measurements.

Computationally, a program which accurately simulates multiple types of metal foams in various loading patterns has been developed as part of this thesis, utilizing both MatLab and the ADINA finite element program. The novel simulations account for the randomness in both the structure and properties of the material, and have been validated against the results of experimental tests. This program has in turn been used in several matrices of uniaxial compression and tension tests to demonstrate the large effect that randomness has upon analyses, to predict the effect of varying geometric parameters, and to prove the feasibility of using simulations to guide manufacturers in setting manufacturing parameters necessary to achieve given mechanical properties.

Suggestions are also provided as to further research work which should be performed to bring steel foam closer to a commercially viable material. Focus in all testing and simulating has been placed upon forming an understanding of the properties that will be most important to structural engineers in potential applications of the new material within the steel design and construction industry.

CHAPTER 2 BACKGROUND AND LITERATURE REVIEW

2.1 Manufacturing Processes

Key Section Objectives

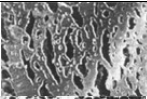
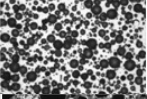
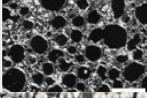


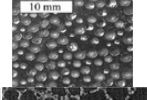
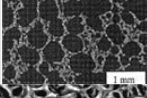
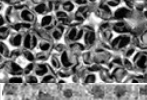
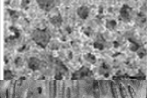

Provide an overview of the manufacturing processes currently available for steel foams

Explain the basics of steel foam morphology and structure

Significant research has been performed regarding optimal manufacturing methods for foams made of metals such as aluminum, titanium and copper. However, steel presents unusual challenges, particularly in steel's high melting point, that require new technologies to be used in manufacturing.

Current methods of manufacturing allow for any of several different cell morphologies in the foam, each with varying regularity, isotropy, and density. All foams are defined as either open-celled or closed-celled based upon whether each microstructural cell is permeable or sealed with surrounding membranes, respectively. Open-cell foams may be considered a network of ligaments and closed-cell foams are networks of membrane walls of various thickness. Current methods of manufacture are able to produce either open-cell or closed-cell steel foams. All published methods for producing steel foams are summarized in Table 1. The following subsections contain more detailed descriptions of the various processes.

Table 1: The several possible manufacturing methods for steel foam, including basic resultant foam characteristics

Process	Microstructure	Primary Variables	Min Dens.	Max Dens.	Cell Morph.	Morphology Notes	Major Advantages	Major Disadvantages	References
Powder metallurgical		Foaming agents (MgCO ₃ , CaCO ₃ , SrCO ₃), cooling	0.04	0.65	Closed	Anisotropic if not annealed enough, or with some mix methods	High relative densities possible	Rough pore surfaces	(Park and Nutt 2001), (Hyun, et al. 2005)
Injection molding with glass balls		Types of glass (e.g. IM30K, S60HS)	0.48	0.66	Closed	Glass holds shape of voids, and increases brittleness of material	High relative densities possible	Potential chemical reactions; glass can fracture	(Weise, Silva and Salk 2010)
Oxide ceramic foam precursor		Ceramic / cement precursor materials	0.13	0.23	Open	Polygonal shapes on small scales, residues of reactions remain	Foaming at room temperatures; complex shapes possible	Many step process	(Verdooren, Chan, et al. 2005a), (Verdooren, Chan, et al. 2005b)
Consolidation of hollow spheres		Sphere manufacture, sphere connections	0.04	0.21	Either	Two different cell voids: interior of spheres, and spaces between spheres	Low relative densities possible; predictable and consistent behavior	High relative densities not possible	(Friedl, et al. 2007), (Rabiei and Vendra 2009)
PCM		Types of working before sintering, filler materials	0.05	0.95	Open	Anisotropy is controllable	Wide range of relative densities; anisotropy is controllable	Potentially brittle material may result	(Tuchinsky 2007)
Comp. powder metallurgy / hollow spheres		Matrix material used, casting may be done instead of PM	0.32	0.43	Closed	Powder metallurgical region may be foamed or a semi-solid matrix	Behavior is predictable; no collapse bands until densification	Many step process	(Rabiei and Vendra 2009), (Neville and Rabiei 2008)
Slip Reaction Foam Sintering		Dispersant, bubbling agent, and relative quantities	0.12	0.41	Open	Highly variable cell diameters are produced	Many optimizable parameters; foaming at room temperature	Cell diameter not highly controllable	(Angel, Bleck and Scholz 2004)
Polymer foam precursor		Polymer material used	0.04	0.11	Open	Cells take on whatever characteristics the polymer foam had	Low density open-cell structure for filter and sound absorption	Too weak for most structural applications	(Adler, Standke and Stephani 2004)
Powder space holder		Filler material used, material shapes and gradation	0.35	0.95	Closed	Porosity may be graded across material	Porosity may be graded by a wide range across the material	Space holder material may not be removable	(Nishiyabu, Matsuzaki and Tanaka 2005)
Gasar / lotus-type		Partial pressure of gas, which gas to use	0.36	1.00	Closed	Highly anisotropic but aligned cell shapes are unavoidable	Continuous production techniques; high relative densities are possible	Isotropic cell morphologies are not possible	(Hyun, et al. 2005), (Ikeda, Aoki and Nakajima 2007)

2.1.1 Hollow Spheres

Giving highly predictable mechanical properties and requiring only minimal heat treatment, the consolidation of hollow spheres method is one of the two most popular techniques for manufacturing steel foams (Rabiei and Vendra 2009). The hollow spheres method may result in foams of either fully closed-cell or mixed open- and closed-cell morphology, with relative densities from about 4% to 20% possible. The method produces highly predictable material properties as cell (void) size is strictly controlled (Friedl, et al. 2007). All hollow spheres processes first involve taking solid spheres of some cheap material such as polystyrene, placing these spheres in a liquid suspension of metal powder and a binding agent, and then draining the liquid to create “green spheres.” These green spheres may then be sintered individually and consolidated using an adhesive matrix, casting in a metal matrix (Brown, Vendra and Rabiei 2010), or compacting through powder metallurgy techniques (Neville and Rabiei 2008). Alternatively, the green spheres may also all be stacked into a bulk shape, and sintered as all at once under high temperature and pressure to create a single block of hollow spheres (Friedl, et al. 2007). In the sintering process, the spheres end up held together by welds, or necks of metal that form between individual hollow spheres. A further special variation involves manufacturing the spheres with a blowing agent within and then allowing the spheres to expand and sinter into the resultant honeycomb-like shapes (Daxner, Tomas and Bitsche 2007).

2.1.2 Gasar / Lotus-Type

The gasar manufacturing method, also known as the lotus-type method, is capable of producing high-density foams ranging from about 35% to 100% relative density with highly anisotropic, closed-cell morphology. The method features the great advantage that it is easily

adapted to a continuous casting process (Hyun, et al. 2005). It also allows for high tensile strength and ductility—up to 190 MPa at over 30% strain for a foam of 50% relative density—due to its direct load paths and largely non-porous matrix. In comparison, hollow spheres foams reach ultimate tensile strength at about 8 MPa at 2% strain and 8% relative density (Friedl, et al. 2007).

Gasar steel foams take advantage of the fact that many gases are more soluble in metals while they are in their liquid state than when they are in their solid state. In the case of steel, either hydrogen or a hydrogen-helium mixture is diffused into molten steel (Ikeda, Aoki and Nakajima 2007). As the steel solidifies, the gas leaves the solution, creating pores within the solid steel body. Two similar methods of performing this process continuously have been developed: continuous zone melting and continuous casting (Hyun, et al. 2005). In continuous zone melting, one segment of a rod of the base metal is melted in the presence of the diffusive gas, and then allowed to re-solidify shortly thereafter. In continuous casting, the base metal is kept melted in a crucible in the presence of the gas, and then slowly cast and solidified (Hyun, et al. 2005).

2.1.3 Powder Metallurgy

Originally developed for aluminum foams, the powder metallurgy method was one of the first methods to be applied to steel foams and is still one of the two most popular (Kremer, Liszkiewicz and Adkins 2004). It produces primarily closed-cell foams and is capable of developing highly anisotropic cell morphologies. The relative densities possible with this method are among the highest, up to 0.65, making it a strong candidate for many structural engineering applications. Structural applications may demand that the foam retain a relatively high portion of the base material strength, which should occur at higher relative densities.

The powder metallurgy method involves combining metal powders with a foaming agent, compacting the resulting mixture, and then sintering the compacted piece at pressures of 900-1000 MPa (Muriel, et al. 2009). The metal is brought to the melting point and held there for a period of time depending on the foaming agent and desired cell morphology, usually about 15 minutes (Muriel, et al. 2009). The final product may also be heat treated to optimize the crystal structure of the base metal. A variation, known as the powder space holder method, involves using a simple filler material rather than the foaming agent and allows for graded porosity across the material (Nishiyabu, Matsuzaki and Tanaka 2005).

2.1.4 PCM

The PCM method, originally referred to as a bimaterial rods method, involves forming steel around a filler material, extruding these rods, sintering them together, and then melting out the filler material. The rods may either be fed through a filter which would first align them, or they may be placed randomly, allowing the orientation of the rods and therefore the voids to be controlled. The rods may also be cut to any desired length or mixture of lengths, allowing void length to be precisely controlled. In the end, a uniquely uniform cylindrical cell morphology results, and the method may have the potential to produce a wide range of relative densities from 5% to 95% with highly adjustable void morphologies (Tuchinsky 2007).

2.1.5 Other Methods

Another method of production for steel foams involves the use of a ceramic (Verdooren, Chan, et al. 2005a) (Verdooren, Chan, et al. 2005b) or polymer (Adler, Standke and Stephani 2004) precursor. For ceramics, a chemical reaction is initiated to reduce the iron oxide to pure iron, and then the iron is sintered with carbon already present in the ceramic mixture to result in steel foam (Verdooren, Chan, et al. 2005a). For polymers, a replication method is used, in

which molten steel is poured into a high-porosity open-cell precursor shape (Adler, Standke and Stephani 2004). The final steel foam will take on the same morphology as the precursor material. Possible relative densities range from 4% to 23% depending largely on the precursor.

Another manufacturing method, the slip reaction foam sintering (SRFS) method, is specific to iron-based foams and results in an open-cell morphology. It has the advantage that, being based entirely on chemical reactions, it operates almost entirely at room temperature. It produces foams of moderate densities, ranging from about 12% to 41%. Two powders are mixed, one containing the base metal and a dispersant, and the other containing an acid (the binder) and a solvent. The acid reacts with the iron to produce hydrogen, which then creates air pockets. Those pockets are held in place in the powder by a partial solidification reaction between phosphoric acid and the iron. Once this reaction is complete, water byproducts are drained out and the foam may be sintered to achieve full strength (Angel, Bleck and Scholz 2004).

There are several further methods of steel foam manufacture that have been the subject of at least preliminary investigation by material scientists, including injection molding and various fibrous foams. Injection molding involves mixing hollow glass beads or other granular material into the molten metal. To date, steel foams with glass beads have shown high strength, but also low ductility and brittle fracture (Weise, Silva and Salk 2010). Various fibrous foams have been proposed, but their resulting mechanical strength is likely too weak for foreseeable structural applications. There are two forms of such fibrous foams: truss cores, and sintered fibers. Truss cores involve twisting or welding thin fibers into mesoscale trusses of various shapes. Such mesoscale trusses can serve as the core layer in structural sandwich panels (Lee, Jeon and Kang 2007). Fiber sintering involves laying out fibers and sintering them together. Again, strength has generally been too low for structural applications, though the oriented fibers

do show potential applications for a material that would only support tensile loads (Kostornov, et al. 2008).

Key Section Findings

The most popular steel foam manufacturing methods are hollow spheres, gasar, and powder metallurgy.

Each production method has its own unique advantages and disadvantages in morphology and difficulty of manufacture.

2.2 Effective Macroscopic Properties

Key Section Objectives

Describe the basic mechanical and non-mechanical properties of steel foams.

Give examples of the variability of foam properties, as determined through experimentation.

Explain the several attempts that have been made to model steel metal foam behavior, through both computational simulation and mathematical formulae.

For engineering purposes, the material properties are of primary importance, and the manufacturing process used to achieve these properties is unimportant. In contrast, the investigators who have developed the manufacturing processes described in section 2.1 have performed only limited tests of the material properties of the steel foams resulting from each process. This section reviews the key experimental studies regarding the mechanical and non-mechanical properties of steel foams (see Table 2).

In compression, steel foams display a stress-strain curve similar to that of Figure 1, featuring an elastic region (up to σ_c), a plateau region in which the voids begin plastic deformation (identified by σ_p), and a densification region in which cell walls come into contact with one another and compressive resistance rapidly increases (after ϵ_D).

In tension, yielding and fracture of steel foams occur first in either the walls or ligaments that surround the voids, or in the case of hollow spheres foams, in the welds that sinter together

the material. Due to bending of the walls, tensile yield strengths of the bulk foamed material may be significantly less than that of the base material.

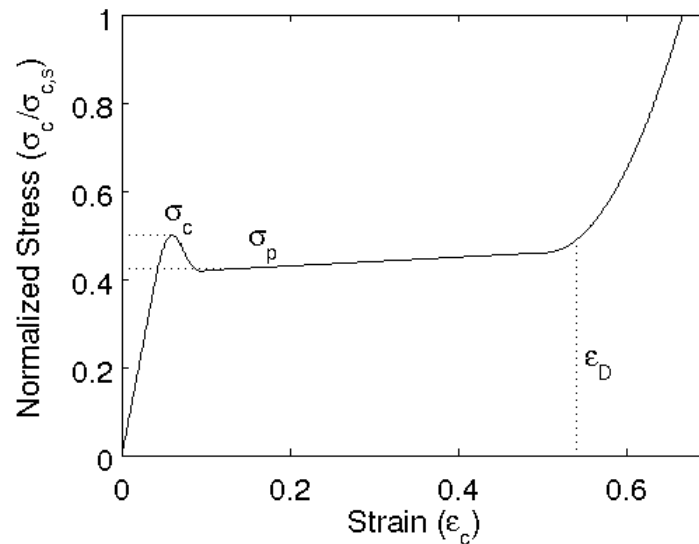


Figure 1: Typical stress-strain curve for steel foam in uniaxial compression

2.2.1 Experimental Material Properties

A number of experiments have been performed to measure steel foam mechanical properties (see Table 2). While many models have been proposed to predict properties (see section 2.2.2), all implicitly assume that foams of a given base material and relative density will behave the same (Ashby, et al. 2000). However, the material properties depend upon the manufacturing method (Fathy, Ahmed and Morgan 2007), cell size and morphology (Fazekas, et al. 2002), and sample size tested (Andrews, et al. 2001). For example, powder metallurgy and gasar steel foams usually have anisotropic cells, resulting in tensile and compressive yield strengths which vary by as much as a factor of two depending on direction (Park and Nutt 2001) (Kujime, Hyun and Nakajima 2005). Others have studied size effects in metal foams, determining that macroscopic material properties are dependent on sample dimensions (Andrews, et al. 2001).

The most common mechanical property to measure is the compressive yield strength or plateau strength. The plateau strength is usually about 5% higher than the measured yield strength (Ashby, et al. 2000). As shown in Table 4, the compressive yield strength of steel foam varies from approximately 1 MPa for highly porous foams (<5% density) to 300 MPa for extremely dense samples. At about 50% density, steel foam's compressive strength varies from 100 MPa for typical samples to upwards of 300 MPa for highly anisotropic or specially heat-treated samples. Other mechanical properties, including elastic modulus, Poisson's ratio, ultimate tensile strength, densification strain, and energy absorption, have been less frequently published.

Compressive yield strength (σ_c) normalized by the solid steel compressive yield ($\sigma_{c,s}$) is plotted against elastic modulus (E_c) normalized by the solid steel elastic modulus ($E_{c,s}$) in Figure 2, showing that different ratios of stiffness to strength have been achieved, illustrating the large material selection space available to designers. The solid lines indicate the envelope of stiffness to strength values predicted by the Gibson and Ashby open and closed cell models for compressive strength (Ashby, et al. 2000). The wide envelope indicates that there exists a substantial design space for steel foams in terms of stiffness to strength ratio.

Table 2: Material properties extracted from selected publications

Manufacturing Process	Relative Density	Base metal	Compressive Yield Stress (MPa)	Compressive Elastic Mod. (MPa)	Ultimate Tensile Stress (MPa)	Min Comp Energy Abs (MJ/m ³)	References
Casting HS – Al-steel composite	0.42	A356+316L	52-58	10000-12000		51 (at 57%)	(Brown, Vendra and Rabiei 2010)
Ceramic precursor – CaHPO ₄ *2H ₂ O	0.23	Fe-based mixture	29 +/- 7				(Verdooren, Chan, et al. 2005a)
Ceramic precursor – MgO, LD	0.13	Fe-based mixture	11 +/- 1				(Verdooren, Chan, et al. 2005b)
Ceramic precursor – MgO, HD	0.21	Fe-based mixture	19 +/- 4				(Verdooren, Chan, et al. 2005b)
Injection molding – S60HS	0.49-0.64	Fe 99.7%	200				(Weise, Silva and Salk 2010)
Injection molding – I30MK	0.47-0.65	Fe 99.7%	200				(Weise, Silva and Salk 2010)
Lotus type – 50%	0.5	304L steel	95		190		(Ikeda, Aoki and Nakajima 2007)
Lotus type – 62%	0.62	304L steel	115		280		(Ikeda, Aoki and Nakajima 2007)
Lotus type – 70%	0.7	304L steel	130		330		(Ikeda, Aoki and Nakajima 2007)
Polymer precursor – 4.3%	0.04	316L steel	1.2	83			(Adler, Standke and Stephani 2004)
Polymer precursor – 6.5%	0.065	316L steel	3	196			(Adler, Standke and Stephani 2004)
Polymer precursor – 7.6%	0.076	316L steel	4.8	268			(Adler, Standke and Stephani 2004)
Polymer precursor – 9.9%	0.099	316L steel	6.1	300			(Adler, Standke and Stephani 2004)
PM – MgCO ₃ foaming	0.4-0.65	Fe-2.5C powder	30(par)-300(perp)				(Park and Nutt 2001)
PM – MgCO ₃ and CaCO ₃ foaming	0.53-0.54	Fe-2.5C powder	40(5e-5 s ⁻¹)-95(16 s ⁻¹)			50 (4.5E-5 s ⁻¹)	(Park and Nutt 2002)
PM – MgCO ₃ and SrCO ₃ foaming	0.46-0.64	Fe-2.5C powder	95-320(pre-annealed)			45 (at 50%)	(Park and Nutt 2000)
PM – MgCO ₃ foaming	0.55-0.60	Fe-2.5C, Fe-2.75C, Fe-3C powders	50-180				(Muriel, et al. 2009)
PM / HS composite – 3.7mm, LC steel	0.389	Fe+.002% O,.007% C	30	5600		18.9 (at 54%)	(Rabiei and Vendra 2009)
PM / HS composite – 1.4mm, LC steel	0.324	Fe+.002% O,.007% C	30-89	5600		41.7 (at 57%)	(Rabiei and Vendra 2009)
PM / HS composite – 2.0mm, stainless	0.375	316L steel	89	9000-10300		67.8 (at 54%)	(Rabiei and Vendra 2009)
Sintered HS – 2mm dense	0.04	316L steel	0.89	201	1.59		(Friedl, et al. 2007)
Sintered HS – 2mm porous	0.04	316L steel	1.27	261	1.63		(Friedl, et al. 2007)
Sintered HS – 4mm dense	0.04	316L steel	1.55	358	2.53		(Friedl, et al. 2007)
Sintered HS – 4mm porous	0.04	316L steel	1.5	362	1.95		(Friedl, et al. 2007)
Sintered HS – 4mm dense	0.08	316L steel	3.34	637	5.32		(Friedl, et al. 2007)
Sintered HS – 4mm porous	0.08	316L steel	3.05	627	5.06		(Friedl, et al. 2007)

Note: Due to chemical processes involved in all manufacturing methods, foam properties are not directly comparable to solid metal properties.

Poisson's ratio for steel foams is commonly assumed to be the elastic base metal value of 0.3, and few publications have measured Poisson's ratio. However, for hollow spheres steel foams, experimental regiments have reported ranges from 0 (or even slightly negative) to 0.4 (Lim, Smith and McDowell 2002) and 0.09 to 0.2 (Kostornov, et al. 2008), depending on the density and manufacturing method.

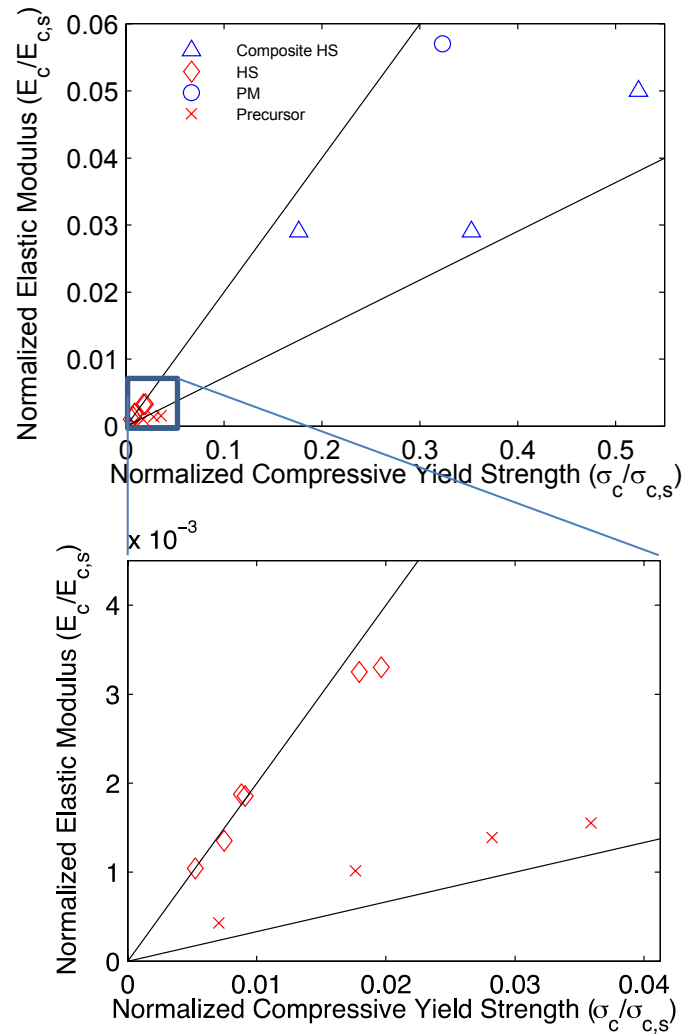


Figure 2: Compressive yield strength versus normalized elastic modulus of various types of steel foams, as reported by various researchers (see Table 2). The Gibson & Ashby model's minimum and maximum values are also displayed (see section 2.2.2.2). The lower graph zooms in upon the open-celled foams in the top graph.

Evaluation of the densification strain and energy absorption is possible in most experiments, but few values are published. Densification usually occurs at 55-70% strain. Energy absorption measured up to 50% strain ranges from 40 MJ/m³ to 100 MJ/m³, for densities near 50%.

In the few tension tests conducted, tensile strengths between 1 and 5 MPa for low-density sintered hollow spheres foams and up to over 300 MPa for the anisotropic gasar foam parallel to the pore orientation have been recorded.

A basic summary of tested thermal, acoustic, and permeability properties is included in Table 3. Non-structural properties are directly associated with parameters other than relative density: cell morphology for permeability (Khayargoli, et al. 2004), cell size for acoustic absorption (Tang, et al. 2007), and cell wall thickness for thermal conductivity (Zhao, et al. 2004). Nevertheless, the primary predictive parameter is still relative density and Table 3, which summarizes these values, is based upon these measurements.

Table 3: Non-mechanical material properties for steel foam, including thermal, acoustic, and permeability, for optimal manufacturing methods of steel foam.

Property	Minimum	@ Density	Maximum	@ Density	Reference
Thermal Conductivity ^a (W/mK)	0.2	0.05	1.2	0.1	(Zhao, et al. 2004)
Acoustic Absorption Coeff @ 500 Hz	0.05	0.12	0.6	0.2	(Tang, et al. 2007)
Acoustic Absorption Coeff @ 5000 Hz	0.6	0.27	0.99	0.12	(Tang, et al. 2007)
Permeability (m ² * 10 ⁻⁹)	2	0.14	28	0.1	(Khayargoli, et al. 2004)
Drag Coefficient (s ² /m * 10 ³)	0.3	0.9	2.2	0.14	(Khayargoli, et al. 2004)

Note: Solid steel thermal conductivity is in the range of 20-50 W/mK, acoustic absorption coefficients range from 0.08 to 0.12, permeability is 0, and drag coefficient is irrelevant due to the impermeability.

2.2.2 Modeling of Mechanical Properties

In addition to experimental evaluation of the mechanical properties of steel foams, investigators have attempted to develop computational or analytical models for material

properties that incorporate explicit representation of the foam microstructure. Attempts have also been made to develop and fit phenomenological models to the mechanical properties obtained in experiments, interpolating to obtain a good curve fit. Finally, continuum representations of the mechanics of steel foam deformations have used constitutive models based on metal plasticity to represent the nonlinear response of metal foams.

2.2.2.1 Computational Microstructure Models

Explicit modeling of steel foam microstructure has been explored by a variety of investigators as summarized in Table 4. Computational approach, cell morphology, software, and details of the mechanics are also summarized. While nearly all of the studies include plasticity in the simulation, only five include contact, and none include material fracture, meaning that simulation of the densification strain and tensile ductility is an underdeveloped area of inquiry.

The simplest models employ tetrakaidcahedra geometry, with continuous faces for closed-cell foams, and with only struts (no faces) for open-cell foams (Kwon, Cooke and Park 2002). A tetrakaidcahedron is shown in Figure 3. These shapes are not physically possible to create by current manufacturing methods, but are the most computationally efficient shapes because they stack without gaps. Tetrakaidcahedra models also exist which examine the impact of defects on the unit cell (Kepets, Lu and Dowling 2007). Microstructural models for unit cells of hollow sphere steel foams with ordered packing are also relatively common (Lim, Smith and McDowell 2002). More recently, models of representative samples of closed-cell foams with random material removed have been explored (Kari, et al. 2007), but these models require fine meshes and can be computationally challenging.

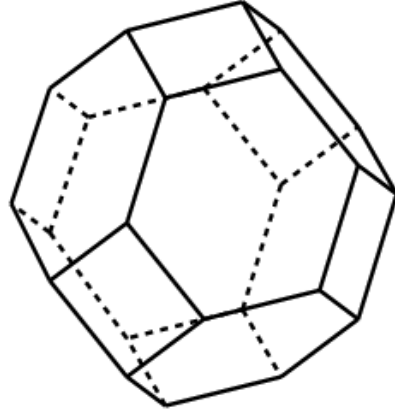


Figure 3: A single tetrakaidecahedron. These shapes stack without gaps, so conglomerations of tetrakaidecahedra are used in simple computational models.

A number of microstructural features have not been modeled to date, including strain hardening in the base metal, fracture, the presence of pressure in internal voids, and voids made from glass or other materials. Further, simulations generally ignore any effects of special treatments to the material such as unusual heat treatments, instead focusing on the foams that are more likely to enter commercial production. Currently, the greatest restriction in microstructural computational modeling is the available computational resources, but as computational capabilities continue to expand, the fidelity of steel foam computational models will also increase.

Table 4: Microstructural representations of steel foam used in selected published literature.

Microstructure Representation	Intended to model	Cell Types	Software	Nonlinearities Included	Behaviors Modeled	Reference
FCC hollow spheres, simulated weld connections	Sintered metal HS $r/R < 0.2$	Unit spheres	CAST3M, SAMCEF	None – elastic only	3 imposed stress tensors	(Gasser, Paun and Brechet 2004)
Two 2D circles with weld connections	Sintered hollow metal spheres	Two 2D circles	ZeBuLoN	Power law strain hardening, contact	Damage and densification of spheres	(Fallet, Salvo and Brechet 2007)
SC hollow spheres, simulated weld connections	Sintered hollow metal spheres	Unit spheres	ABAQUS/CAE	Some power law strain hard.	40 imposed stress tensors	(Sanders and Gibson, Mechanics of BCC and FCC hollow-sphere foams 2002)
Tetraikaidecahedrons tightly-packed	General open-cell metal foams	Unit tetraikaidecahedrons	(not stated)	Plastic deformation	Elastic compression and plastic damage	(Kwon, Cooke and Park 2002)
FCC and HCP hollow spheres, direct contact	Sintered hollow metal spheres	Unit spheres	ABAQUS	Contact, plastic deformation	Plastic response in compression and tension	(Karagiozova, Yu and Gao 2007)
Tetraikaidecahedrons w/ random defects	Sintered hollow steel spheres	Bulk tetraikaidecahedrons	ABAQUS, MATLAB	Large displacements, plastic deformation	Plastic collapse in uniaxial compression	(Kepets, Lu and Dowling 2007)
SC, BCC, FCC, and HCP hollow spheres	Sintered, syntactic, & perforated HS	Unit spheres & perforated spheres	MSC NASTRAN	Plastic deformation	Heat transfer, uniaxial tension	(Oechsner 2009)
SC hollow spheres	Pre-crushed sintered steel HS	Unit elongated spheres	LS-PREPOST, CATIA, ANSYS, LS-Dyna	Non-penetration contact, plastic deformation	Plastic collapse in uniaxial compression	(Speich, et al. 2009)
Composite material with random hollow spheres	Composite hollow sphere foams	Bulk spheres	ANSYS-APDL	Plastic deformation	Uniaxial compression	(Kari, et al. 2007)
FCC hollow spheres	Sintered hollow metal spheres	Unit spheres	(theory) & ABAQUS	Contact, plastic deformation	Plastic collapse in uniaxial compression	(Karagiozova, Yu and Gao 2006)
ABC symmetry hollow spheres	Sintered hollow metal spheres	Unit spheres	(not stated)	Plastic deformation	Uniaxial compression	(Franeck and Landgraf 2004)
SC, BCC, FCC, and HCP hollow spheres	Sintered hollow metal spheres	Unit spheres	ABAQUS	Plastic deformation	Uniaxial compression	(Gao, Yu and Karagiozova 2007)
Random hollow spheres	Sintered hollow metal spheres	Single sphere	ABAQUS	Non-penetration contact, plastic deformation	Uniaxial compression	(Lim, Smith and McDowell 2002)

2.2.2.2 Mathematical Models with Microstructural Parameters

The first and still most widely accepted models for representing the mechanics of metal foams are those developed by Gibson and Ashby (Ashby, et al. 2000) as summarized in Table 5. The expressions assume that the primary dependent variable for all foam mechanics is the relative density of the foam, and all other effects are lumped into a multiplicative coefficient with typical ranges provided within the formulas in Table 5. Selection of the appropriate coefficient must be done with care and the resulting expressions are only valid for a small range of relative densities as well as specific morphologies and manufacturing methods. Convergence to solid steel values at high relative density is not intrinsic to the expressions.

Table 5: Equations for mechanical properties of metal foams as set by Gibson and Ashby (2000)

Property	Open-Cell Foam	Closed-Cell Foam
Elastic modulus	$E / E_s = (0.1-4) \cdot (\rho/\rho_s)^2$	$E / E_s = (0.1-1.0) \cdot [0.5 \cdot (\rho/\rho_s)^2 + 0.3 \cdot (\rho/\rho_s)]$
Compressive yield strength	$\sigma_c / \sigma_{c,s} = (0.1-1.0) \cdot (\rho/\rho_s)^{3/2}$	$\sigma_c / \sigma_{c,s} = (0.1-1.0) \cdot [0.5 \cdot (\rho/\rho_s)^{2/3} + 0.3 \cdot (\rho/\rho_s)]$
Tensile strength	$\sigma_t = (1.1-1.4) \cdot \sigma_c$	$\sigma_t = (1.1-1.4) \cdot \sigma_c$
Shear modulus	$G = 3/8 \cdot E$	$G = 3/8 \cdot E$
Densification strain	$\epsilon_D = (0.9-1.0) \cdot [1 - 1.4 \cdot (\rho/\rho_s) + 0.4 \cdot (\rho/\rho_s)^3]$	$\epsilon_D = (0.9-1.0) \cdot [1 - 1.4 \cdot (\rho/\rho_s) + 0.4 \cdot (\rho/\rho_s)^3]$

Comparison of the expressions of Table 5 with available experimental data for compressive yield stress and Young's modulus is provided in Figure 4. Basic trends are captured correctly by the expressions, but exact agreement is poor, and only a very wide envelope is effectively provided. Data outside the "bounds" of the Gibson and Ashby expressions include steel foams with unusual anisotropy, special heat treatments, and unusually thin-walled hollow spheres. The Gibson and Ashby expressions therefore represent an adequate starting point, but other models require investigation.

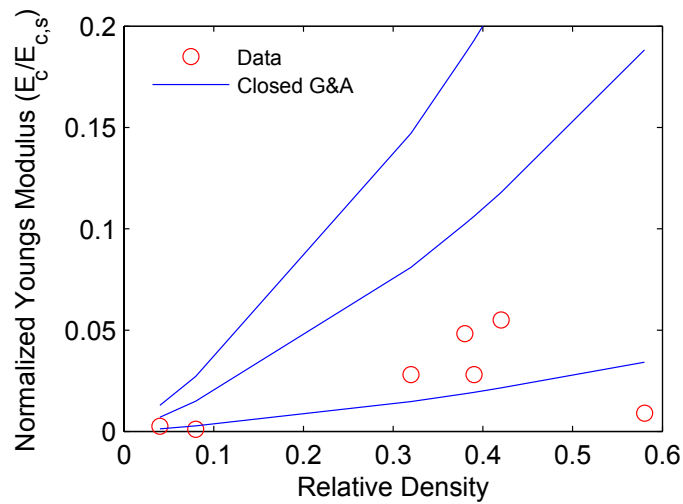
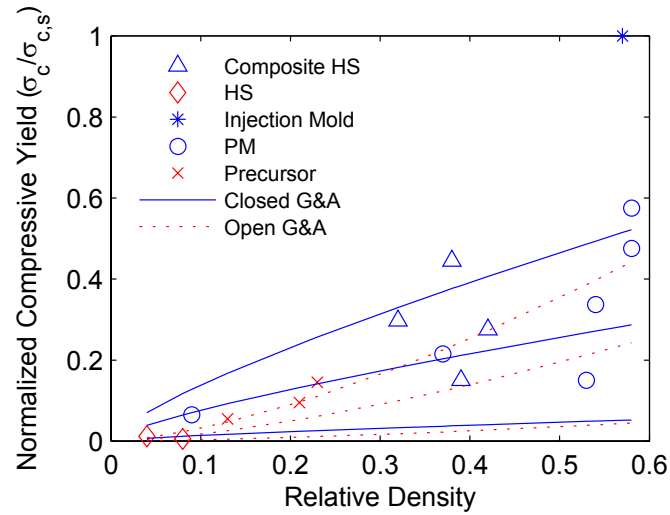


Figure 4: Comparison of available experimental data with Gibson and Ashby expressions of Table 5. Blue lines indicate Gibson & Ashby expressions with leading coefficients equal to minimum, maximum, and central value.

Experimental researchers have developed versions of the Gibson and Ashby expressions that are specific subsets of foam types, as provided in Table 6. For hollow spheres foams, the ratio of radius to thickness of the spheres has been introduced as a descriptive variable in addition to the relative density. Comparison of the expressions of Table 6 with those of Gibson and Ashby, as shown in Figure 5, demonstrate that although all yield different solutions, they remain within the established bounds. Nevertheless, in comparison to experimental results, these more specific models still make little improvement upon the ability to actually predict

mechanical properties of metal foam. Utilizing plate bending and membrane theory, closed-cell foam models that include relative density as well as a measure of the proportion of material present in the walls of the cell versus in its struts (denoted as Θ) have also been proposed by Gibson and Ashby (Ashby, et al. 2000) and others. Despite the potential for increased accuracy, the uncertainty in defining Θ accurately, and the simplicity of existing expressions (regardless of accuracy), has led to slow adoption of this improvement. It also remains uncertain as to how much more accurate even these highly complex equations may prove to be.

Table 6: Experimentally derived expressions for mechanical properties of elastic modulus (first table) and compressive yield (second table). t = sphere thickness, R = outer radius of hollow sphere, r = radius of joined metal between spheres

Model Type	Constitutive Equation of Elastic Modulus	Reference
Ideal		
Tetrakaidecahedral	$E_d/E_{c,s} = 0.32 \cdot (\rho/\rho_s)^2 + 0.32 \cdot (\rho/\rho_s)$	(Sanders 2002)
Powder Metallurgy	$E_d/E_{c,s} = 0.08 \cdot (\rho/\rho_s)^2$	(Gauthier 2007)
Sintered Hollow Spheres (FCC)	$E_d/E_{c,s} = 1.25 \cdot (\rho/\rho_s)^{1.33}$, $(\rho/\rho_s) < 0.06$	(Sanders 2002)
Sintered Hollow Spheres (BCC)	$E_d/E_{c,s} = 0.72 \cdot (\rho/\rho_s)^{1.13}$, $(\rho/\rho_s) \geq 0.06$	
Sintered Hollow Spheres (SC)	$E_d/E_{c,s} = 2.62 \cdot (\rho/\rho_s)^{1.67}$, $(\rho/\rho_s) < 0.1$	(Sanders 2002)
Sintered Hollow Spheres (SC)	$E_d/E_{c,s} = 0.96 \cdot (\rho/\rho_s)^{1.25}$, $(\rho/\rho_s) \geq 0.1$	
Sintered Hollow Spheres (FCC)	$E_d/E_{c,s} = 0.65 \cdot (\rho/\rho_s)^{1.36}$	(Sanders 2002)
Sintered Hollow Spheres (BCC)	$E_d/E_{c,s} = [0.826 \cdot (t/R) + 0.118] \cdot (t/R)$	(Sanders and Gibson 2002)
Sintered Hollow Spheres (FCC)	$E_d/E_{c,s} = [0.826 \cdot (t/R) + 0.118] \cdot (t/R)$	(Sanders and Gibson 2002)
Sintered Hollow Spheres (FCC)	$E_d/E_{c,s} = [5.14 \cdot (r/R)^2 + 0.57 \cdot (r/R) + 0.118] \cdot (t/R) + [-30.1 \cdot (r/R)^2 + 10.5 \cdot (r/R) + 0.826] \cdot (t/R)^2$	(Sanders and Gibson 2002)

Model Type	Constitutive Equation of Compressive Yield	Reference
Ideal		
Tetrakaidecahedral	$\sigma_c/\sigma_{c,s} = 0.33 \cdot (\rho/\rho_s)^2 + 0.44 \cdot (\rho/\rho_s)$	(Sanders 2002)
Powder Metallurgy	$\sigma_c/\sigma_{c,s} = 1.1 \cdot (\rho/\rho_s)^{3/2}$	(Gauthier 2007)
Sintered Hollow Spheres (FCC)	$\sigma_c/\sigma_{c,s} = 1.0 \cdot (\rho/\rho_s)^{1.30}$	(Sanders 2002)
Sintered Hollow Spheres (BCC)	$\sigma_c/\sigma_{c,s} = 0.81 \cdot (\rho/\rho_s)^{1.35}$	(Sanders 2002)
Sintered Hollow Spheres (SC)	$\sigma_c/\sigma_{c,s} = 0.65 \cdot (\rho/\rho_s)^{1.36}$	(Sanders 2002)
Sintered Hollow Spheres (FCC)	$\sigma_c/\sigma_{c,s} = [-1.58 \cdot 10^{-3} \cdot \theta^2 + 1.10 \cdot \theta + 0.015] \cdot (t/R)^{1.13}$	(Sanders and Gibson 2002)
Sintered Hollow Spheres (BCC)	$\sigma_c/\sigma_{c,s} = [0.029 \cdot \theta + 0.352] \cdot (t/R)^{1.13}$	(Sanders and Gibson 2002)
Sintered Hollow Spheres (FCC)	$\sigma_c(\epsilon)/\sigma_{c,s} = 0.071 \cdot \epsilon - 0.6295 \cdot (\rho/\rho_s)^2 + 0.2674 \cdot \epsilon - 0.1608 \cdot (\rho/\rho_s)$, $\epsilon > 0.03$	(Sanders and Gibson 2002)
Sintered Hollow Spheres (BCC)	$\sigma_c(\epsilon)/\sigma_{c,s} = 0.0519 \cdot \epsilon - 0.5958 \cdot (\rho/\rho_s)^2 + 0.4652 \cdot \epsilon - 0.4318 \cdot (\rho/\rho_s)$, $\epsilon > 0.03$	(Sanders and Gibson 2002)

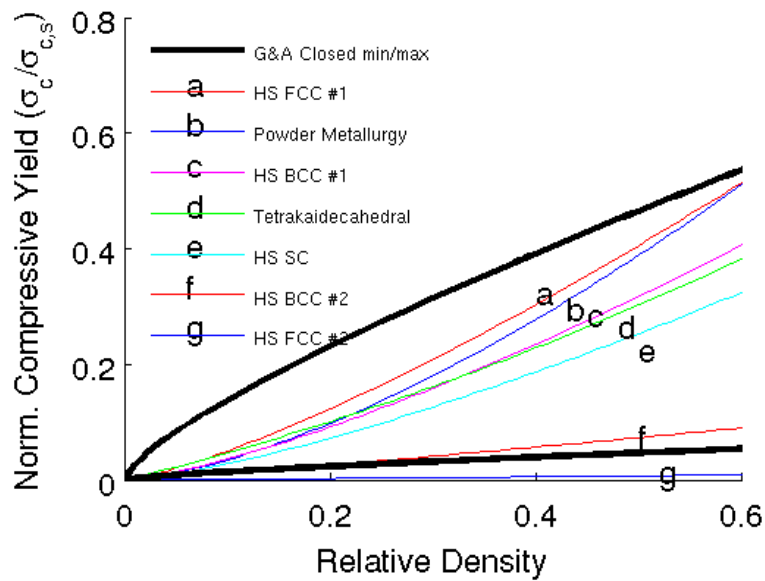


Figure 5: Graph comparing the alternative mathematical models for compressive yield with the model of Gibson and Ashby. The graph for alternative elastic modulus models shows similar patterns.

Key Findings

Steel foam behaviors similarly to solid steel except in compression, where the plastic modulus increases massively at densification in high strain.

The effective macroscopic properties of foams vary dramatically between manufacturing methods, providing a large design space to engineers. However, few researchers have tested properties other than in compression.

Computational simulations have focused almost exclusively upon highly-simplified hollow spheres foams, and usually only model compression.

Mathematical models provide only a very general guidance as to predicting the macroscopic properties of a metal foam based upon microstructural characteristics.

2.3 Usage in Structural Engineering

Key Section Objectives

Explain the need and method of modeling steel foam in a homogenized manner based on plasticity models.

Describe basic advantages of steel foam over other building materials, both in mechanical and non-mechanical properties.

Identify several example applications for steel foam in structural engineering, based upon both published literature and current uses of foams in metals other than steel.

To evaluate the properties of any new material properly, its likely future usage must be considered throughout to determine the most important properties and to avoid examining unnecessary properties. Various structural applications are being considered for steel foam, some of which even vary depending upon the manufacturing method of the foam. For example, hollow spheres foams are known to have poor tensile properties and cannot be manufactured at higher than about 25% relative density, so their potential applications are almost entirely limited to compression-only uses that do not require high strength. Efficient use of the material requires being able to perform efficient computational simulations in finite element packages, which in turn requires being able to simulate the steel foams in a homogenized manner, so the inputs for such homogenized models must also be established through microscale material investigation.

2.3.1 Plasticity Based Models

Due to microstructural complexity, simulations of metal foam components using traditional 3D solid elements would require orders of magnitude more elements than simulations of equivalent homogeneous solid metal components. Therefore, new types of elements capable of representing a large volume of metal foam as a macroscopic material are necessary for the examination of structural components and applications of the material.

Macroscale finite element models utilizing either solid or shell elements may employ homogenized elastic properties, but this will only lead to an accurate material response representation up to initial yield. Classical metal plasticity utilizing von Mises yield criteria assumes metals are incompressible in the plastic regime and that yield properties are dependent only on distortional energy associated with shear stress (Khan 1995). However, steel foam has internal voids, is compressible in the plastic regime, and is thus dependent upon dilatational energy, associated with mean stress. Traditional material definitions for finite elements are therefore incapable of representing metal foams as a bulk material during plastic deformation.

Miller (2000) and Deshpande and Fleck (2000) generalized the von Mises yield criterion by accounting for pressure dependence (mean stress) in their effective stress formulation. These initial models only included linear hardening. To capture the densification that is experienced by metal foams at high strains, the model was expanded and validated for aluminum foams by Reyes (2003) and Hanssen et al. (2002) to include nonlinear hardening, and later to also account for tensile fracture. The Deshpande-Fleck model with these improvements is implemented in various commercial finite element codes such as LS-DYNA and ABAQUS, but calibration for steel foams has not been conducted.

Important inputs required to calibrate the Deshpande-Fleck model include a stress-strain curve up through densification, incremental Poisson's ratio values, and a factor representing the multiaxial strength of the material. These inputs must be derived through experimental testing and microscale simulations which utilize traditional plasticity elements. The Deshpande-Fleck model is not designed for and cannot be used on microstructural simulations.

2.3.2 Structural Applications

Foamed steel introduces relative density as a design variable in material selection, and the ability to foam steel affords potential advantages over solid steel in both structural and non-structural properties. These advantages have been utilized in existing design applications:

Structural advantages








- Minimize weight
- Maximize stiffness
- Increase energy dissipation
- Increase mechanical damping
- Tune vibration absorption frequencies
- Joining thermally dissimilar materials

Non-structural advantages

- Decrease thermal conductivity
- Improve acoustical performance
- Provide air/fluid transport within material
- Electromagnetic and radiation shielding

Steel foams applications are just beginning to be developed, though some aluminum foam applications already exist on the commercial market, primarily in the mechanical, aerospace, and automotive industries. Nevertheless, steel foam bars, rods, foam core sandwich plates, and foam filled tubes have been created and tested at laboratory scale, at sizes on the order of 300 mm long by 50 mm diameter (Kremer, Liszkiewicz and Adkins 2004). This work provides proof of concept testing for the manufacture of steel foam components which are similar to those used in existing aluminum foam applications. Existing metallic foam applications have been summarized according to how the advantageous properties of foaming have been exercised in the design application. Structural and mechanical advantages are detailed in Table 7, and nonstructural advantages are explored in Table 8.

Table 7: Prototype and production structural applications for metal foams from selected literature.

Prototype/In-Production Applications:	Weight	Stiffness	Energy	Damping	Vibration	Importance to civil engineering	Reference
	X	X	X			Proof-of-concept, demonstrates steel foam bars, rods, sandwich plates, foam filled tubes can all be produced; demonstrates essentially all aluminum foam applications could be extended to steel foam.	(Kremer, Liszkiewicz and Adkins 2004)
	X	X				Mass production of metal foam panels is possible. Great variety of bending stiffness-to-weight regimes opened up by this possibility.	(Banhart and Seeliger 2008)
	X	X				Metal foam panels may take significant, even localized, loads, thus appropriate for floor slab, even heavily loaded parking garage (as load redistributes adequately).	(Hipke 2011)
	X	X				Metal foam beams can be produced that support high/typical structural loads and fatigue is not a unique problem as crane arms were fatigue tested.	(Banhart and Seeliger 2008)
		X		X	X	Metal foam panels can be tuned for desired vibration characteristics, could, e.g., be very important for high-speed rail applications.	(Neugebauer, et al. 2004)
	X	X			X	Shell structures possible with metal foams, tight dynamic performance constraints can be met. Metal foam explicitly cheaper than traditional sandwich panel in this case.	(Banhart and Seeliger 2008)
			X			Load transfer to the support limited by the foam yield. Slower deceleration reduces dynamic effects and enhances driver's safety.	(Lefebvre 2008), (Cardoso and Oliveira 2010)

Steel foams exhibit excellent stiffness to weight ratios when loaded in flexure (Ashby, et al. 2000). In particular, foam panels have better bending stiffness than solid steel sheets of the same weight (Banhart and Seeliger 2008). Therefore, the majority of existing structural applications seek to either minimize weight given stiffness constraints, or maximize stiffness given weight constraints, and the ability to control density through foaming makes these goals possible. For example, a manufactured 16 mm sandwich panel, with 1 mm steel sheet faces and the remainder foamed, has comparable bending stiffness to a solid steel plate 10mm thick, but at only 35% of the weight (Neugebauer, et al. 2004). As another example, a parking garage utilizing steel mesh reinforced metal foam floor slabs was proposed and full-scale load tests conducted (Hipke 2011). The design met standard strength and serviceability requirements, including deflection and strength under localized loading, and the use of the metal foam sandwich panels reduced the weight of the floors by 75% compared with traditional reinforced concrete decks.

Minimizing weight can have surprising benefits. The rigid body dynamics of a crane arm dictate that the mass of the arm controls the maximum lift, though a crane arm with the same stiffness but less weight can lift more with the same ballast. With this basic principle in mind a metal foam lifting arm, weighing 50% less than its solid steel counterpart was created (Banhart and Seeliger 2008). The crane successfully underwent high cycle fatigue testing and is currently in commercial production, thus demonstrating that heavily loaded beams under fatigue loading are possible with metal foams.

Additional mechanical examples include improvements in fabrication equipment (Neugebauer, et al. 2004) and the cone of a prototype rocket (Banhart and Seeliger 2008) that explore the structural benefits of increasing mechanical damping, and tuning the vibration frequency of components.

Energy dissipation through large compressive deformations at constant stress levels have been used in the automotive industry for crash protection (Lefebvre 2008). Once kinetic energy is completely dissipated through plastic deformation, the crash is arrested and the vehicle comes to rest. The yield stress of the foam is designed such that it does not substantially change the load carrying characteristics of the main car frame. Vehicles equipped with foamed elements decelerate over a longer distance and period of time, thereby reducing accelerations experienced by the vehicle occupants (Cardoso and Oliveira 2010). The ability to absorb energy of impact or blast while limiting stress levels is crucial to the design of robust hardening systems for civil infrastructure.

An important structural advantage for metallic foams that has not been demonstrated to date is the mitigation of buckling both for rods and plates, and the conversion of limit states from unstable buckling modes with little to no energy dissipation to stable modes exhibiting crushing or post-buckling behavior. In addition, applications with high strain rate, low-cycle fatigue have not been explored. Existing structural advantages demonstrate the potential for steel foam in civil applications, but much work remains for these advantages to be realized in practice.

Example non-structural applications for metallic foams utilize benefits of the material such as thermal conductivity, fire retardance, acoustics, gas and fluid transport, and electromagnetic shielding (summarized in Table 8). Existing applications are largely in the mechanical engineering domain, so for each application, the potential importance to civil engineering is also discussed.

Table 8: Prototype and production non-structural applications of metal foams

Prototype / In-Production Applications:	Thermal Resist	Fire Resist	Acoustic Absorb	Fluid Transport	E/M Shielding	Importance to civil engineering	Reference
Industrial chill forms and generic foamed parts	X					Reduced thermal conductivity; could help thermal bridging in steel applications.	(Neugebauer, et al. 2004), (Ashby, et al. 2000)
Metal-ceramic heat shield and biomedical implants	X					Metal foams allow materials of disparate thermal expansion to be joined.	(Reisgen, Olschok and Longerich 2010), (Shirzadi, Zhu and Bhadeshia 2008), (Levine 2008)
Fire retarders	X	X				Potential for integral fire resistance in steel members.	(Coquard, Rochais and Baillis 2010), (Lu and Chen 1999)
Heat exchanger	X			X		Open-cell metal foams allow fluid transport, potential for walls to be integrated with HVAC.	(Ashby, et al. 2000), (Reisgen, Olschok and Longerich 2010)
Sound absorber on bridge, in auto exhaust, and general use			X			Potential to integrate sound absorption and vibration control into bridge/rail design.	(Ashby, et al. 2000), (Gohler, et al. 2001), (Bao and Han 2009)
Electromagnetic shield and radiation shield					X	Potential for shielding buried structures, components of critical facilities.	(Losito, D. and Dimiccolim 2010), (Xu, Bourham and Rabiei 2010)

Key Section Findings

To model steel foam in a finite element analysis, a plasticity model such as that proposed by Deshpande and Fleck must be employed.

Cellular steel exhibits particular advantages in stiffness to weight ratio, energy dissipation, vibration control, and thermal conductivity.

Potential applications include parking garages, beams, crash absorbers, integral bridge vibration absorption, and electromagnetic shielding of critical facilities.

CHAPTER 3 EXPERIMENTAL TESTS

3.1 Testing Standards

Key Section Objectives

Explore the testing standards which currently exist and their applicability to metal foams.

Experimental measurements of steel foam properties vary significantly not only among different manufacturing methods, but also among different research groups, even within nominally similar specimens (Lim, Smith and McDowell 2002). Bias in the data exists because of a strong correlation between manufacturing type and research group; for example, only two research teams work on gasar manufacturing: Nakajima, Ikeda, and Hyun (2003) and Shapovalov and Boyko (2001). Variability is also due to the lack of standardization in testing (see Table 9). For example, authors have considered yield stress to occur at strain offsets from 0.2% to 5%; sample sizes vary significantly, particularly for tensile and shear tests; and many authors do not describe how samples and testing apparatus were prepared.

Recently, there has been some effort to standardize testing of metal foams. Japanese and German (Krupp, et al. 2007) standards for compression testing of metal foams have been accepted, and the International Standards Organization (ISO) recently combined these two standards into its own international standard for compression testing of metal foams (ISO/DIS 13314). However, there are no standards that currently exist for tensile, shear, cyclic, or other mechanical tests on metal foams. There are analogues in testing of cellular plastics and ceramics, as listed in Table 9, or in certain testing procedures for solid metals, but metal foam testing procedures must be devised by analogy to these standards.

Table 9: Table of comparable American and international testing standards for metal foams.

Test	Similar Standards	Standard Is Designed For
Cell openness	ISO 2738	Metal foams
	ISO 4590, ASTM D6226	Cellular plastics
Linear dimensions	ISO 1923	Cellular plastics
	ISO 2738	Metal foams
Density	ISO 845, ASTM D1622	Cellular plastics
	ASTM C271	Sandwich foam core
Cell size	ISO 24003	Metal foams
	ASTM D3576	Cellular plastics
Compression	ISO/DIS 13314(E), DIN 50134, JIS H7902	Metal foams
	ISO 844, ASTM D1621	Cellular plastics
Tension	ISO 1926, ASTM D1623	Cellular plastics
	ASTM C1674	Honeycomb ceramics
Shear	ASTM C273, DIN 53295	Sandwich foam core
	ISO 1922	Cellular plastics
Shear fatigue	ASTM C394	Sandwich foam core
Compressive creep	ISO 7616, ISO 7850	Cellular plastics
Bending	ISO 1209-1	Cellular plastics
Elastic modulus	ISO 1209-2	Cellular plastics
Poisson's ratio	ASTM D6790	Honeycomb core materials

Key Section Findings

While there is some current effort to create testing standards specifically for metal foams, there is generally very poor standardization of testing procedures and the best analogues are generally in cellular plastics.

3.2 Testing Procedure

Key Section Objectives

Describe the specimens available for testing and their machinability.

Discuss the procedures used in testing.

Two types of steel foams were available for testing, including several hollow spheres foam samples, and one block of PCM foam. The former was acquired from Fraunhofer Institute for Advanced Materials (IFAM) in Dresden, Germany, while the latter was sourced from MER Corporation in Tucson, Arizona, USA. Precise inventories are described below.

Sixty-six blocks of hollow spheres steel foam samples were available for experimental testing. Each block measures approximately 52mm by 55mm by 260mm, is made of a mild carbon steel, and has a relative density of approximately 14%. After inquiries to the

manufacturer, Fraunhofer, the company representative stated that the precise alloy composition cannot be known due to the nature of their production process (Goehler 2010). While the specimens would ideally be prepared for testing exactly according to existing testing standards for either metal foam or solid steel, the limited machinability of hollow spheres steel foam samples available often restricted this. Attempts to cut the material have shown that milling and likely any type of drilling is impossible, as instead of cutting through the material, the spinning bit breaks off spheres at their welds and throws them off. For similar reasons, a lathe would likely also cause similar problems, though this was not tested. While previous published testing suggested that electrical discharge machining would be the most successful method of machining, the cost and difficulty of this method rendered this method prohibitive. The only successful method of machining readily available at the University of Massachusetts was to use a band saw. Further, it was found that a band saw operating at slower speeds provides a better cut than a band saw operating at higher speeds. At higher speeds, the saw appears to partially melt the sphere walls, while a slower speed tears some sphere walls slightly but otherwise leaves them cleanly cut.

Only one block of PCM foam was available for testing, measuring approximately 110mm by 110mm by 37mm. However, the PCM foam was also easily machined using a mill and so could be easily cut to have flat surfaces and accurate right angles. Andrews et al (2001) showed that size effects reduced the apparent strength of experimental specimens with dimensions equal to less than 8-10 pore diameters to a side. For the PCM foam, the diameter of the largest pores was on the order of tenths of millimeters, so the minimum 8-10 pore diameters was easily met in even the smallest samples in the directions perpendicular to the voids. However, the voids were also highly elongated, having lengths of up to about 20mm. As the pores were oriented with their long axis running along the shortest dimension of the material, the 37mm

height, it was impossible to meet the 8-10 pore diameter minimum (Andrews, et al. 2001). Nevertheless, testing was performed despite this restriction.

All mechanical tests were performed upon a screw-driven Instron 3369 testing machine. In order to process resulting data, the Instron testing machine was set to export raw data consisting of elapsed time, crosshead extension, load cell values, and, if used in the given test, extensometer strain into a .csv comma-separated values text file. These .csv files were then imported into MatLab, and processed using custom-written scripts to convert the data into stresses, strains, Poisson's ratio values, and graphs of these results.

3.2.1 Microscopy

Understanding the precise nature of the material's microstructure is extremely important for accurate computational simulations. The features of interest on the hollow spheres foams are particularly the sphere wall thickness, weld diameter, and weld length. All of these features would be measured on the scale of hundredths of millimeters, which is possible under an optical light microscope. The Conte Polymer Science Center at the University of Massachusetts Amherst possesses such microscopes and the tools necessary to make measurements, so examination were done at this location. Through experimenting with different cutting methods and cutting speeds, it has been determined that a sharp vertical band saw operating at low speed (near to the machine's minimum speed) provides the cleanest cut. Thin slices of approximately 5mm thickness were cut using such a method and then examined under the microscope. While it is not possible to measure every weld and hollow sphere on a given block of material, random samples were observed and their measurements recorded. This data was then entered into MatLab, approximate distribution was determined visually through

histograms, and then means and standard deviation were calculated. This data is then used to inform the input parameters for computational simulations.

In order to characterize the steel foam by a set of discrete parameters, various characteristics of the material's microstructure were measured and recorded with the aid of an Olympus optical microscope. These parameters include the outer diameter and the sphere wall thickness of the hollow spheres, as well as the diameter of the weld areas connecting spheres. These parameters correspond to those used in the computational simulations (see Chapter 4), and are also considered sufficient to represent the hollow spheres geometry.

Images were viewed by directing the optical microscope's output to a computer, and observing the live display in a software imaging package along with a size scale. While the software did not provide a means of measuring between arbitrary points, measurements were performed by calibrating a standard ruler to the image scale and then measuring on screen with a ruler. The subjectivity of these measurements suggested that attempting to make measurements more precisely through other means would not have yielded results that were any more accurate.

3.2.1.1 Hollow Spheres Foam

The sphere diameter was measured on the uncut face of the material so as to ensure that no incorrectly small measurements would be obtained from spheres that were cut more than halfway through. See Figure 6 for a sample image from which measurements were taken. Dimensions of each sphere vary throughout the material, so random spheres were measured while ensuring that no one sphere was measured more than once. Further, an occasional damaged, highly deformed, or badly corroded sphere was excluded from being measured, as they were considered not to be representative of the overall geometry. Such criteria removed

fewer than 5% of spheres from the sample frame. It was also assumed that the hollow spheres are close enough to being axisymmetric that only a single measurement of diameter was taken for each sphere, but was taken along a random direction for which a precise measurement could be obtained. Some directions were more difficult to obtain a precise measurement along, particularly around welds, where the division between where one sphere ends and the next begins becomes difficult to determine. When a measurement was taken, the ruler was placed on a point on one side of the sphere, and then pivoted about that point until the largest measurement was observed, and then this value was recorded, thereby ensuring that the measurement was representative of the full diameter.

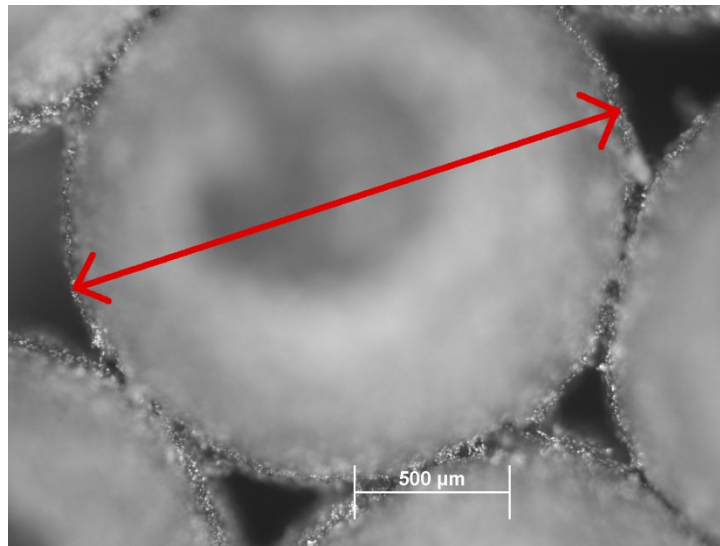


Figure 6: Sample image of a sphere diameter microscopy measurement.

Weld size was measured from the same uncut face of the steel foam in order to ensure that the full weld diameter would be measured. Again, random welds were measured while making sure that no welds were repeated. The value was obtained by measuring from one cusp between welds to the next, as shown in Figure 7.

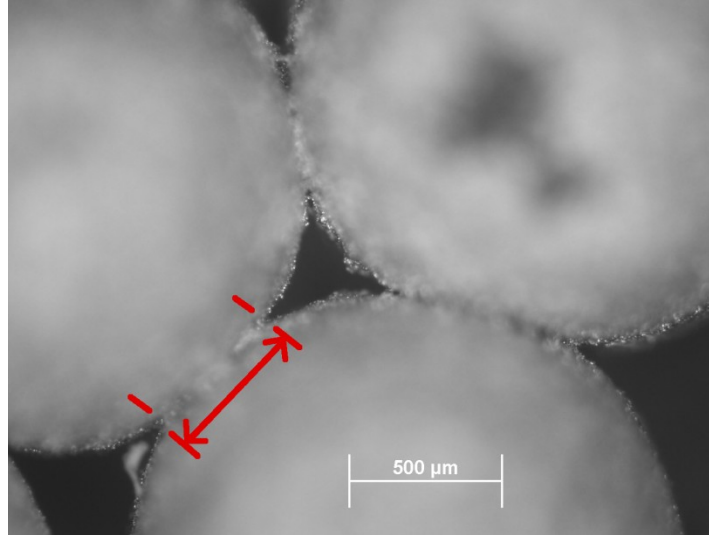


Figure 7: Sample image of a weld size microscopy measurement.

Finally, the sphere wall thickness could only be measured from a cut face of the material. However, band saw cuts were too inaccurate and caused too much tearing and bending of the sphere walls. Therefore, faces of the material which had been cut by electrical discharge machining (EDM) by Fraunhofer IFAM were used for measurements. However, it is likely that many spheres were not cut straight through their centers, which would result in cuts not perpendicular to the wall and therefore measurements of the wall thickness being artificially large. To partially account for this, only spheres that appeared to be at least close to the measured average diameter were measured for their wall thickness. However, this error is still inherent in the wall thickness measurements. Further, the wall thickness is not uniform throughout the entire circumference due to imprecisions in the manufacturing method as well as microporosity within the walls themselves. When measurements were made, a section which visually appeared to be average within a given circumference was measured (see Figure 8). The wall thickness parameter has the least confidence of the three parameters due to these several sources of error.

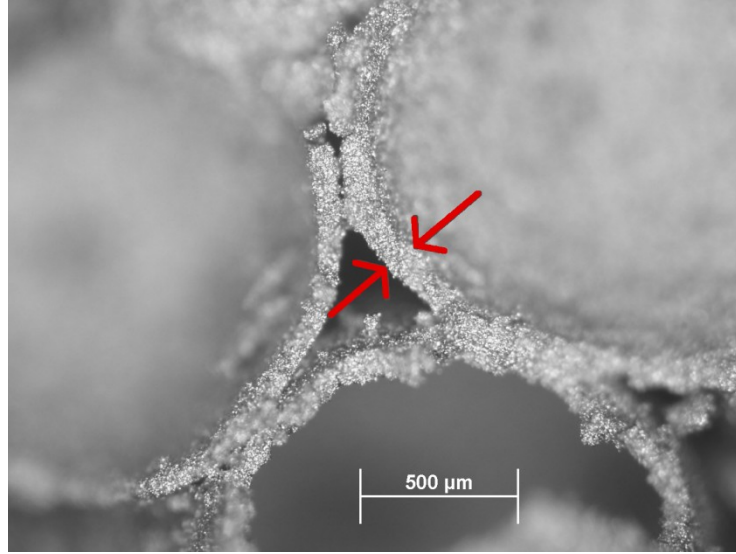


Figure 8: Sample image of a sphere wall thickness microscopy measurement.

3.2.1.2 PCM Foam

PCM foams had three different types of faces available for measurements under the microscope: cut parallel to pores, cut perpendicular to pores, and tensile fracture faces perpendicular to pores.

On the faces cut parallel to pores, it was possible to measure the length of each pore, and the angle at which each pore was oriented along the plane of the face. The angle of orientation of the voids was observed to be so close to vertical that it was not possible to take an accurate measurement of the angle. It was therefore assumed that the pore length could be measured along a cut made parallel to the pores, though it was still possible that pores could have dived into the material, artificially decreasing the measureable lengths. As the shortest pores were about 2 mm in length (see Figure 9), they were measured without the aid of a microscope. Nominally random pores were measured while ensuring that no one pore was measured twice, and then the results were tabulated. See Figure 10 for a microscopy image of the face cut parallel to pores.

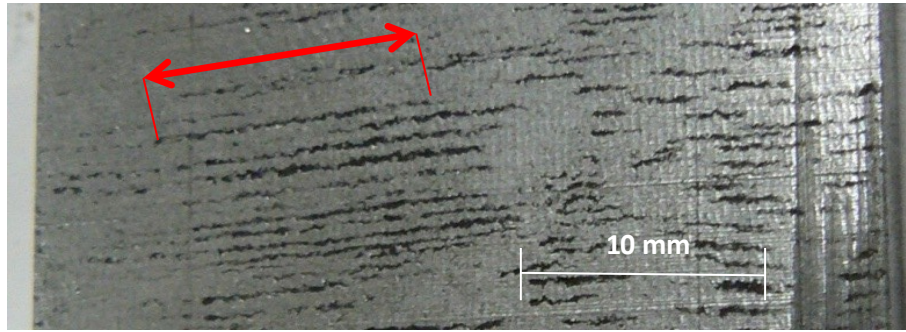


Figure 9: Macro photograph of measuring the length of a pore on the PCM material. The full 37mm height of the material is shown.

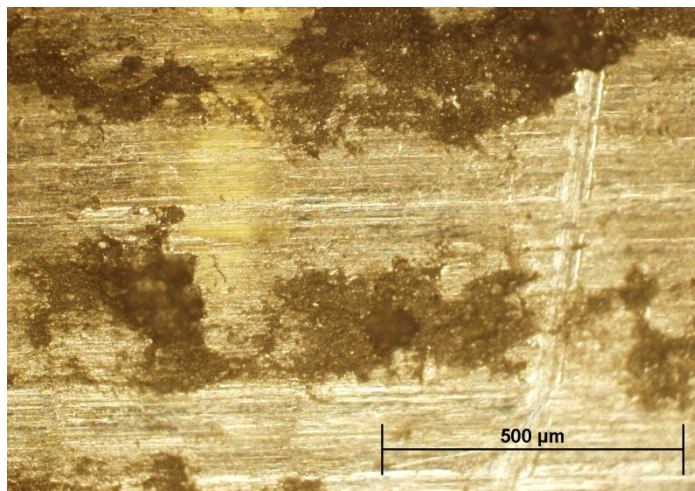


Figure 10: Microscopy image of a PCM face cut parallel to pores.

Perpendicular to the pores, measurements were desired for the diameter of the pores and the quantity of spheres per unit area. The tensile fracture face and the cut face each provided their own unique surfaces for taking such measurements. The tensile fracture face might have some Poisson contraction effects, and was far from flat. On the other hand, it also did not suffer the disadvantage of having any microscopic burrs or other debris from the cutting process. All cut surfaces were rough cut with a band saw and then milled. Measurements of the pore diameter were taken by means of visually searching for the largest actual diameter measureable for the pore, attempting not to measure any microscopic chip in the metal or other microporosity as being part of the pore measurement. While this was a subjective judgment, it

was believed that adequate enough decisions could be made, and there was no discernible method of setting an objective criterion for this measurement. It was believed that an alternative of attempting to take an average value for the diameter of a given pore would have resulted in artificially low diameters because it would have been measuring surface deformities, particularly on the milled face. See Figure 11 for a depiction of how diameters were measured upon microscopy images of both surfaces. The measurement of pores per unit area was made by counting the pores present in a given area.

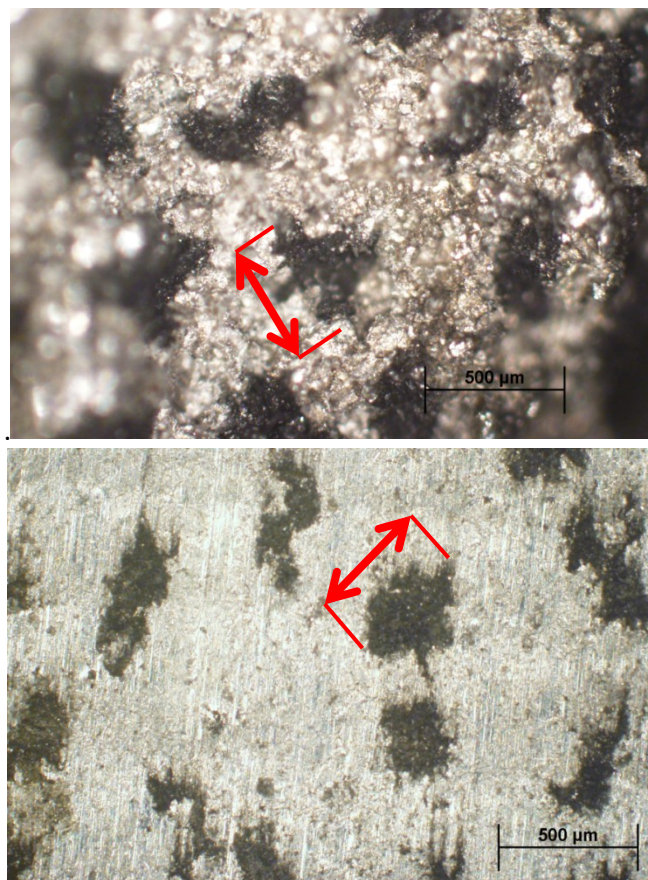


Figure 11: Microscopy images depicting how void diameters were measured. The top image shows a tensile fracture surface, while the bottom shows a milled surface. The scale is the same on both images.

3.2.2 Compression Testing

Compression specimens, the only specimens for which a testing standard specifically written for metal foams exists, are both the most physically simple and least affected by machinability. The standard, ISO/DIS 13314 calls for rectangular prism specimens with a height equal to between 1.5 and 2.0 times the width, with the width and length being equal. All dimensions should be at least 8-10 times the diameter of the largest void, which is the sphere diameter for hollow spheres foams, or the length of the voids for PCM foams (Andrews, et al. 2001). The testing standard specifies that samples should be placed between two flat platens, lubricated with an “appropriate lubricant”, and then compressed under displacement control. A screw-driven Instron 3369 machine was used, and two different lubricants were tested: a “Dri Slide” molybdenum disulphide and graphite aerosol lubricant designed for pressures up to 689 MPa (100,000 psi), and an “X-tra Heavy Duty Wheel Bearing” automobile axle grease. After testing both lubricants, the automobile axle grease was determined to be superior and all subsequent tests were performed with this lubricant.

3.2.2.1 Hollow Spheres Foam

A band saw was easily used to cut the straight lines for compression tests in hollow spheres. The only deviation from the ISO 13314 standard resulted from the fact that the cross-section of the sample blocks as delivered was slightly rectangular, at approximately 52mm by 55mm. Rather than attempt to cut a 3mm sliver of material, this was left in its slight rectangular shape. However, in order to perform tests to greater compressive stresses on the available testing machine, smaller cross-section specimens were also cut, though still having dimensions of at least 10 times the sphere diameter. These were cut to square cross-sections of

approximately 25mm to a side. See Figure 12 for an image of one of the full-size samples in the midst of a compression test.

Three types of uniaxial compressive tests were performed to evaluate the mechanical properties of the available steel foam with the one available extensometer. The displacement rate was between 0.5mm/min and 1.0mm/min (equivalent to strain rates of between 0.003/min and 0.015/min). Three tests each of densification strain and Poisson's ratio were performed, and six tests of the elastic modulus were performed. See Table 10 for details of testing parameters for each test.

Table 10: Table of the three types of compression tests performed upon hollow spheres foam.

Measurement	Loading type	Strain rate / min	Strain acquisition	Specimen size
Densification strain	Monotonic compression	0.015	Crosshead displacement	25mm x 25mm x 55mm (± 5%)
Poisson's ratio	Monotonic compression	0.015	Transverse extensometer	52mm x 55mm x 80mm (± 3%)
Elastic modulus / yield stress	Compression, unloadings spaced at 0.5% to 1.0% strain	0.015 or 0.007 loading 0.007 or 0.004 unloading	Loading direction extensometer	52mm x 55mm x [80mm or 140mm] (± 2%)

Initially, to verify the extensometer and crosshead extension data as well, the crosshead extension rate was set at 1mm per minute and periodic manual measurements were taken while running a "Poisson's ratio" type test. Every two minutes, equal to every 2mm of extension, transverse measurements were taken using a caliper at the center of the material's height. Further, a longitudinal measurement of the space between the platens was taken every 10 minutes, starting with a measurement at 5 minutes. These measurements were taken while the machine was loading. The calipers were accurate to 0.01 mm, though the heterogeneity of the material itself as well as simple human error probably resulted in an accuracy of only about 0.05 to 0.1mm. The extensometer was verified to be accurate within 3% of caliper readings, and the crosshead was verified to be accurate to within 5% of caliper readings. Later tests, however,

would show that the crosshead data only remains accurate for low forces (under about 5,000 N) and relatively compliant materials (with elastic moduli less than about 2500 MPa).

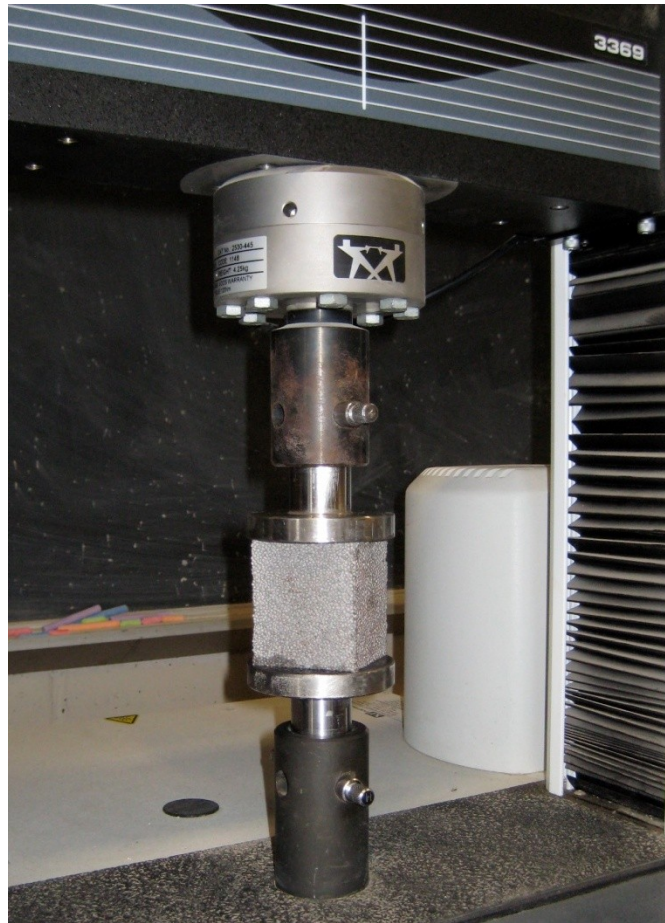


Figure 12: Image of a full-size hollow spheres specimen during a compression test.

3.2.2.2 PCM Foam

Due to the much smaller size of the material available, only one type of destructive compression test was performed upon the PCM foams: a monotonic compression test. However, differing results were expected based upon whether the material was compressed with its pores oriented transversely or longitudinally to the direction of loading. With pores oriented longitudinally, samples measured 9mm by 9mm by 14mm ($\pm 10\%$), and with pores oriented transversely, samples measured 11mm by 11mm by 17mm ($\pm 10\%$). The smallest available extensometer had a gauge length of 51mm and so could not be used on these tests.

One verification test was also performed with a sample measuring 25mm by 25mm by 37mm, with pores oriented longitudinally, upon a hydraulic Tinius-Olson testing machine. Finally, in order to obtain an accurate elastic modulus value, one non-destructive test was performed with the extensometer attached to a large sample measuring 35mm by 42mm by 106mm, with pores oriented transversely.

3.2.3 Tension Testing

In the absence of a tension testing standard specifically designed for metal foams, the ASTM E8 standard, "Tension Testing of Metallic Materials," for tension testing of solid metal samples was utilized instead. Tension specimens were machined to a dog bone shape as described in ASTM E8 for "plate-type" specimens. Significant deviations from this standard were necessary for both hollow spheres and PCM testing, however, with the former restricted by difficulties in gripping the highly compliant material, and the latter restricted by quantity of material available.

3.2.3.1 Hollow Spheres Foam

To efficiently make use of the material available, samples were prepared to a thickness of 25mm, reduced length of 55mm, reduced width of 25mm, and grip sections of 55mm width using the remainder of the roughly 225mm total length, as shown in Figure 13. The only deviation from the testing standard for the size is that the region between the reduced section and the grip section is supposed to be filleted to prevent stress concentrations, but due to the relative impossibility of using a band saw to make a fillet, these transitions are beveled instead using the band saw. It is judged that the microstructure itself should provide greater stress concentrations than a macroscopic face intersection.

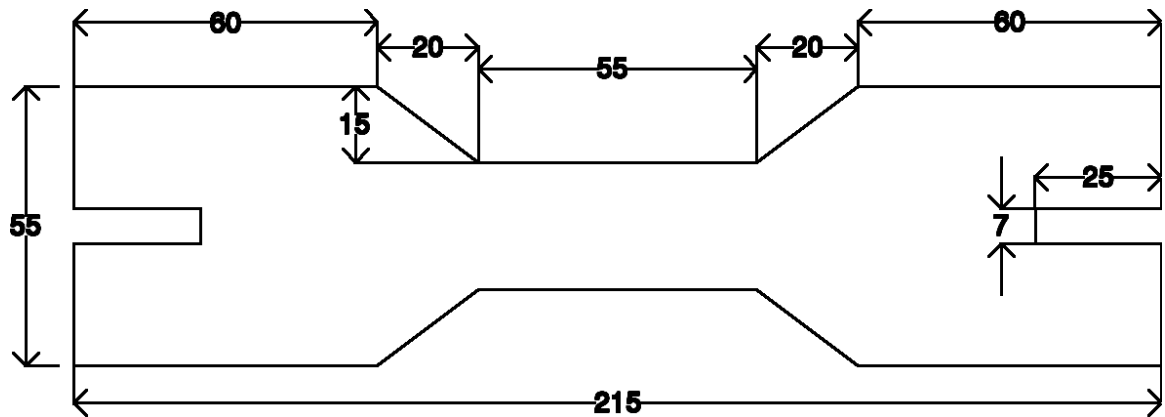


Figure 13: Dimensioned drawing of a hollow spheres tension specimen (all dimensions in mm).

The ASTM E8 standard specifies that the sample should be gripped through screw threads, friction, or a lip on the sample, but none of these options are practical for steel foam. Screw threads are not possible due to the material heterogeneity, and either friction or latching onto a lip would not be possible as the material would crush as the gripping force was applied, leading to either distorted results or an impossible test. Therefore, a high-strength epoxy was used instead. The slots at either end of the specimen were filled with epoxy and then the solid steel platens were inserted into the slots, attaching the two together (see Figure 14). As the ultimate tensile strength on hollow spheres foams in particular is relatively low, epoxies are a viable option. An initial test of this epoxy using a small rectangular prism sample failed, but in a ductile manner, suggesting an insufficient cure time. However, allowing the epoxy to cure overnight allowed the epoxy to hold and the sample failed appropriately within the material itself. Two different epoxies were utilized: JB Bond, and Devcon High-Strength Plastic Welder. The extensometer was used to measure the specimen elongation on the three tension specimens tested.

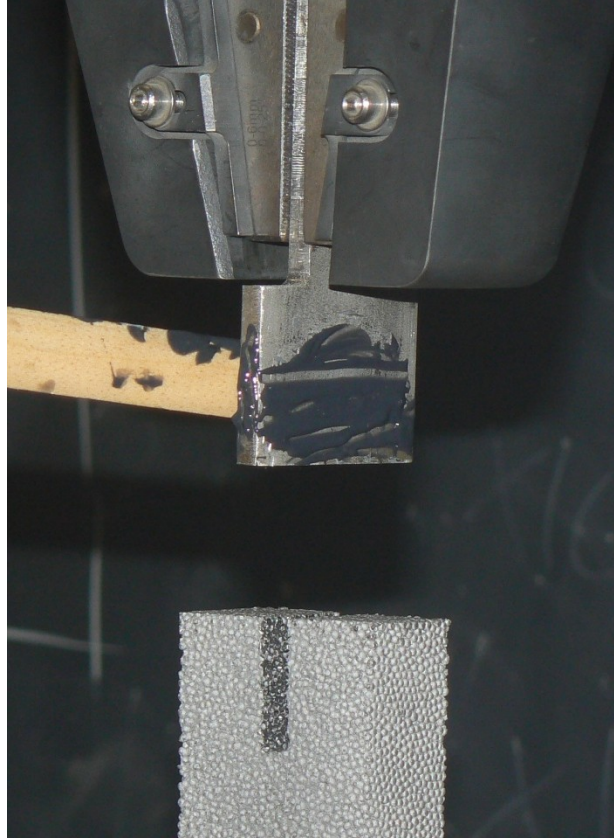


Figure 14: Photo of epoxying a tension platen. The testing specimen with slot cut into it is located immediately below the platen.

3.2.3.2 PCM Foam

The PCM foam was significantly more limited in quantity, but also much more easily machined. The same “plate-type” specimen described in ASTM E8 could therefore still be used, just scaled down to smaller dimensions. As the height of the available block was 37mm, the height of the specimens was kept at 37mm. ASTM E8 calls for a thickness equal to the “thickness of the material”. Since specimens were being cut, the optimal thickness could be chosen by other means. The relevant restriction was in how to grip the material. Given extremely high compression strengths measured (see section 3.2.2.2 PCM Foam), gripping the material with wedge grips was presumed to be possible. The maximum thickness that the available wedge grips could hold was 6 mm, so this was used as the thickness. This thickness also allowed for the

minimum 6-8 voids to be present across the cross-section; note that this a slightly relaxed restriction from compression, which required 8-10 voids diameters across the cross-section (Andrews, et al. 2001). A direct scaling of the ASTM E8 standard would call for the reduced length to be 4-5 mm. As this seemed unreasonable and could be fewer than 6-8 voids across, the width was instead set at 15 mm, which was a convenient width for machining. As a mill could be used for machining, a fillet could easily be formed in the transition between the grip section and the reduced section. See Figure 15 for a dimensioned sketch of a sample.

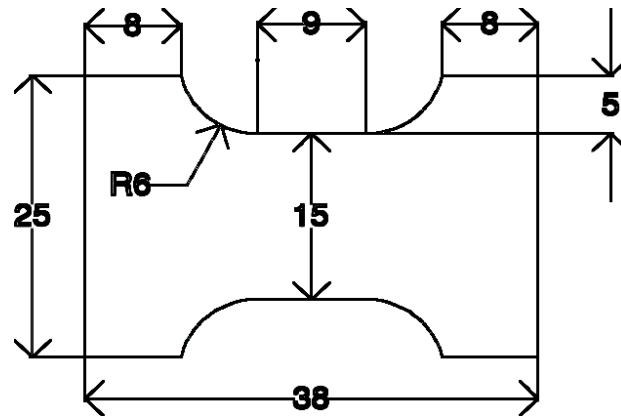


Figure 15: Dimensioned drawing of a PCM tension specimen (all dimensions in mm).

To adequately test the material, two sets of tension specimens were prepared: one with pores oriented longitudinally to the testing direction, and the other oriented transversely. Two specimens were tested for each orientation. An image of a mounted tension specimen is shown in Figure 16.

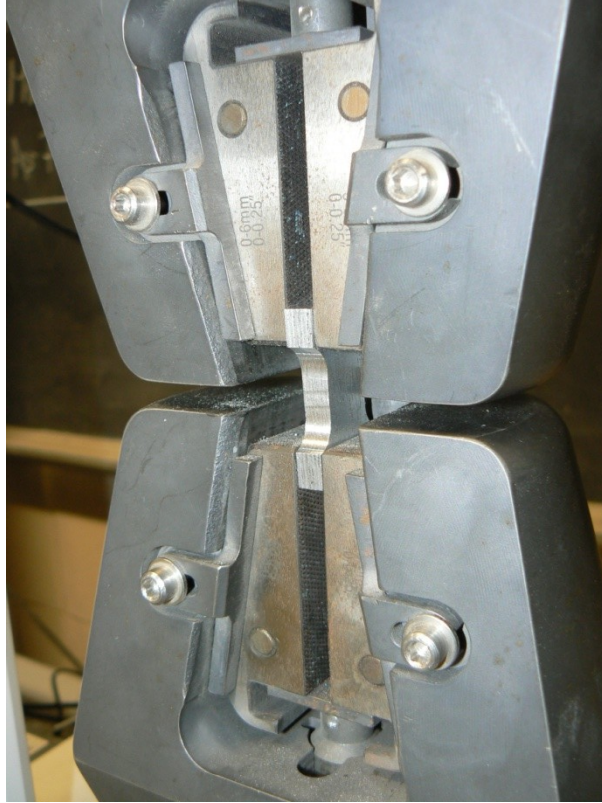


Figure 16: Specimen of PCM foam mounted in the wedge grips and ready for tension testing.

3.2.4 Shear Testing

While the standard shear test for structural materials is a torsion test, as specified by ASTM E143, and is the preferred method for testing, there is no torsional testing machine available at the University of Massachusetts for experimental testing. Therefore, experimental testing was performed according to the testing standard for shear testing of rigid cellular plastics, ISO 1922, which involves attaching a thin rectangular sample to two rigid platens, and then pulling one platen in a direction parallel to the platen's face, as shown in the diagram of Figure 17. As PCM foams failed in shear during compression tests (see section 3.3.2.2 PCM Foam), there was assumed to be little value in attempting specific shear tests of this foam. Therefore, only hollow spheres foams were tested according to this procedure.

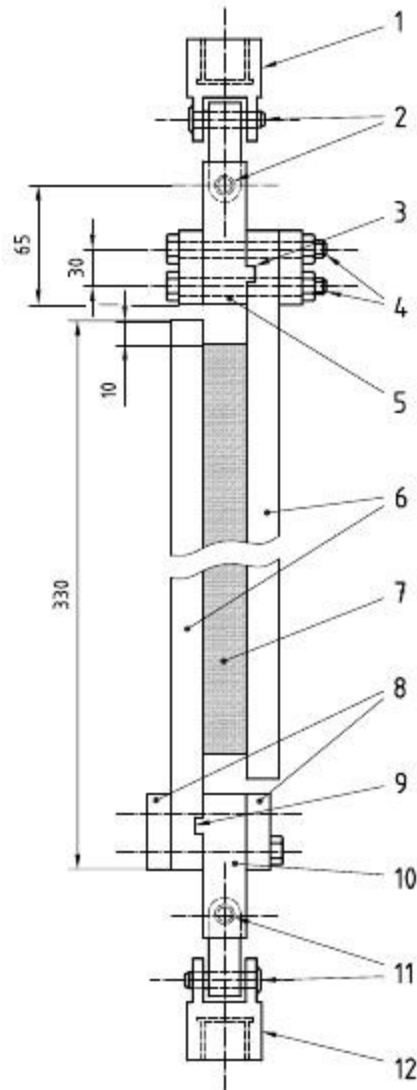


Figure 17: Drawing of shear testing apparatus specified in ISO 1922, the shear testing standard for rigid plastics (Image from ISO 1922). All dimensions shown are in mm.

The ISO 1922 testing standard calls for specimens of size 25mm by 50mm by 250mm.

After multiple attempts at performing such tests, however, it was found to not be possible to machine a flat enough surface on the hollow spheres foam so that the entire surface would end up laminated by the epoxy, as only limited quantities of epoxy strong enough to hold the material was available. Therefore, the ISO 1922 standard dimensions were reduced; the 25mm thickness was kept, but the depth was reduced from 50mm to 25mm, and then height from 250mm to 55mm. Three such tests were performed. The same Devcon Plastic Welder epoxy

used for the tension tests (see section 3.2.3.1 Hollow Spheres Foam) was used for attaching the samples to the platens for these shear tests. The ISO 1922 standard was followed precisely for the remainder of the testing procedure, and no further deviations were necessitated by the use of steel foam in the tests. Platens for use in this test were custom manufactured, as none previously existed that would serve the purpose. In order to accurately measure strains, an extensometer was attached between the lower platen and the upper. As the hollow spheres foam is neither particularly stiff nor strong, platen measurements were considered accurate enough. A photograph of the final setup is shown in Figure 18.



Figure 18: The shear testing apparatus, based upon ISO 1922, loaded with a sample and ready for testing. The extensometer is attached in the upper right.

Key Section Findings

Roughly twenty specimens of hollow spheres foam measuring approximately 52mm by 55mm by 250mm were tested, and one specimen of 110mm by 110mm by 37mm of PCM foam was tested.

Compression, tension, and shear testing procedures were described, all based closely upon various ASTM or ISO testing standards.

3.3 Results

Key Section Objectives

Discuss the results from compression, tension, and shear testing of hollow spheres testing.

Give results from compression and tension testing of PCM foams.

Numerous compression tests, tension tests, and shear tests have been performed on both hollow spheres and PCM steel foams. Optical microscopy measurements have been taken of both foams. Results are described in this section. Procedures for each of these tests is described in the above section 3.2 Testing Procedure. A summary of all of the tests performed is shown in Table 11.

Table 11: Summary table of all experimental tests performed.

	Test	# of tests	Sample size (mm)	# of blocks	Basic Procedure
Microscopy	HS – Sphere Diameter	60	52x55x5	0	Two sets of sphere diameter measurements
	HS – Weld Diameter	50	52x55x5	0	Two sets of weld diameter measurements
	HS – Wall Thickness	25	52x55x5	0	One set of wall thickness measurements
	PCM – Void Diameter	71	25x37x6	0	Measurements of void diameter on one tensile fracture surface, and one cut surface
	PCM – Void Length	48	25x37x6	0	Two sets of void length measurements
	PCM – Pore Concentration	10	25x37x6	0	10 measurements of pore concentration
Uniaxial Compression	HS – Elastic Modulus	6	52x55x[80 140]	3	Compression with repeated unloadings
	HS – Densification	3	25x25x55	0.5	Compression past densification
	HS – Poisson's Ratio	3	52x55x80	1.5	Compression with transverse extensometer
	HS – Base Metal	1	8x10x10	0.1	Compression to base metal yield point
	PCM – Longitudinal Orientation	4	9x9x14	0.2	Compression until ultimate failure
	PCM – Transverse Orientation	3	11x11x17	0.1	Compression until ultimate failure
	PCM – Elastic Modulus	1	37x43x108	0	Non-destructive compression in elastic range
Uniaxial Tension	HS – Tension	3	22x55x215	1.5	Tension of dog bone shape held with epoxy
	PCM – Longitudinal Orientation	2	6x25x37	0.1	Tension of dog bone plate held by wedge grips
	PCM – Transverse Orientation	2	6x25x37	0.1	Tension of dog bone plate held by wedge grips
Uniaxial Shear	HS – Shear	3	25x25x55	0.5	Shear of rectangular block held with epoxy

3.3.1 Microscopy

Microscopy measurements were taken for both PCM and hollow spheres in sufficient quantity as to obtain mean and standard deviation values. These values are obtained primarily for the purpose of providing accurate inputs into the Metal Foams Simulator computer program described in Chapter 4. Reported in the following sections are the summary results from the microscopy studies.

3.3.1.1 Hollow Spheres Foam

Individual measurements of sphere diameter, weld size, and wall thickness were taken from two different samples in order to obtain reliable values for average and standard deviation. The results are shown in Table 12. No significant differences in values were observed between the two measured samples. The results of these microscopy measurements changed the previous assumptions of both sphere diameter and wall thickness, which had been 2mm and 0.13mm, respectively. The 2mm value had been based upon the order invoice from Fraunhofer IFAM, and the 0.13mm value had been based upon the 20% relative density also quoted in that invoice and determined through computational simulations (see Chapter 4). The reduction in both values suggested that our 20% relative density value may also be inaccurate, and so a scale was used to measure the weight of a few blocks of known volume. The scale confirmed a lower relative density at 14-15%, showing that the invoiced relative density was incorrect.

Table 12: Results of hollow spheres microscopy study, showing mean and standard deviation of values in each sample.

	Sphere Diameter (mm)		Weld Diameter (mm)		Wall Thickness (mm)
	Sample 1	Sample 2	Sample 1	Sample 2	Sample 3
Mean	1.87	1.84	0.50	0.45	0.08
Standard Deviation	0.10	0.07	0.10	0.10	0.01
# of Measurements	40	20	25	25	25

3.3.1.2 PCM Foam

Measurements were taken of pore diameter, length, and concentration, with diameter being measured on both a cut surface and a tensile fracture surface. Results are shown in No values were provided by the manufacturer.

Table 13. No previous assumptions had been made as to these values. The differences between void maximum widths measured from the cut surface and the tensile fracture surface are not statistically significant, but a real difference may well exist due to microscopic burrs or

other damage produced during the milling process. The relative densities of three cut samples were measured, consistently showing a value at 34% based upon weight divided by volume measurements. No values were provided by the manufacturer.

Table 13: Results of PCM microscopy study, showing mean and standard deviation of values in each sample.

	Pore Diameter (mm)		Pore Length (mm)	Pores per mm ²
	Cut Surface	Tension Surface	Cut Surface	Cut Surface
Mean	0.32	0.34	5.10	1.4
Standard Deviation	0.05	0.06	2.17	0.38
# of Measurements	50	21	48	10, totaling 208 mm ²

3.3.2 Compression Testing

The plurality of experimental tests performed were compression tests, due to the ease of their execution and the extensive data that could be obtained from them. Also, most potential applications make use of steel foams primarily in compression. Elastic and plastic moduli, yield stress, densification stress, and Poisson's ratio values could all be obtained through various forms of compression tests. All of these were obtained for hollow spheres foams, while all but Poisson's ratio data were obtained in PCM tests. The following sections detail all the results obtained in experimental testing upon both types of steel foams.

3.3.2.1 Hollow Spheres Foam

Three types of compression tests were performed upon hollow spheres foams, as described in section 3.2.2.1 Hollow Spheres Foam. These included elastic unloading modulus, densification strain, and Poisson's ratio tests. A summary of all compressive hollow spheres results is shown in Table 14 at the end of this section.

Tests with multiple unloadings were repeated six times with an extensometer used to measure strain in the direction of applied load, with two of the tests using a larger specimen height. An image of the test of a normal-height specimen in progress is shown in Figure 19. As the extensometer was used in the longitudinal direction, these tests were used to accurately measure the elastic modulus and yield strain of the material in addition to unloading properties.

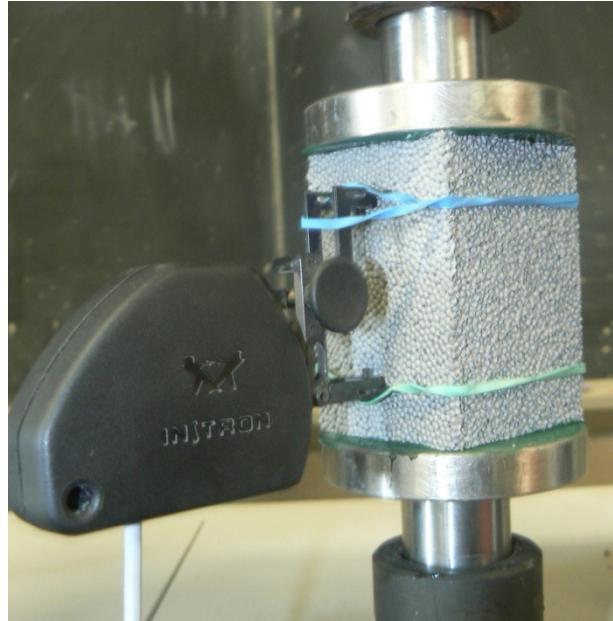


Figure 19: An elastic unloading modulus test upon a normal-height specimen in progress.

Longitudinal strain ε_z was recorded using both the extensometer and the crosshead displacement of the testing machine. As the extensometer only has a 10% movement, tests were stopped at 0.1 strain. Before strains of approximately 0.05, the extensometer-based and crosshead-based strains differed substantially, with the extensometer measuring lower strain values than the crosshead. After approximately 0.05 applied strain, the two values were within 5% of one another, though the crosshead values still showed much lower stiffnesses during both unloading and reloading stages of unloading cycles as compared to the extensometer data. This observation lends support to the use of crosshead displacement for measuring ε_z during the densification and Poisson's ratio tests, where larger strains were the focus. However, it also

suggests that the crosshead displacement should be considered very unreliable at strains less than 0.05.

To attempt to quantify the effect of seating of the specimens on measured strain, specimens of identical cross section (52 mm x 55 mm) but different heights (80 mm and 140 mm) were tested. It was observed that in the 140 mm specimens, the extensometer strains were identical to those recorded for the 80 mm specimens, but the strains computed from the crosshead displacement were 40% lower for the 140 mm specimens than for the 80 mm specimens, and much more closely approximated the values obtained from the extensometer.

The extensometer was placed in the middle of the specimen, so the fact that it records lower strain readings than the crosshead indicates that there is significant deformation near the top and bottom surfaces of the specimen. There are likely two causes to this. First, much of the initial difference may be attributed to the poor workability of the material which made it difficult to obtain flat and parallel loading faces to within tight tolerances. However, significant differences later in the loading regime demonstrate that there is more to the anomaly than simply picking up machining slop. The second cause is likely related to greater compliance existing near the ends of the material. This would make sense in that cut spheres have significantly less strength than intact spheres, and the ends of the material are where most cut spheres are located.

The yield stress of the material, as calculated by the traditional 0.002 offset of elastic modulus, is equal to 3.2 ± 0.6 MPa. Figure 20 shows that there is substantial variation in the stress-strain response of the material at strains lower than roughly 0.02, but that at strains greater than 0.02 the variability decreases. The 0.002 offset yield stress captures this early variability, but in designing steel foam applications in which moderate to large deformations are

to be expected, the 0.002 offset stress exaggerates the practical variability of the material properties.

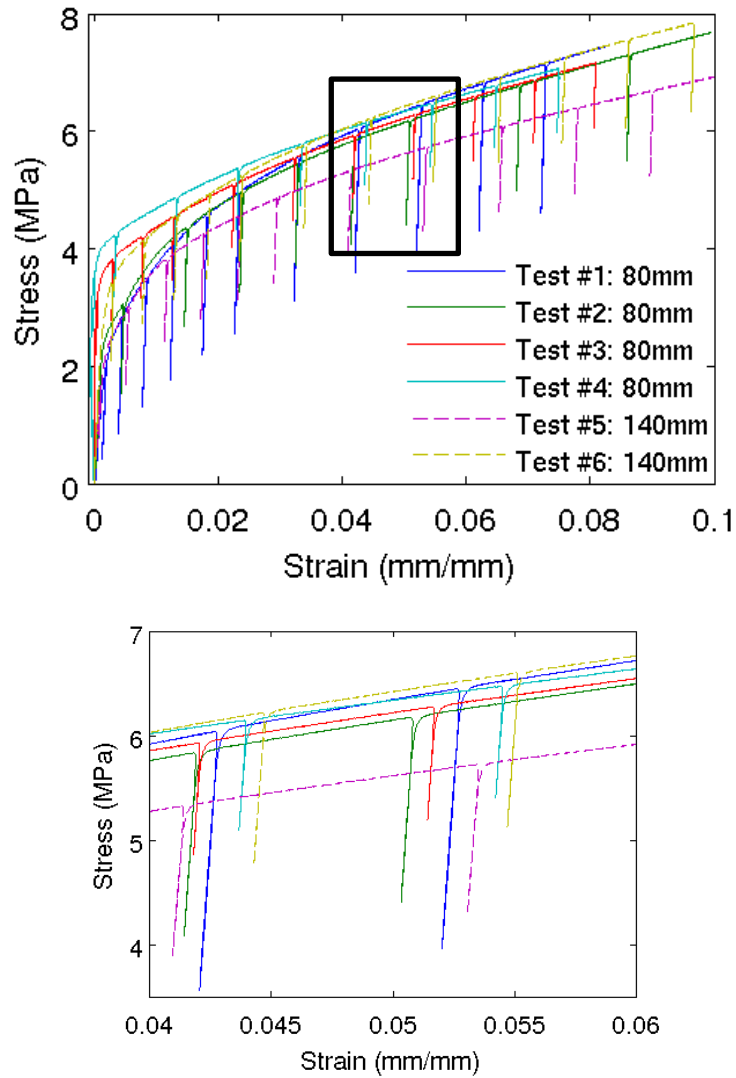


Figure 20: Stress-strain curve of multiple unloadings test showing the full testing regime (top), where the overlaid black box is the region for which a zoomed view is shown below.

The ISO/DIS 13314 metal foams compression testing standard provides an alternate method of calculating a yield stress in a “0.01 proof stress.” This 0.01 proof stress is defined simply as the stress value at an applied strain of 0.01, with no offset made for the elastic modulus. The 0.01 proof stress is equal to 4.0 ± 0.3 MPa, reflecting the much lower variability in stress magnitude at this higher strain. The choice of yield stress is a particularly important consideration when developing a bi- or tri-linear material model, for which the use of $\sigma_{p,0.02} = 4.0 \pm 0.3$ MPa is likely a better choice than $\sigma_{y,0.002} = 3.2 \pm 0.6$ MPa, being more reflective of the actual material behavior.

The elastic modulus was estimated by manually performing a least square linear regression on each of the unloading episodes shown in Figure 20. The resulting moduli are plotted against the strain at which the unloading began in Figure 21. The results show a large amount of uncertainty early in the loading history, but become relatively constant after an applied strain of $\varepsilon_y = 0.02$. After this point, the elastic modulus becomes 3150 ± 250 MPa. The test results show no strong evidence for evolution of the elastic modulus during deformation, though tests were only run until an applied strain of 0.1 (equal to the maximum reach of the available extensometer), indicating that although the material is well past yield at that point, no substantial damage has yet accumulated at the microstructural level. The highly variable moduli measured prior to $\varepsilon_y = 0.02$ are likely due to initial imperfections in the test specimens, such as surfaces which are not precisely parallel, and should not be regarded as characteristics of the material.

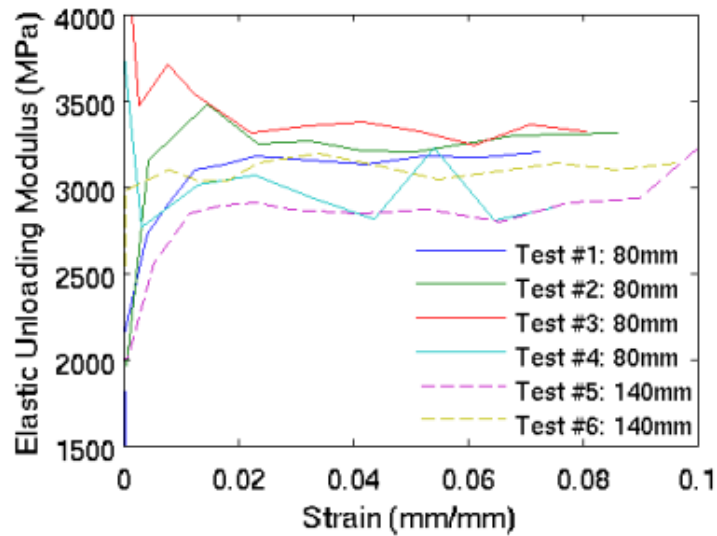


Figure 21: Elastic unloading modulus as calculated manually from each unloading shown in the stress-strain curves of Figure 20.

These tests were performed primarily using the extensometer for strain data. While this is significantly more accurate than using the crosshead, particularly either early in the loading regime or during movement through high-stiffness regions as shown above, other types of tests went far beyond the maximum reach of the available extensometers. Therefore, they are based upon crosshead strain. To validate that the crosshead does provide good enough results after picking up initial slop and in the absence of unloadings, one straight test was performed of a 52mm x 55mm x 80mm specimen, resulting in the stress-strain curve shown in Figure 22. It can be seen that, once the material passes into inelastic deformation, the crosshead results are exactly parallel to the extensometer, and effectively imprecise by a strain of about 0.04. Therefore, the crosshead provides results of sufficient accuracy to trust results gained after a strain of roughly 0.05.

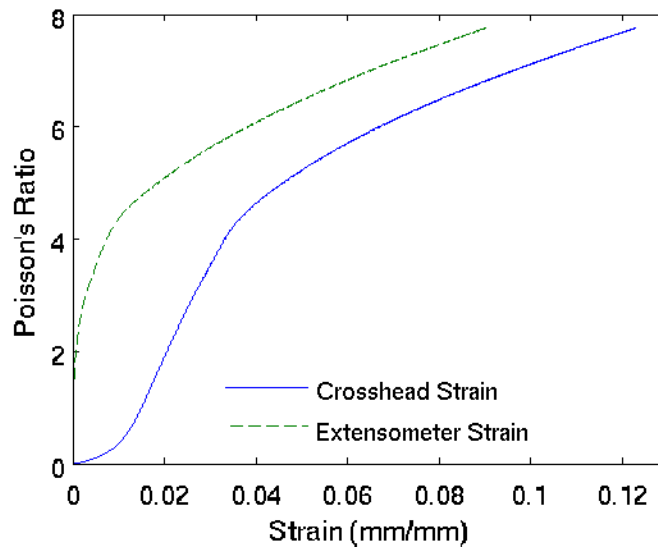


Figure 22: Validation for the accuracy of crosshead-based stress-strain curves, demonstrating fair accuracy after a strain of about 0.05.

Densification Strain Tests

Three replications of the densification compression test were performed, resulting in the stress-strain curves shown in Figure 23. A sequence of photographs showing the progression of densification is shown in the same figure. Note that all strain values for this test are based upon measurements taken from the crosshead displacement of the Instron. Manual measurements and comparison with extensometer-acquired strain data collected in other tests indicates that the strain readings, while not accurate enough to estimate the initial elastic modulus, do provide accurate measurements as the strains become larger than 0.05.

During the tests, the material was observed to form into an S-curve or C-curve shape, beginning at a longitudinal strain of approximately 30%. While this anomaly is similar to buckling in visual appearance, its commencement at such high strains suggests that it is caused by locally higher strains in the material. The term “asymmetric smooching” is used to describe this behavior in this thesis, and an image of a sample having undergone this asymmetric smooching is shown in Figure 25, and is also noticeable in most stages of Figure 23.

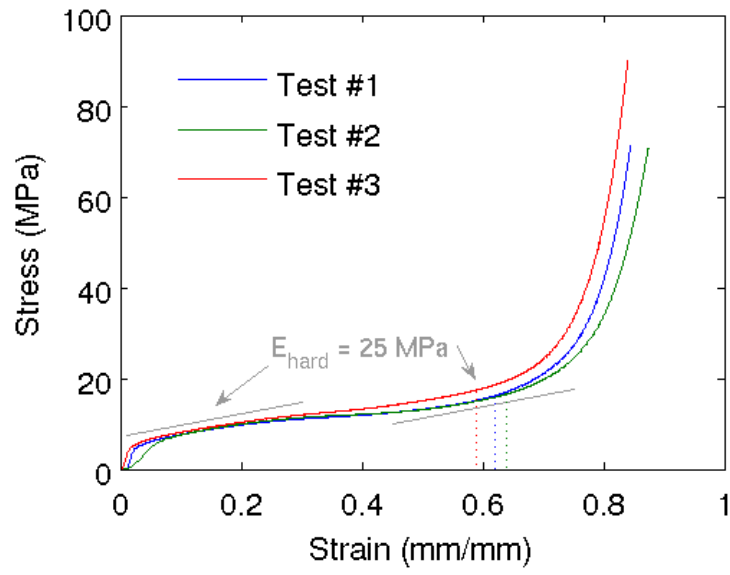


Figure 23: Engineering stress-strain curve from densification tests.

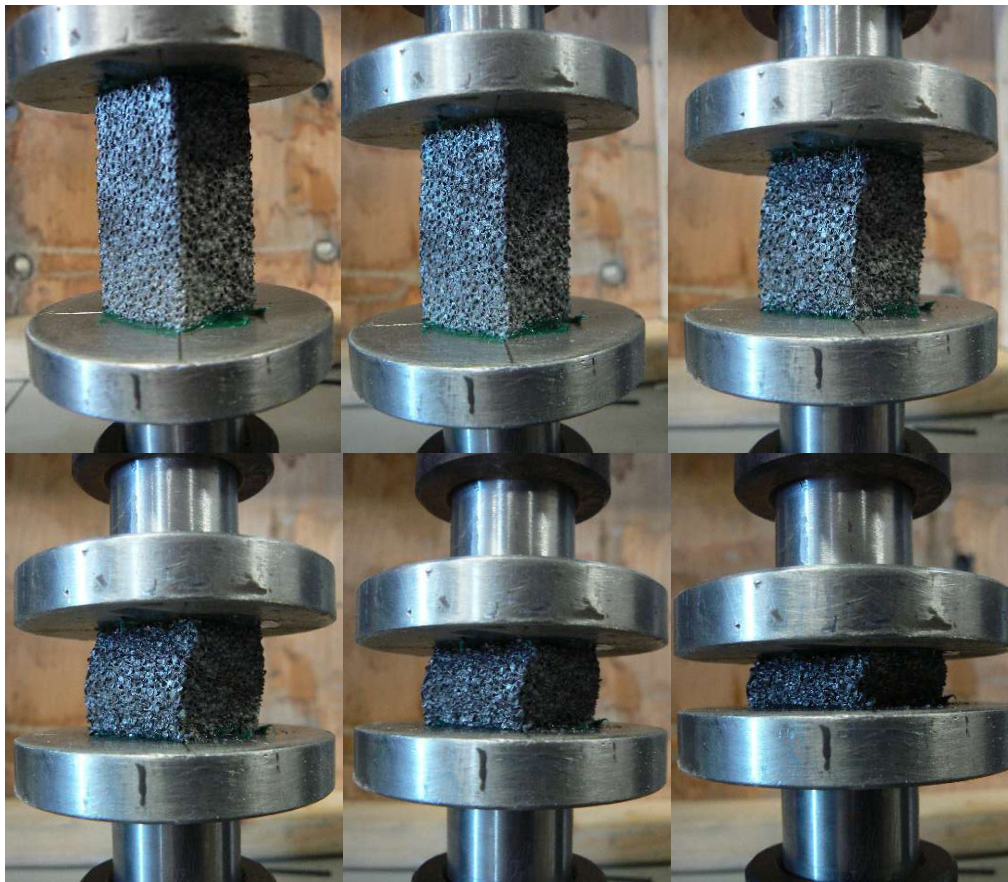


Figure 24: A sequence of images of the steel foam during the test at various strains (from left to right then top to bottom: 0.0, 0.10, 0.35, 0.50, 0.65, 0.85). Note that photos use a wide-angle lens; the platens did not rotate during compression.

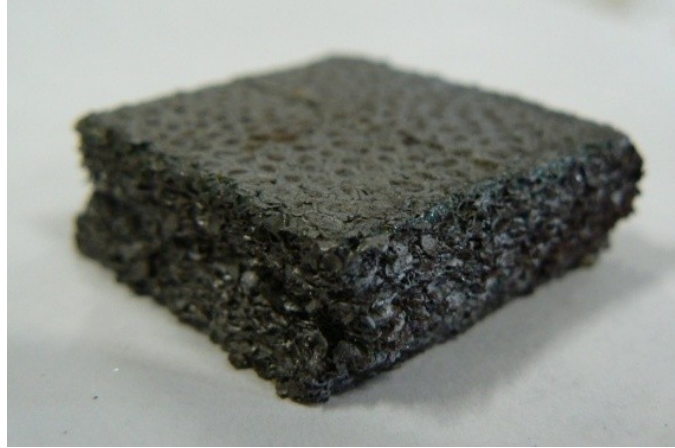


Figure 25: A densified sample which experienced asymmetric smushing.

Densification begins at a strain of approximately 0.65. No established definition exists for the onset of densification, so the following has been adopted: Let $E(\varepsilon)$ be the tangent modulus of the material determined by performing a linear regression on the stress strain curve over the range $[\varepsilon, \varepsilon+0.005)$, and define $E_{hard}(\varepsilon=0.01)$ to be the value of this tangent modulus in the window immediately following the 0.01 proof stress (essentially a yield stress, but taken as the stress at a strain of exactly 0.01, and not offset by the elastic modulus). The densification strain is then defined as the following:

Equation 1

$$\varepsilon_d = \min \varepsilon: E \varepsilon > E_{hard}(\varepsilon = 0.01)$$

In other words, densification is assumed to begin when the tangent modulus exceeds for the first time the post-yield tangent modulus. This definition gives an average densification strain for the three samples of $\varepsilon_d = 0.65$ with a range of ± 0.05 .

The tests also revealed that the material exhibits a substantial hardening modulus between the yield and densification points of approximately 20-25 MPa. The presence of such a hardening modulus should give pause to analysts who prefer to use an elastic-perfectly plastic material model. The hardening modulus is variable, but if measured as a secant line from the yield point to the densification point, it is equal to 21 MPa with a range of ± 1 MPa. Despite the

small value of the hardening modulus, the large strains that can be absorbed by the material mean that the stress level increases by a factor of two between yield and densification, a feature that a perfectly plastic model would of course fail to capture.

Poisson's Ratio Tests

Three replications of the Poisson's ratio compression test were performed and used to evaluate the evolution of the Poisson's ratio with applied compressive strain. As these tests used the crosshead for longitudinal strain data, their results were not used for anything other than Poisson's ratio calculations. However, the crosshead was assumed to be accurate enough for these measurements. An image of such a test in progress is shown in Figure 26.

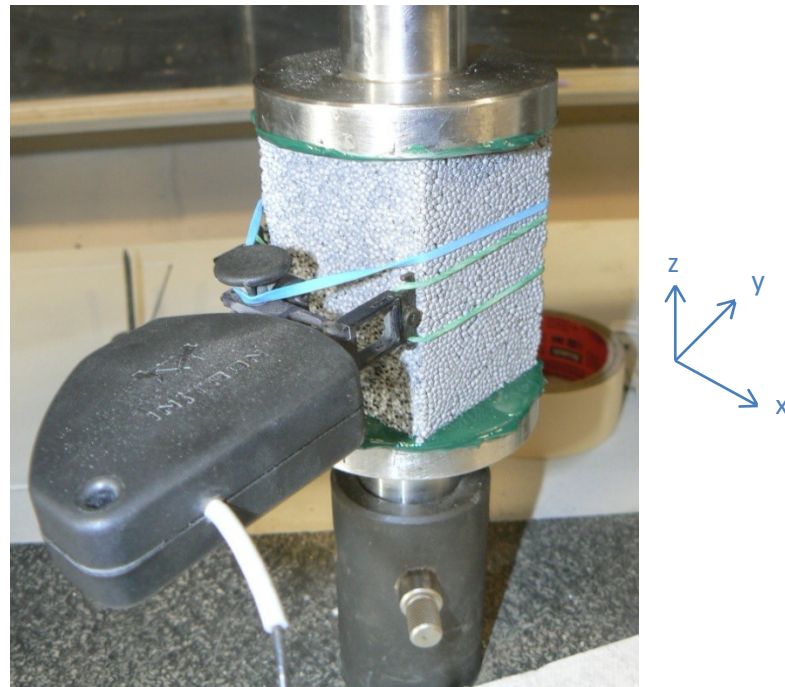


Figure 26: Image of Poisson's ratio compressive test in progress. The extensometer blades are held against the material by pressure

To calculate the evolving value of the Poisson's ratio, the assumption was made that the two transverse components of the strain (ϵ_x and ϵ_y) are equal. The average Poisson's ratio was then calculated over 0.005 increments of applied strain ϵ_z . By this definition, the Poisson's ratio

is given as a function of position by the following, where $\varepsilon_x(\varepsilon_z)$ represents the value of the transverse strain ε_x evaluated at applied strain ε_z :

Equation 2

$$\nu_{\varepsilon_z} = \frac{\varepsilon_x(\varepsilon_z) + 0.005}{0.005}$$

Figure 27 shows the complicated evolution of Poisson's ratio with increasing applied strain, with a fairly rapid increase from near zero to a peak value at an applied strain of approximately 0.4, which falls in the middle of the post-yield plateau shown in Figure 23: . This peak is followed by a gradual decrease until the end of our test at the onset of densification. The test was terminated at the onset of densification because this is where the Instron testing machine reached its maximum capacity.

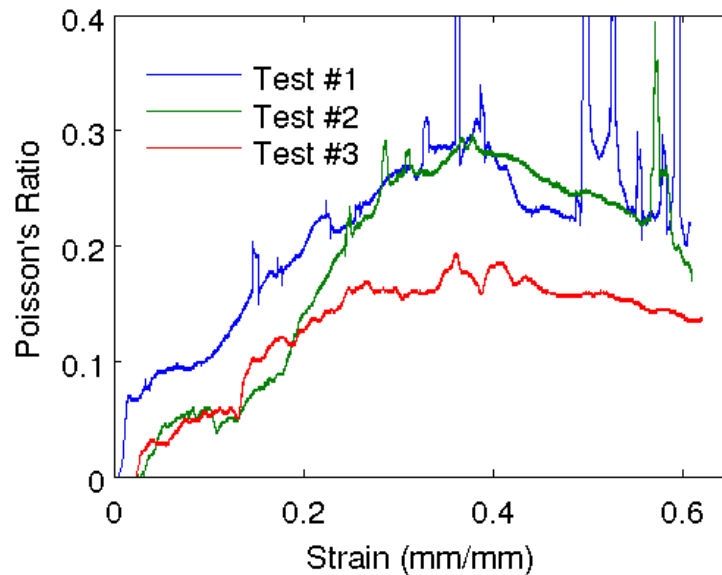


Figure 27: Engineering Poisson's ratio versus crosshead strain.

An important observation resulting from these tests is that the Poisson's ratio of 0.32-0.34 which is derived based on elementary mechanics of cellular networks may not apply for all foams (Ashby, et al. 2000). In the case of the HS foam tested here, the peak value of Poisson's ratio is in the mechanistically derived range, but over almost all of the range tested, the HS foam exhibits a Poisson's ratio much lower than 0.3. This finding will have significant meaning for the

behavior of HS steel foam under multiaxial stress states and even under uniaxial loading where the level of confinement in the interior of the specimen would be much lower than predicted by the Gibson and Ashby Poisson's ratio values.

During the tests, some small fragments of the material, sized on the order of approximately 0.5mm to 4mm were observed to fall off onto the lower platen. Also, the Poisson's expansion resulted in the corners of the samples just starting to extend over the edge of the platens when the machine cut off. However, it is believed that neither of these anomalies resulted in major discrepancies in the results.

Miscellaneous

One further non-standard test was performed in order to evaluate the strength of the base metal used in the hollow spheres foam. Theoretically, at some point deep into densification, the material would become dense enough so that it would effectively become a solid metal, and then experience another yield point characteristic of the solid metal. In this procedure, a sample that had already been crushed to the Instron 3369's machine capacity in the densification tests (described above) was cut down to a smaller cross-section and further compressed. After crushing to the Instron's capacity once, the resulting stress-strain curve still showed no sign of the base metal itself having yielded and reached its ultimate strength, so the cross-section of the sample was cut down again. This process was repeated a third time, when finally a base metal yield point was observed at approximately 260 MPa (equivalent to roughly A36 steel), showing that this was the ultimate strength of the material. An image of the three stages of specimens used in this testing are shown in Figure 28.

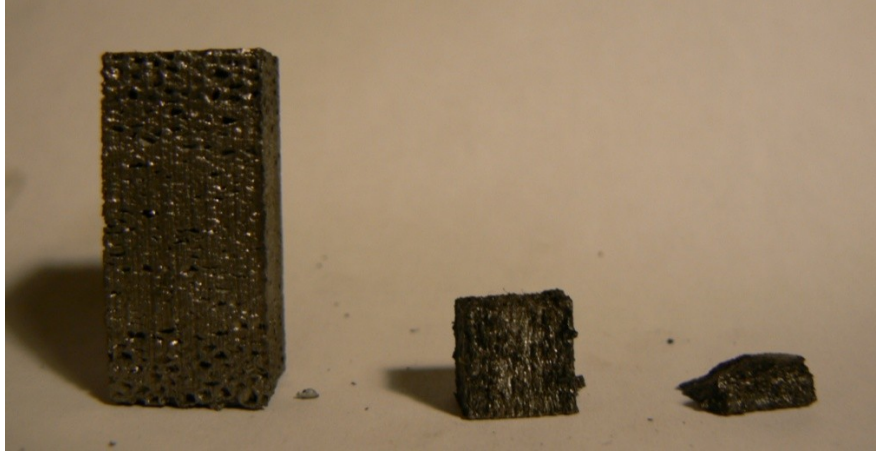


Figure 28: The three stages of specimens used to test the base metal yield strength of the hollow spheres foam.

Table 14: Summary of all compressive hollow spheres properties.

	Initial Modulus (MPa)	Inelastic Unloading Modulus (MPa)	Yield Stress (MPa)	Hardening Modulus (MPa)	Densification Strain (mm/mm)	Densification Stress (MPa)
Average	1900	3150	3.6	21	0.65	16
Range	±600	±100	±0.4	±1	±0.05	±1

	Ultimate Stress (MPa)	Elastic Poisson's Ratio	Poisson's Ratio @ 50% Strain
Average	260	-0.03	0.2
Range		±0.03	±0.04

3.3.2.2 PCM Foam

Due to limited quantities of material available, only one type of compression test, equivalent to the densification-type test performed upon hollow spheres specimens, was performed for multiple PCM foam samples. However, two sets of these tests were performed; one with the pores oriented longitudinally, and one with the pores oriented transversely. Resultant stress-strain curves are shown in Figure 30. All tests were performed upon an Instron 3369 testing machine (50 kilonewton capacity), having cross-sections of approximately 9mm x 9mm, except for test #4 in the longitudinal orientation, which was performed upon a Tinius Olson testing machine (1750 kilonewton capacity) with a 25mm x 25mm cross-section. Note

that, because the material was so short in longitudinal height, the extensometer could not be used, and strain values are therefore based upon crosshead displacement and only approximate. In particular, the extremely high stiffness of the material, witnessed in a later test, is not reflected in these plots (see the end of this section where an elastic modulus test is described).

Compression specimens failed in a diagonal brittle fracture at a strain of roughly 0.15 and stress of roughly 500 MPa. Test #4 in the longitudinal orientation and tests #2 and #3 in the transverse orientation reached this ultimate capacity, as shown in Figure 30. The other tests were terminated upon reaching the capacity of the testing machine before ultimate material capacity was reached. The dimensions were kept within tolerances of about 5%, so the slight differences in cross-sections may explain why some specimens reached ultimate and others did not. Images of two specimens which failed in such a brittle manner are shown in Figure 29.

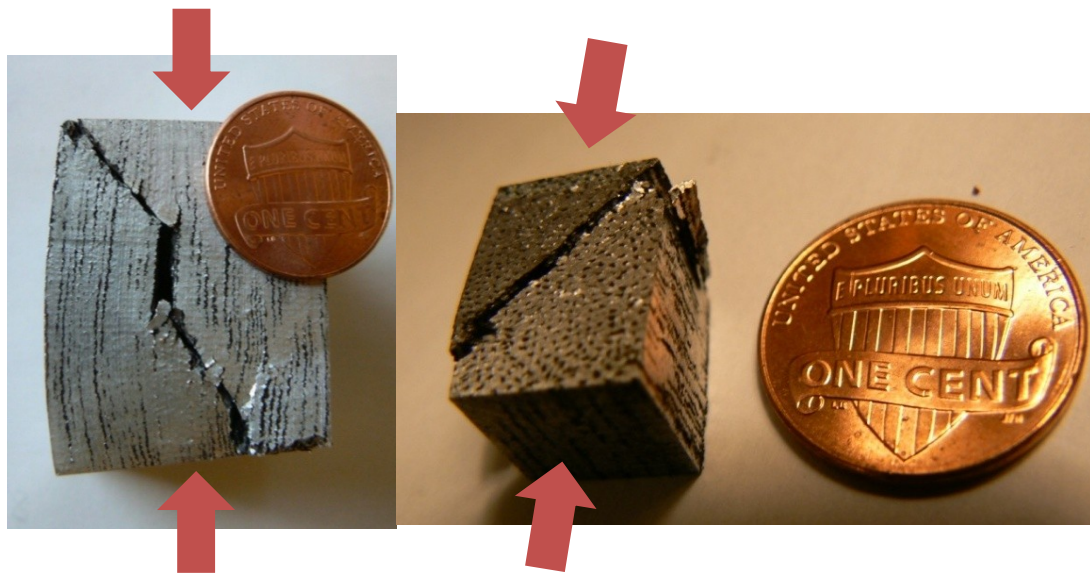


Figure 29: Images of two PCM compression specimens which failed in brittle fractures: longitudinal orientation test #4, performed upon the Tinius Olson testing machine (left), and transverse orientation test #2, performed upon the Instron 3369 testing machine (right). Block arrows indicate the direction in which load was applied.

No difference was observed in ultimate capacity between longitudinal and transversely oriented specimens, though only one longitudinal specimen reached ultimate capacity. However, the average yield stress of the longitudinal specimens was approximately 15% higher, at 409 ± 10 MPa, than that of the transverse specimens, which measured 349 ± 50 MPa. The traditional 0.2% offset definition of yield stress was used for these results.

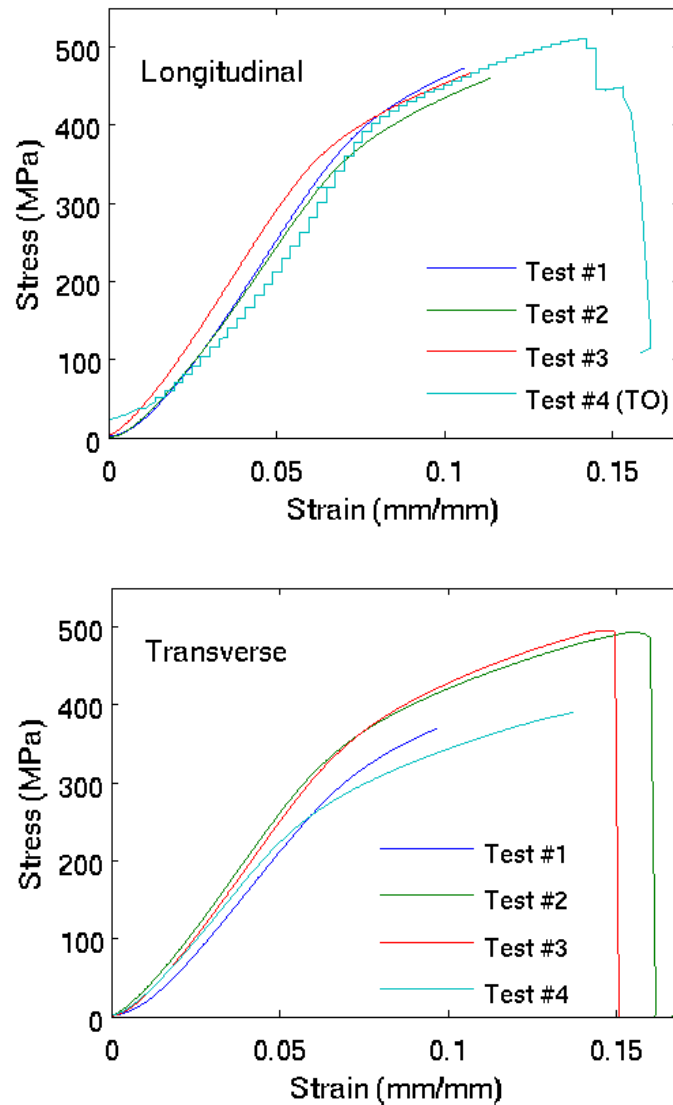


Figure 30: Uniaxial compression stress-strain curves with pores oriented longitudinally (left) and transversely (right) to the direction of loading. All tests were performed on an Instron 3369 machine, except test #4 in the longitudinal direction was performed on a Tinius Olson.

One further test was performed upon a specimen having dimensions of 37.4mm by 43.8mm by 108.6mm; that is, the entire block of material remaining after all of the above compression tests and the tension tests described in section 3.3.3.2 PCM Foam were performed. The pores were oriented transversely. This specimen was large enough to attach the extensometer onto and was tested only out to a strain of 0.01, or just enough to obtain a reliable elastic modulus. From this test (not shown in the graphs), an elastic modulus value of 59,000 MPa was obtained, suggesting an extremely stiff material and one in which the elastic modulus had scaled almost linearly (34% of 200,000 MPa is 68,000 MPa). Note that this is roughly 10 times stiffer than the graphs of Figure 30 suggest, though those tests used the crosshead displacement for their strain values, while this test used the extensometer. A table summarizing all compressive properties of the PCM foam is shown as Table 15.

Table 15: Summary of all compressive properties of PCM foam.

	Transverse Initial Modulus (MPa)	Longitudinal Yield Stress (MPa)	Transverse Yield Stress (MPa)	Ultimate Strain (mm/mm)	Ultimate Stress (MPa)
Average	59000	409	349	0.15	505
Range	n/a	±10	±50	±0.01	±5

3.3.3 Tension Testing

Tension tests were performed upon both hollow spheres and PCM foams in order to determine elastic moduli, yield stresses, and ultimate stresses and strains. Though the dimensions differed between the two materials, the procedures were essentially the same. The only difference in resulting data is that the PCM foams were too small to attach and extensometer to.

3.3.3.1 Hollow Spheres Foam

Three replications of a uniaxial tension test were conducted to evaluate the behavior of the hollow spheres foam in tension, even the qualitative properties of which have not been reported previously. An image of a test in progress is shown in Figure 31.

The results, summarized in the stress-strain curves of Figure 32, indicate poor tensile ductility for this material, with fracture strains 0.019 ± 0.007 and a high level of uncertainty associated with even that small fracture strain. The peak tensile stresses of 4.9 ± 0.9 MPa are also highly variable, although the strength in tension is comparable to the stress level in compression at equal strain levels. In a fourth test (not shown in the graph), several periods of unloading were included to evaluate the material elastic modulus in tension. No significant difference was found between the compressive and tensile moduli, which were both approximately equal to 3150 MPa. Full results are summarized in Table 16.

In tests #1 and #3, two dominant cracks formed originating from opposite sides of the specimen, while in the other test, a single dominant crack formed. In tests #2 and #3, the dominant crack(s) formed well away from the transition from the grip to test sections, suggesting that the specimen design, despite its small deviations from the ASTM E8 testing standard, is appropriate for characterizing the tensile material properties of this hollow spheres steel foam.



Figure 31: Image of a hollow spheres tension test in progress.

The shape of the stress strain curve in all three tests was similar up to the point of peak stress, the point at which a dominant crack becomes manifest in the specimen. In all three cases, some ductility is shown, as a distinct yield point and a small amount of inelastic deformation were observed. The nearly immediate drop to zero stress level in test #3 was recorded because the dominant crack appeared at the location of one of the extensometer blades, meaning that additional strain ceased to be recorded. The crosshead-based stress-strain curves, which are not shown, indicate that the post-peak behavior was similar for all three tests.

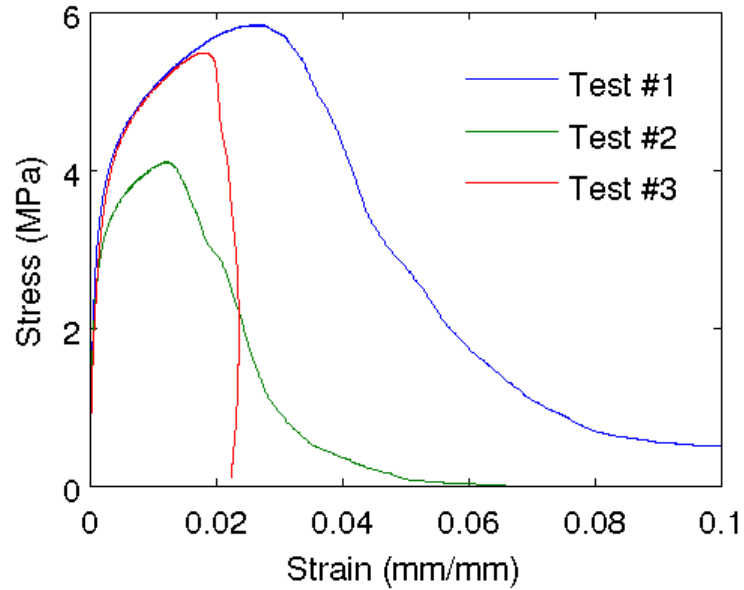


Figure 32: Stress-strain curves for the three tension tests performed (top), with corresponding photos of failed specimens (below, tests #1 through #3 pictured from left to right).

Macro imagery of the fracture surfaces (see Figure 33) revealed that fracture occurred by failure of the individual hollow spheres along the circumference of the weld. This indicates that the connections between spheres, where the material thickens substantially, are stronger than the hollow sphere shells themselves, and indicates that if greater tensile strength—and possibly greater ductility—is desired from the material, thicker spheres or possibly larger diameter welds should be used. If the diameter of the spheres were increased, this change could be made without affecting the overall relative density of the material.



Figure 33: Macro photo of tensile fracture surface. Arrows indicate examples of spheres from which welds have pulled out.

Table 16: Summary of all hollow spheres tensile properties.

	Unloading Modulus (MPa)	Yield Stress (MPa)	Ultimate Strain (mm/mm)	Ultimate Stress (MPa)
Average	3150	3.7	0.019	4.9
Range	n/a	±0.4	±0.007	±0.9

3.3.3.2 PCM Foam

Tension tests for PCM materials were significantly more consistent than those observed in hollow spheres tests. Two tests each were performed with the pores oriented longitudinally and transversely to the direction of loading. An image of a test that had just completed is shown in Figure 34. The PCM specimens were too small to attach an extensometer to, so strain values shown are measured by the crosshead and therefore imprecise.

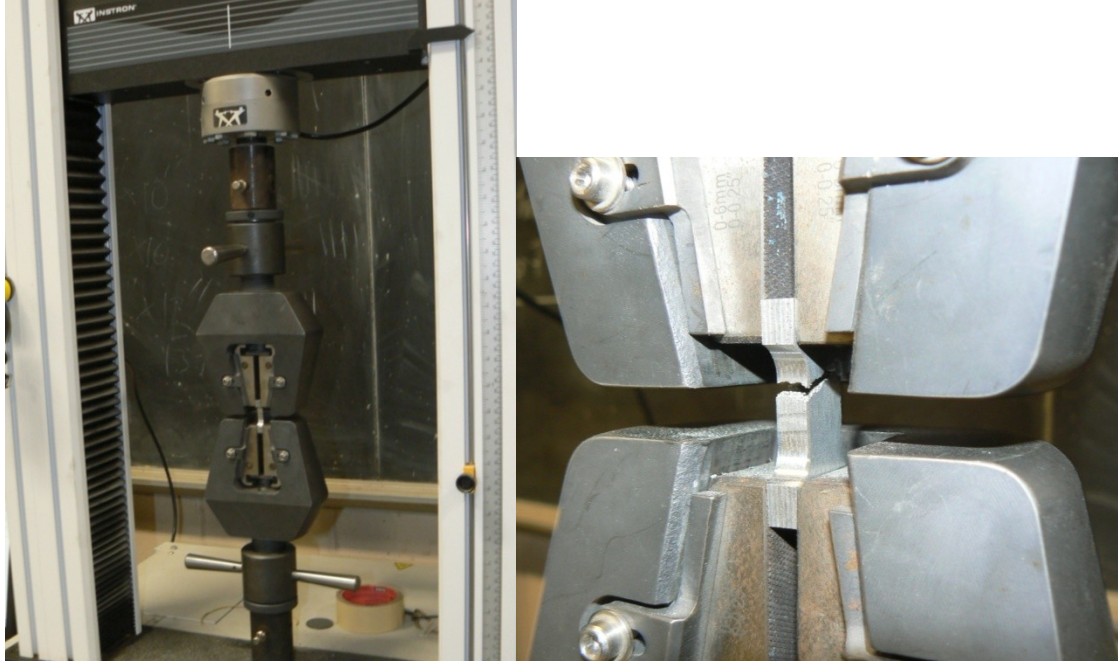


Figure 34: Image of PCM tension test that had just completed, showing the full test setup on the left and a zoomed image of the grips and specimen on the right.

Unlike the hollow spheres foam, the tensile strength of the PCM foam was observed to be nearly two to three times lower than its compressive yield strength. The strength, however, was significantly higher. Furthermore, the ultimate strength of the transverse orientation was roughly 40% weaker than the longitudinal direction. In comparison, PCM compression tests showed only about a 10% difference in strength between longitudinal and transverse orientations. The cause of the initial dip in the stress-strain curves (see Figure 35) is likely due to the wedge grips seating upon the specimen and providing additional strain irrelevant to the material. Evidence of this may be seen in the minor damage to the grip surface of the specimens shown near the ends of the specimen photos of Figure 36. Despite the use of a smooth fillet, failures were predominantly located at the fillet, suggesting that results shown here may be conservative. Full results are summarized in Table 17.

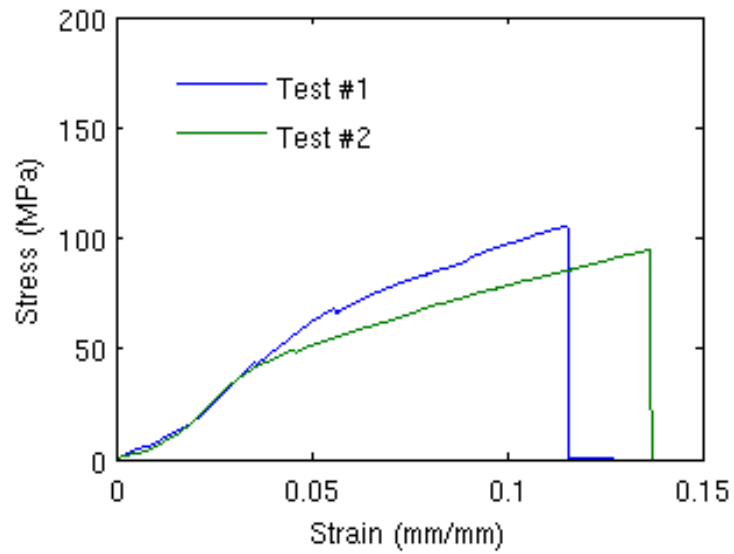
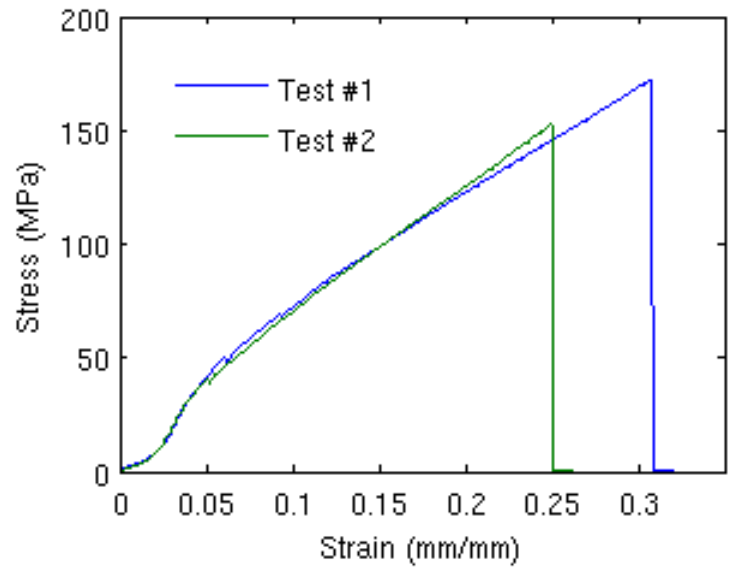


Figure 35: Stress-strain curves for PCM tension tests, with pores oriented longitudinally (top) and transversely (bottom) to the direction of loading.

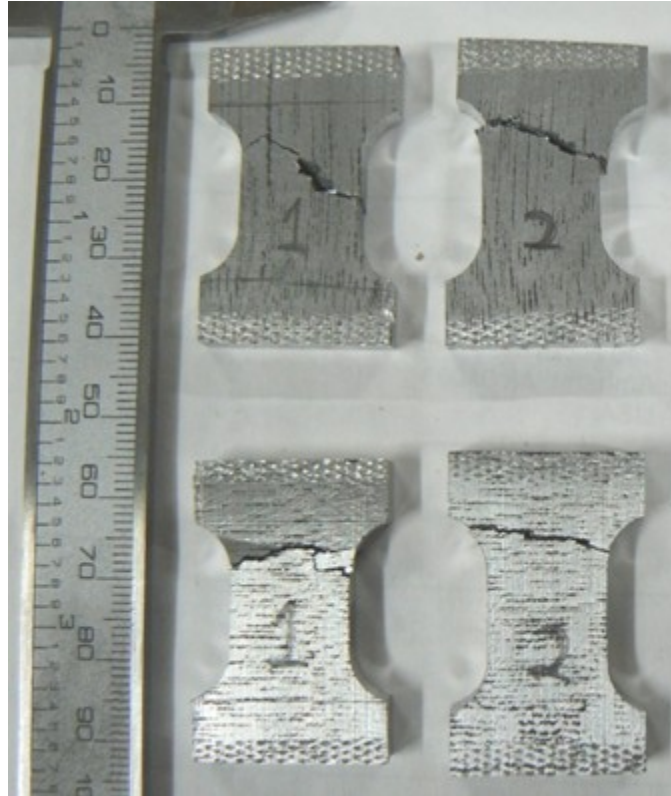


Figure 36: Photos of failed PCM tension specimens, with pores oriented longitudinally (top row) and transversely (bottom row) to the direction of loading.

Table 17: Summary of all PCM tensile properties.

	Longitudinal Ultimate Stress (MPa)	Transverse Ultimate Stress (MPa)
Average	162	100
Range	±10	±5

3.3.4 Shear Testing

Once a successful method of performing shear tests was found, three such tests were repeated upon hollow spheres foams. An image of the full test setup is shown in Figure 37. Strains shown and discussed in this section are shear strains, so that a strain of 1.0 refers to a displacement equal in magnitude to the thickness of the material between the platens.



Figure 37: An image of the full shear test setup, ready to begin load application.

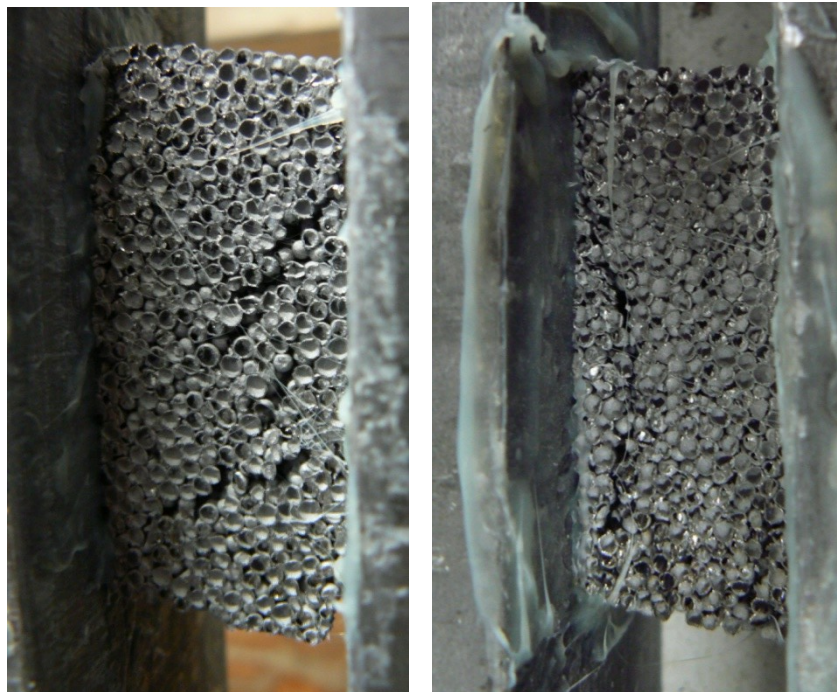


Figure 38: Image of shear specimens #1 (left) and #2 (right) at about 0.08 strain, clearly showing shear cracks.

Tests showed remarkable consistency, with elastic modulus and ultimate stress varying by less than $\pm 10\%$ (see Figure 39 and Table 18). Some ductility is evident in that the material definitely yields before it reaches its ultimate strength. There are also two distinct slopes evident in the post-yield behavior. The second, smaller slope beginning at about 0.07 shear strain is likely where friction between the heterogeneous fracture surfaces begins. Test #3 does show somewhat sudden dip at a strain of 0.07; this is believed to be where a small (less than 10 mm²) region of the specimen delaminated from the platen. This was the only test in which any delamination occurred, and it exhibited a higher ultimate stress than other tests, so its data was kept.

A measurement was taken on test #3 of the separation between platens, in order to verify that stresses were as purely shear as possible without rotation. The measurement was taken at the top of the platens. The separation was measured to be approximately 0.1mm just after the ultimate strain was passed, and eventually reached 1mm at 0.11 strain. At ultimate, the shear strain was about 0.03, equivalent to about 1.5mm of displacement, suggesting approximately a 7% rotation.

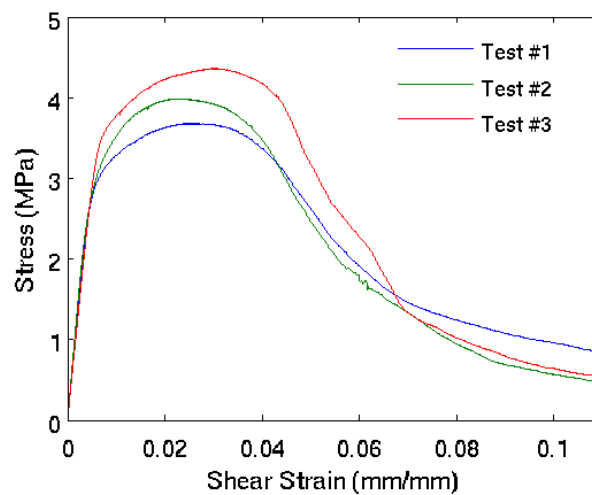


Figure 39: Stress vs shear strain graph for hollow spheres shear tests.

Table 18: Summary of hollow spheres shear properties.

	Shear Modulus (MPa)	Yield Stress (MPa)	Yield Shear Strain (mm/mm)	Ultimate Stress (MPa)	Ultimate Shear Strain (mm/mm)
Average	648	3.3	0.007	4.0	0.026
Range	±40	±0.3	±0.001	±0.4	±0.004

3.3.5 Discussion of Results

Gibson and Ashby (Ashby, et al. 2000) developed mathematical models for predicting the effective properties of metal foams. Comparing all of their available “open-cell” equations to experimental results, the hollow spheres results are within the very large predicted possible range with the exception of Poisson’s ratio, which is predicted to be between 0.32 and 0.34 (Ashby, et al. 2000), differing substantially from these results, which showed a Poisson’s ratio varying from 0 to about 0.25 depending upon compressive strain.

Tension and compression of hollow spheres foams feature different yielding and failure modes, with the compressive strength depending upon wall buckling, and the tensile strength depending upon weld size and quality as well as sphere shell tension. It is believed to be a coincidence that the compressive and tensile yield strengths are actually almost the same (averaging 3.4 or 3.7 MPa, respectively). Due to compression required during the manufacturing process to sinter the hollow spheres material, the spheres themselves have significant deformities, as can be seen in the microstructural images of Figure 40. These deformities encourage buckling of the spheres and are a microstructural instability.

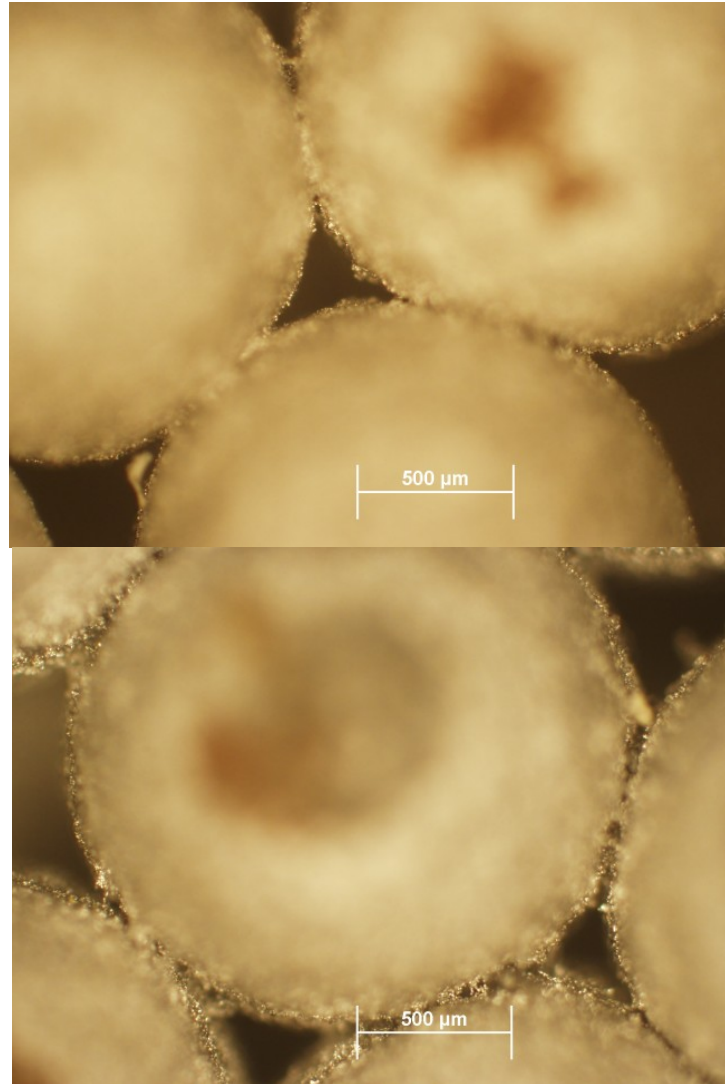


Figure 40: Two microstructural photos of hollow spheres showing the amount by which spheres are deformed around weld regions, resulting in instability in the spheres walls.

The PCM material has proven to be significantly more brittle than the hollow spheres foam, showing very little strain between compressive yield and ultimate failure. While precise strains were not determinable, they were less than 15% in both tension and compression. Compressive yield strains were on the order of 0.001, and no yield point was observed in tension. The brittleness arises from the sintering process during manufacturing. The ability to mill the PCM material led to smooth surfaces and few macroscopic crack initiators, but cracks

began at the pores instead, as was particularly visually apparent in tests where pores were oriented transversely.

For PCM foams, the orientation of the pores made a greater difference in tension than in compression. Tensile ultimate stresses differed by approximately 40%, while ultimate stresses were nearly identical and yield stresses only differed by 10% in compression. As expected, orientations longitudinal to the direction of loading are stronger than those in the transverse.

Key Section Findings

Hollow spheres foams showed very similar yield strengths in compression, tension, and shear, at 3.3-4.0 MPa, with low ductility in tension and very high ductility leading to densification in compression.

PCM foams showed extremely high strengths and stiffnesses compared to other steel foams, with compressive ultimate stresses up to 409 MPa, tensile ultimate stresses up to 162 MPa, and elastic moduli on the order of 60,000 MPa. Compression tests experienced brittle failures, while tensile tests showed much lower ultimate stresses.

CHAPTER 4 COMPUTATIONAL SIMULATIONS WITH RANDOM MICROSTRUCTURES

4.1 Introduction and Motivation

Key Section Objectives

Describe the reasons for designing and performing new types of computational simulations for metal foams.

There are several possible microstructures for metal foams, though closed-cell foams present the most promise for structural applications due to their higher strength and stiffness properties. The most prominent of the closed-cell manufacturing methods include gasar / lotus-type, powder metallurgy, sintered hollow spheres, and composite hollow spheres. Each method results in different microstructures, some of which may be anisotropic, have different deformation mechanisms, or different stress concentrators. Existing mathematical models have generally tried to describe the macroscopic material properties of all metal foams by the same single input parameter: the relative density (equal to the density of the foam divided by the density of the solid metal) (Ashby et al 2000). Microstructural differences along with the various published experimental tests, however, suggest that the behavior is more complex than these models describe.

Thus far, attempts to perform finite element analyses of metal foams have focused almost exclusively upon sintered hollow spheres foams, simplified to assume a regular stacking pattern such as face-centered cubic or body-centered cubic, and then simulations are performed with unit cells (Sanders and Gibson 2002) (Gao, Yu and Karagiozova 2007). To more accurately simulate metal foams, the microstructures should be modeled as the random structure that they are, and also microstructures characteristic of other manufacturing methods should be simulated. Finite element simulations allow for an understanding of how best to

optimize a foam's microstructure to achieve desired macroscopic properties. Later, foams with such optimized structures could be tested experimentally to verify computational predictions.

The generation of such random models, as well as their solution, post-processing, and three parametric studies using these models are described in this chapter. Using a combination of MatLab and the ADINA FEA program, two parametric studies have been performed to investigate the behavior of gasar and hollow spheres metal foams. The influence that specific microstructural parameters have upon the macroscopic material properties is investigated by examining the simulation results for the effective macroscopic stress-strain curve, yield stress, elastic and plastic Poisson's Ratios, and percent of the material yielded.

Key Section Findings

Deficiencies in previous computational simulations, particularly in the failure to model randomness, are rectified in the new Metal Foams Simulator.

4.2 Computer Program

Key Section Objectives

Describe the user interface and basic method of function of the program that has been developed to simulate metal foams.

Explain the basic coding theory as to how the program operates internally.

To perform computational simulations, a program has been developed that will perform all steps of the analysis based upon simple user input. This section of the text will give only a summary of the technical details of this program code. The theory behind the code is explained separately in section 4.3 Finite Element Analysis. A complete user guide for the program is also contained in the Appendix.

4.2.1 Coding and User Interface

The program developed makes use of both the ADINA finite element package and MatLab. All code is contained within the MatLab script file `Metal_Foams_Simulator.m`. The coding theory is based upon instructing MatLab to write out a series of ADINA script files, then run ADINA in batch mode with these script files, and finally read in ADINA's output files and perform mathematical analysis on these outputs. All commands are fully automated so that once the script is executed, it is capable of running everything from initial geometry generation to results extraction without any further user input. All code is kept fully commented, with detailed descriptions which precede each function describing what the function does and roughly how it does so, as well as line comments for individual lines of code which are deemed particularly complex or difficult to follow.

Throughout execution, a series of three status bars is displayed, for preprocessing, solving, and then postprocessing, displaying the specific current task being performed and the progress to completion of each of three major portions of the code. The status bars also provide a "Cancel" button which, when pressed, cleanly aborts all processes, cleans up temporary files, and returns MatLab to its previous state. In addition, all ADINA output is redirected to the MatLab command window, so all steps that ADINA is performing may be observed by the user in real time. See Figure 41 for a sample screenshot of the program during execution.

The code contains significant error-trapping based upon the UNIX standard exit code mechanism. Within the code, the mechanism operates by means of setting and monitoring a global variable (or "application variable" in MatLab terminology) to track the exit code. The exit code starts off at a value of "0", and if no error is encountered, then that value remains unchanged and is eventually returned by the code to the MatLab command line, indicating a successful execution. A total of 15 error codes are possible from within the program, and any

error codes returned by externally-executed UNIX programs such as `scp` or `rm` are also passed on and returned. Internal error checks search for problem conditions such as improper parameters passed by the user, a freeze within the ADINA program, failure to read an expected data file, or a meshing error. All possible errors should be captured by this internal mechanism and will not result in a quick exit by the MatLab program.

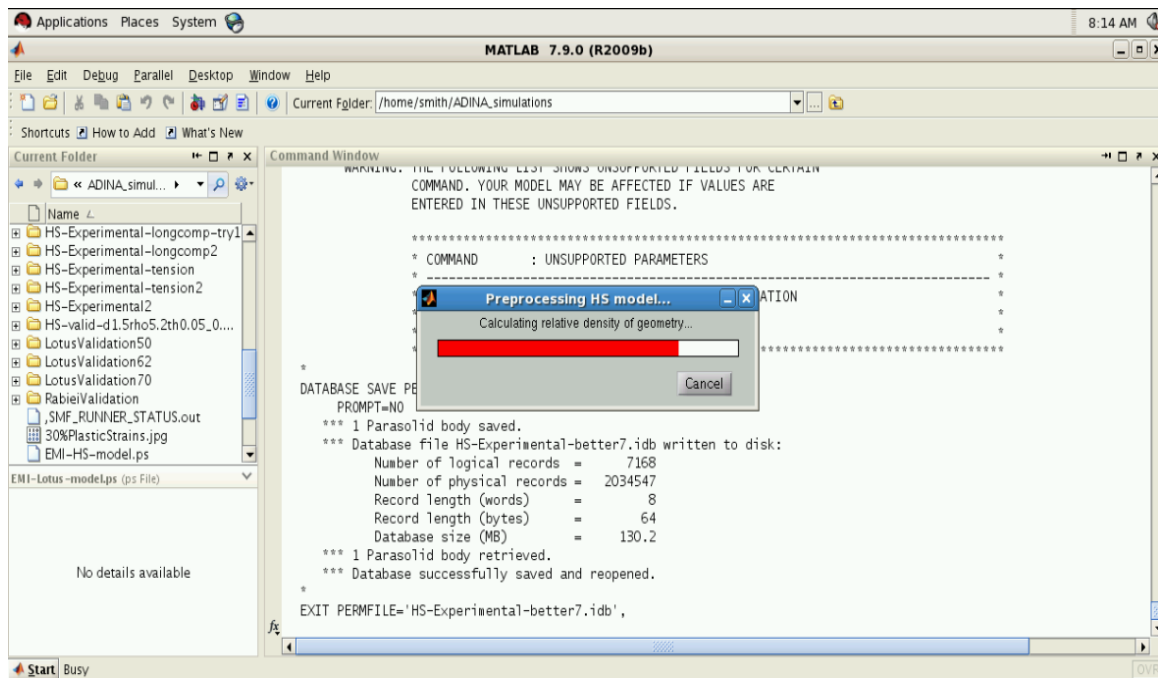


Figure 41: Sample screenshot of program during execution.

Either 35 parameters for general closed-cell simulations or 38 parameters for hollow spheres simulations are required to run the entire simulation. These parameters may be set either directly in the `Metal_Foams_Simulator.m` file, where the input variables are fully explained and commented, or passed to the script file as function parameters. The latter method allows for the possibility of a secondary script to drive the simulations. For example, this method of using a secondary script is used in running simulation test matrices, where the secondary script passes a set of all required parameters for one individual simulation, waits for it to complete with a successful exit code, and then passes the next set of required parameters for

the next individual simulation. Through these means, the program may be simply set up and then allowed to run everything without user intervention. Previous secondary scripts have also checked for a non-zero exit code, which would indicate that an error was encountered, and then attempt to re-run that same simulation with slightly modified parameters such as a more refined mesh in order to automatically attempt to correct common problems. If too many of these automatic retries failed, then the secondary script would give up, record the irrecoverable failure of that specific test into a log file, and then move on to the next test.

The capability of interfacing with a UNIX job queue, such as that commonly used on supercomputers, was also added to this code, though it was never used in practice due to technical difficulties with the solver itself on the available supercomputer. In this procedure, the code would do all preprocessing on the local computer, and then upload the data files to another machine and submit the ADINA solve job to the run queue. Once that job was complete, the user could re-execute the program and it would retrieve the results data from the other machine, and perform postprocessing operations on the local machine. In this way, the most computationally intensive portion of the program, the solving, may be exported to a more powerful machine.

The program finally returns results in the form of graphs saved in multiple formats as well as a MatLab workspace file, `[name]_results.mat`, which contains all output variables including all variables that were used for graphing. Further, a total of at least 6 log files, 4 ADINA input files, and 10 raw data files are generated throughout the course of program execution. In the end, a grand total of at least 46 files are generated by the program.

4.2.2 Code Segments

The code consists of three distinct segments, including preprocessing, solving, and postprocessing. Usually, these segments are all run in one execution, but they may be run independently if the user desires by setting the “run_part” input parameter to the desired segment or combination of segments. To facilitate this separation of segments, the code saves a MatLab workspace file entitled `[name]_internal.mat` at the end of each segment. This file records all variables necessary for the following segments to run properly, such as geometry settings or material properties. Functions within each segment are clearly distinguished by including one of four prefixes on each function name: “pre_”, “solve_”, “post_”, or “help_”. The last prefix distinguishes helper functions which are used by multiple segments of the code, such as one function that monitors an ADINA log file to check for errors or program freezes.

The preprocessing segment internally has three parts, each of which executes a separate ADINA script. The first is the geometry generation and meshing of the specimen, for which functions are unique to either hollow spheres or general closed-cell foam simulations. This part involves MatLab generating a valid geometry, and then writing an ADINA script to build and mesh that geometry and then output a NASTRAN file to describe the mesh. This NASTRAN file, which is a simple plaintext file, is then read and parsed by MatLab to extract the locational coordinates and ID numbers of mesh nodes. These ID numbers are necessary for load and boundary condition application as well as for various post-processing operations. Next, a simple ADINA script that does nothing other than calculates the total volume of the generated geometry is written and executed. This datum is later used to calculate the relative density of the simulated foam. Finally, an ADINA script is written and executed to apply loads and boundary conditions to lists of appropriate nodes, and the ADINA data file is prepared for solving.

During the solution segment, MatLab merely executes the ADINA solver and then monitors its output file for errors or freezes. The program performs no other operations during this time.

Finally, during the postprocessing segment, MatLab writes and executes an ADINA script for exporting sets of the results data into plaintext files, then reads and parses those plaintext files, and finally prepares results in a user-comprehensible format. Three text files are exported, one which contains a list of timesteps and the loading present at each step, another which contains nodal results data, and the last which contains elemental results data. To accommodate particularly large simulation runs, the opening of which may require more RAM than is present on the system, ADINA is set to only open a maximum of 20 timesteps at once. ADINA is executed multiple times and results data are concatenated together by MatLab if there are more than 20 timesteps in the simulation.

Parsing of the extremely large text files is accomplished with the assistance of the highly efficient UNIX 'sed' program, which then converts the text into a form that can be directly read by MatLab. These data imported from the text files include raw values such as nodal displacements, nodal reaction forces, and accumulated effective plastic strain of elements. MatLab then converts these data into stresses, strains, and other engineering values, and then uses these to calculate secondary results such as average transverse strains, an incremental Poisson's ratio, and percentage of elements yielded. Both engineering and true values for stress, strain, and Poisson's ratio are calculated, with true values of strain calculated by using the formula $\epsilon_{true} = \ln(1 + \epsilon_{eng})$ and true values of stress calculated by dividing the load values by the average instantaneous cross-sectional area of the material. Finally, several scalar values such as elastic modulus, yield stress, and elastic Poisson's ratio are calculated. Graphs generated include stress versus strain, modulus of stress versus strain, incremental Poisson's ratio, and

percentage of elements yielded versus strain. All graphs are generated based upon both engineering and true equivalents of the values, and are each generated in MatLab .fig, TIFF image .tif, and Encapsulated PostScript .eps formats.

Key Section Findings

The program developed takes between 35 and 38 input parameters and converts them into a total of 46 output files including several graphs and derived scalar values, all while providing the user with a detailed display of the program's current status towards completion.

Making use of ADINA, MatLab, and several efficient UNIX applications, the program computes a random geometry, solves, and then extracts and calculates common engineering graphs and values.

4.3 Finite Element Analysis

Key Section Objectives

Describe the geometry theory behind generation of both the hollow spheres and general closed-cell models.

Explain the engineering theory for meshing, solving, and finally converting raw results values to effective macroscopic mechanical properties.

The coding and user interface of a program are useless without a solid theory behind the program's operations. Throughout the `Metal_Foams_Simulator.m` program, extensive finite element analysis theory is employed, from the nature of the geometry generated, to how to post-process the raw results data.

4.3.1 Geometry Generation

Most manufacturing methods for closed-cell metal foams result in a microstructure that may be thought of as a bulk material with voids of some geometry scattered randomly throughout. Among the most notable exceptions to this are foams produced by the hollow spheres method, which are a random stacking of hollowed-out spheres connected together through small welds. Two different algorithms were therefore developed to generate the

geometries: one to represent the majority of closed-cell foams, and the other to represent hollow spheres foams specifically. Throughout this paper, the former algorithm is referred to as the “general closed-cell” geometry. The important constraints included that both algorithms had to be able to produce a geometry compatible with the ADINA FEA program and that a single simulation had to be possible to perform in MatLab within a period of at most several hours on a modern computer.

For both the hollow spheres and general closed-cell models, the remaining volumes of the geometries, within metal portions of the matrix, are assumed to consist exclusively of solid metal. This may not be entirely accurate, as most manufacturing methods result in at least some porosity in the bulk metal, but the assumption was considered an adequate and necessary approximation. As cellular metals made of steel are the focus of these simulations, an elastic-plastic bilinear model has been adopted. The elastic modulus used was 200000 MPa, scaled linearly by the estimated relative density of the microporosity within the material (ρ times E). The yield stress was obtained from material property tables if the base metal was known, or estimated through calibration if not. The plastic modulus was generally assumed to be 690 MPa.

4.3.1.1 Hollow Spheres Geometry

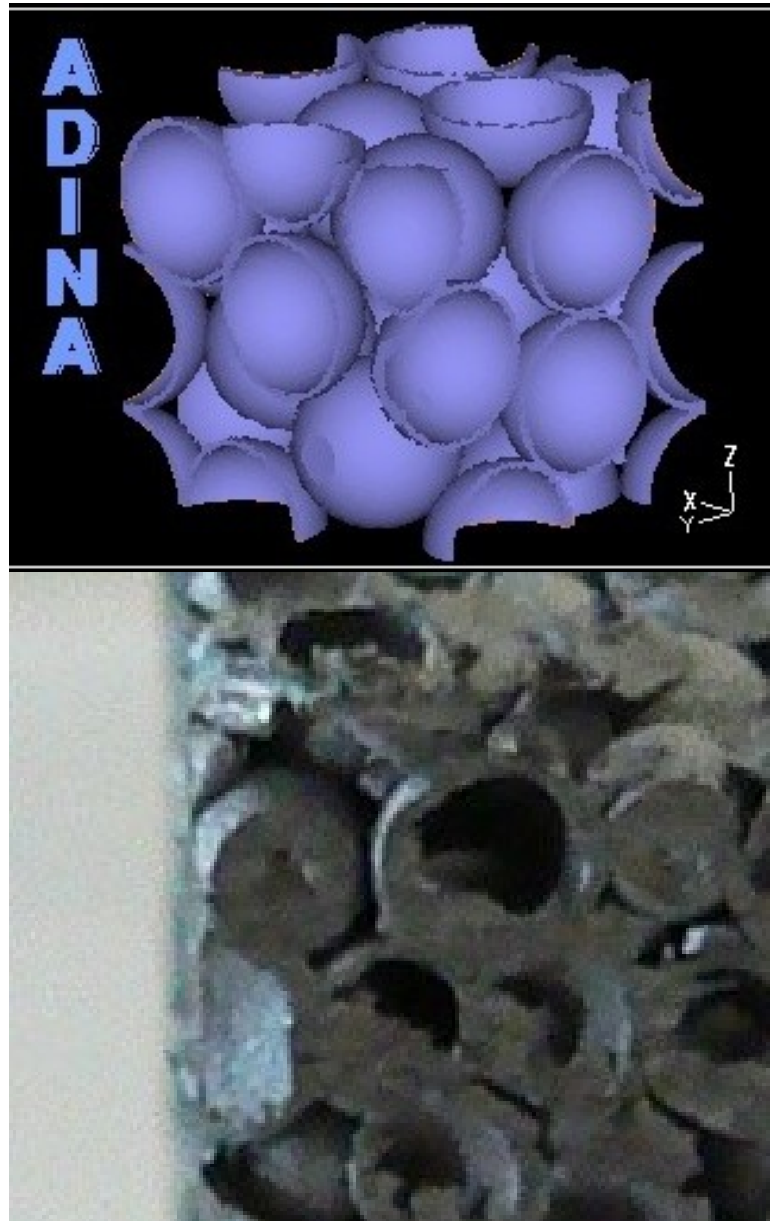


Figure 42: Hollow spheres geometry: sample geometry as generated (left); photograph of the experimentally-tested sintered hollow spheres steel foam (right).

The microstructural components of a physical sintered hollow spheres foam consist of the hollow spheres themselves, and then the welds between those spheres. The spheres have been shown to be in a random close-packed (RCP) stacking (Gao, Yu and Zhao 2008). While previous efforts to simulate such foams have assumed that this RCP stacking could be simplified

to a structured stacking such as face-centered cubic or body-centered cubic, a more accurate simulation requires the stacking to be modeled as random. Several algorithms were considered for the generation of this RCP sphere stacking. Wouterse and Philipse (2006) tested five such algorithms, and showed that two different variations of the “Mechanical Contraction Method” resulted in RCP stackings that were most similar to an experimental stacking in their geometric properties. The algorithmically simpler of those two methods, the “Modified Mechanical Contraction Method”, was chosen for implementation, and operates by the following procedure (Kansal, Torquato and Stillinger 2002) (Wouterse and Philipse 2006):

1. Randomly place spheres of zero size throughout the domain.
2. Increase the size of all spheres by an equal magnitude.
3. Check for overlapping spheres, and move both spheres in each overlap pair away from each other by an equal magnitude. Repeat this step until all overlaps are eliminated.
4. Repeat steps 2 and 3 until the final sphere size is reached.

After spheres are successfully placed, the welds are inserted to connect them. The welds between the spheres in an actual hollow spheres foam are solid cylinders with longitudinally concave sides which curve until they reach a tangent with the sphere (that is, it pinches inwards). However, due to the difficulty of modeling such a shape, two different methods of approximating it were developed. In the first, these welds are approximated by a straight cylinder of a given diameter connecting any spheres that are within some threshold distance of each other. In physical terms, this method would represent the hollow spheres being sintered without applied pressure. In the second method, representing the hollow spheres being sintered with pressure, the Modified Mechanical Contraction Method is adjusted to allow some maximum magnitude of overlap between spheres. Since the actual manufacturing process

would have indented each sphere and not changed the original thickness or mass of either, an additional cylinder is overlaid upon the connection with a height equal to the sum of the thickness of the two sphere walls. This second method is more realistic to the hollow spheres foam that has been tested experimentally, as microscopy showed significant indentation of the spheres due to compaction (see microscopy information in section 3.2.1.1 Hollow Spheres Foam).

Several variables are allowed to vary randomly in this geometry algorithm; these include the sphere size, wall thickness, weld diameter, and sphere location (see Figure 43). All of these do have random variation in the actual manufacturing process, though the precise distribution and distribution parameters are largely unknown. The deterministic variables include the weld structure and some of the input parameters for the Modified Mechanical Contraction Method such as the number of spheres to initially place and the number of overlaps threshold at which to increment the size of the spheres (see Table 19). In the end, this algorithm results in a geometry such as that displayed in Figure 42.

Table 19: Probabilistic distributions assumed for input parameters in hollow spheres geometries.

Input Parameter	Probabilistic Distribution
Sphere radius	Gaussian
Sphere wall thickness	Gaussian
Weld overlap	Deterministic
Initial sphere placement	Deterministic (face-centered cubic), or Uniform random
Number of spheres	Deterministic

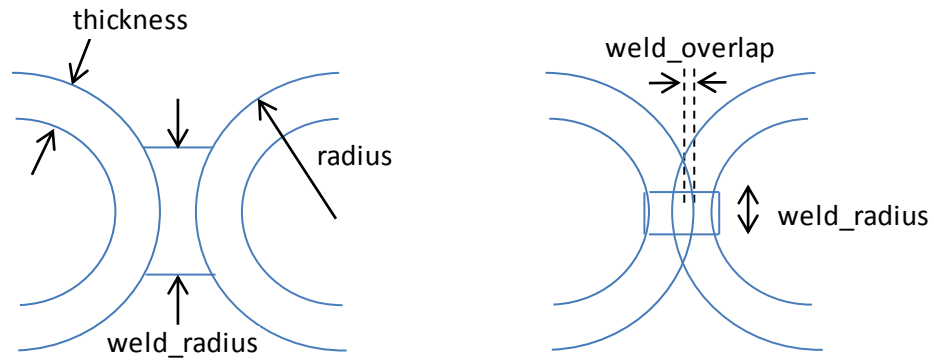


Figure 43: Diagram showing the various geometry characteristics of the hollow spheres algorithm, using the straight cylinder method of representing welds (left), and the overlap method of representing welds (right).

4.3.1.2 General Closed-Cell Geometry

The general closed-cell geometry algorithm, capable of generating geometries for most closed-cell foams, was targeted at accurately representing metal foams produced by the gasar, PCM, powder metallurgy, and high-density composite hollow spheres. These voids are approximately slender ellipsoids for gasar and PCM, something between spheres and ellipsoids for powder metallurgy, and precisely spheres for composite hollow spheres. To represent all of these adequately, the model uses straight cylinders with optional hemispherical caps. These cylinders may then be oriented at any angle and elongated any length.

In each of the manufacturing methods, the void centroids may be placed either as a Poisson point field, or as a random stacking of “lanes” within which voids are centered. In the latter method, the same Modified Mechanical Contraction Method as was used for the hollow spheres geometry is used but with a two-dimensional stacking of void diameters. Each two-dimensional centroid is then used as the center of a “lane” along which to place voids. A further random perturbation may also be applied about that lane centroid in order to prevent voids from being perfectly lined up along the single line of a lane. In either case, overlap may be restricted. Preventing overlap of voids is done by drawing a centerline through the cylindrical

portion of the voids, and then calculating the distance between the centerline line segments of each of the voids, using an algorithm presented by Hoffman (2005).

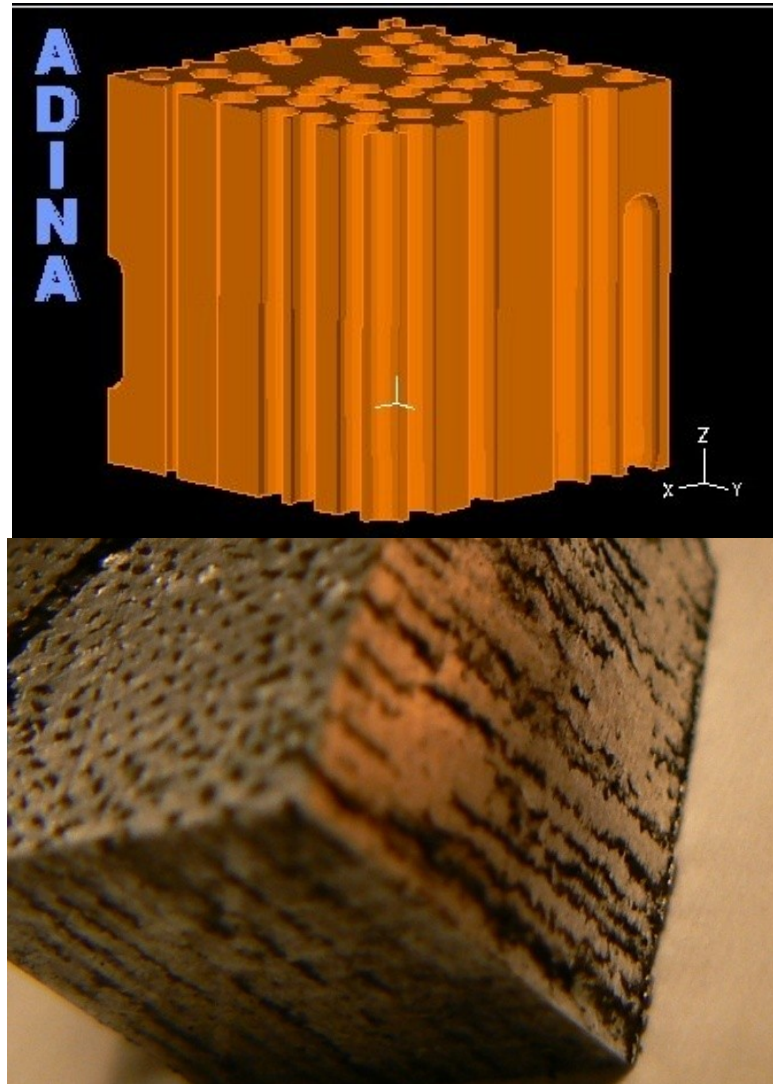


Figure 44: PCM geometry: sample geometry as generated (left); photograph of the experimentally-tested PCM foam (right).

In addition to the random location of the voids, several parameters of the general closed-cell geometry algorithm are also modeled as random variables. The length of the ellipsoid and the diameter of the cylinder are both modeled as Gaussian random variables. The orientation of the voids is modeled as two random variables in the Beta distribution, representing spherical coordinates, with parameters of the distribution chosen to control the

anisotropy of the void orientations. The geometry also allows the minimum distance between voids to be adjusted as a deterministic variable (see Table 20). Upon completion, this algorithm results in a geometry such as that displayed in Figure 44.

Table 20: Probabilistic distributions assumed for general closed-cell input parameters.

Input Parameter	Probabilistic Distribution
Void length	Gaussian
Void diameter	Gaussian
Void orientation θ	Beta ($0 - \pi$)
Void orientation ϕ	Beta ($0 - 2\pi$)
Minimum void distance	Deterministic
Number of voids	Deterministic

After performing several simulations, meshing proved particularly difficult in the region of the hemispherical caps for long and thin voids, such as those in gasar or PCM metal foams. Therefore, an additional option was added to the geometry generation algorithm to create voids which have no hemispherical caps but are otherwise identical to the voids previously described.

4.3.2 Simulation

Once the geometries are generated, they are meshed using second-order tetrahedral elements. These were judged to be most efficiently able to represent linear strain variations across arbitrary three-dimensional geometries. This is particularly important for the hollow spheres model, in which the primary strength mechanism in the foam is the ability of the sphere walls to resist bending. The size of these elements is set at a maximum throughout the body and then automatically refined as necessary. That maximum size is set at approximately 60% of the sphere wall thickness for hollow spheres foams, and at approximately one-sixth of the smallest void diameter for the general closed-cell foams, but adjusted as needed to allow the geometry to be meshed and then solved under the available computing power.

Calculations were originally performed on a desktop server with 16 GB of RAM and two six-core AMD Opteron 2427 processors, with each core running at 2.2 GHz. These models had on the order of 10^6 degrees of freedom with 20 incremental applications of displacement (time steps). Each model typically takes 3-6 hours to solve. More recently, models have been run on a new desktop server with 76 GB of RAM and four six-core Intel Xeon E5645 processors, with each core running at 2.4 GHz. These models have on the order of 10^7 degrees of freedom with 40 time steps, and typically take 6-18 hours to solve.

4.3.2.1 Compression and Tension Testing

Loads and boundary conditions for both compression and tension simulations are applied directly to individual nodes. Uniaxial simulations apply displacements to the +z surface, and then apply fixities in the z direction to the entire -z surface (see Figure 45 for simplified image of boundary conditions). To prevent rotation or rigid body translation of the model during loading, fixities in the x direction are applied to any nodes within 0.05 mm of a material centerline parallel to the y-axis, and fixities in the y direction are applied to nodes within 0.05mm of a material centerline parallel to the x-axis.

Tension tests implemented element deletion in order to simulate fracture failures. ADINA's built-in element deletion algorithm, which only considered a maximum effective strain, was considered inadequate. Therefore, an alternative algorithm was implemented by using a user-defined function for a custom rupture criterion. The “stress modified critical strain” (SMCS) fracture criterion, as proposed by Chi, Kanvinde, and Deierlein (2006), considers both stresses and strains and was intended for complicated geometries. This algorithm is based upon the following function:

Equation 3:

$$\varepsilon_p - \alpha \cdot e^{-1.5 \frac{\sigma_m}{\sigma_e}} > 0 \text{ for } r > l^*$$

Where ε_p is the accumulated effective plastic strain, σ_m is the mean stress, σ_e is the effective or Von Mises stress, and r is the length of the region over which the stresses and strains are being checked. The parameters α and l^* are both material parameters which are intended to be calibrated experimentally, where α is a unitless multiplier and l^* is an effective minimum length.

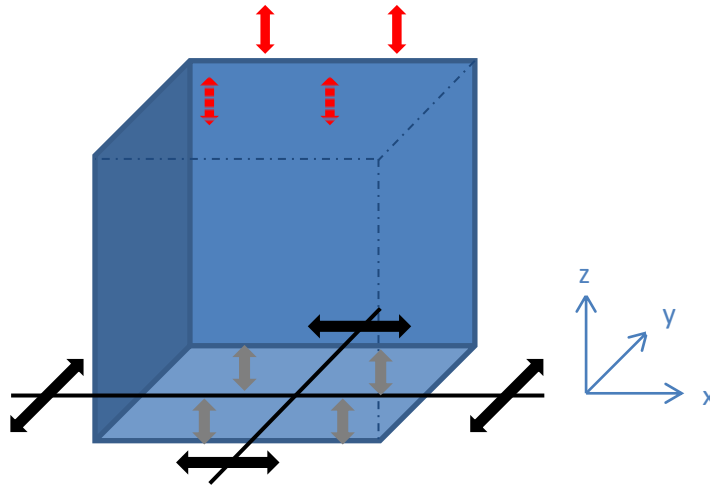


Figure 45: Diagram of boundary conditions applied in uniaxial simulations. Grey block arrows represent the vertical fixity applied to the entire face, black block arrows represent the horizontal fixities applied along centerlines, and red block arrows indicate applied loads.

The ADINA user-defined function mechanism, however, is only capable of testing one isolated element at a time, and has no ability to check any parameters of neighboring elements. Therefore, there is no way to implement the $r > l^*$ check. However, previous experimental calibrations have shown l^* values of approximately 0.1mm to 0.2mm (Chi, Kanvinde and Deierlein 2006), which is close to the size of an individual element in the simulations, so the results should be reasonably close to accurate. The appropriate value of α could only be established by matching fracture strain results for the experimental samples with those of simulations.

4.3.2.2 Shear Testing

There are two options for a type of shear test to implement in the Metal Foams Simulator. The standard shear test for structural materials is a torsion test, as specified by ASTM E143. While this is the preferred method for testing, the absence of a physical torsional test machine and the relative difficulty in implementing the boundary and load conditions in torsional test simulations ruled out this option. Therefore, both the computational simulations and experimental testing were done using the testing standard for shear testing of rigid cellular plastics, ISO 1922. This testing standard involves attaching a thin rectangular sample to two platens, and then pulling one platen in a direction parallel to the platen's face, or equivalent boundary and load conditions in simulations.

Boundary conditions and load applications require a different arrangement in shear than in uniaxial compressive or tensile simulations. The -x face is used as the loading face, and the +x face is held fixed in opposition, with boundary conditions applied only to these faces (see Figure 46). Both sides feature x-displacement fixities across the full areas to oppose bending. A further y-displacement fixity is applied along the centerline of each face to prevent rotation but still allow for any Poisson effects. Finally, a z-displacement fixity is applied only to the +x face, while z-direction loading is applied to the -x face.

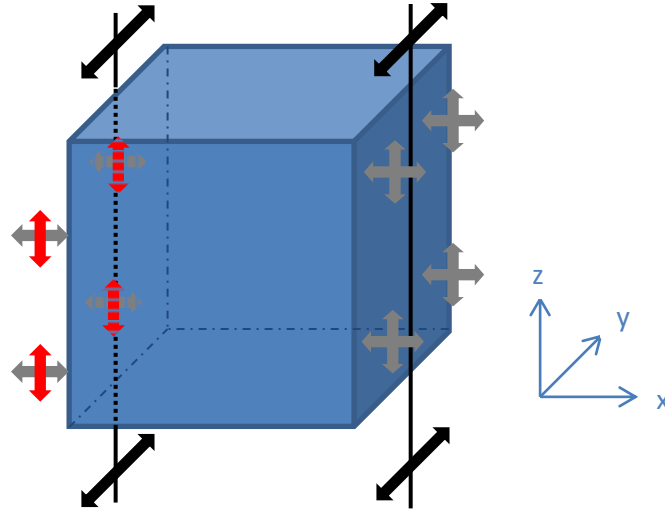


Figure 46: Simplified diagram showing boundary conditions applied to the shear simulation specimen. Grey block arrows indicate fixities applied to the full area of a face, black block arrows indicate fixities applied only along the centerline shown, and red block arrows indicate applied loads.

4.3.2.3 Multiaxial Testing

Multiaxial tests repeat the same pattern of load and boundary condition application as is used in uniaxial simulations. Biaxial tests apply loads perpendicular to the +z and +y faces, while triaxial tests also load the +x face. Boundary conditions are applied on the opposing faces; however, no centerline fixities are applied parallel to loading directions. See Figure 47 for a simplified diagram of boundary conditions applied in a biaxial test; triaxial tests eliminate all centerline fixities and would also fix the -x face and load the +x face.

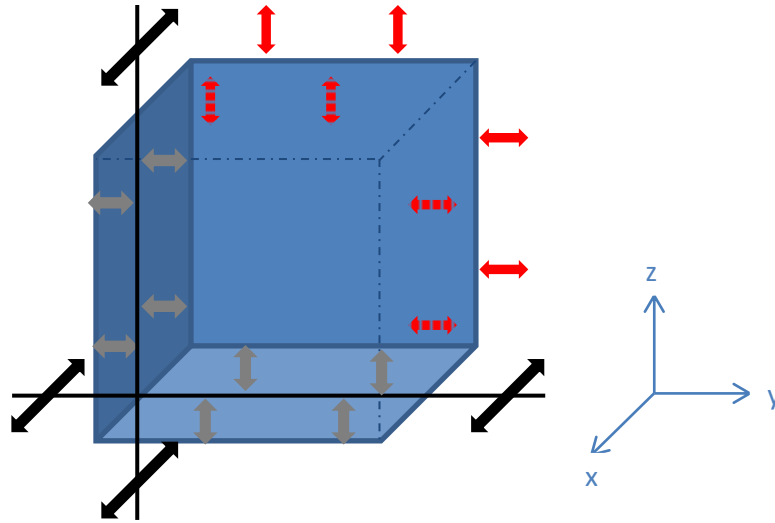


Figure 47: Simplified diagram showing boundary conditions applied during a biaxial simulation. Grey block arrow represent fixities applied to the entire face, black block arrows represent fixities applied only along the centerlines shown, and red block arrows represent loads.

4.3.3 Post-Processing

The post-processing procedure involves exporting various nodal and elemental values into a text file, then importing and processing these using MatLab. First, stress-strain curves are generated by exporting nodal reaction forces, summing all positive reactions on both +z and -z faces, and then dividing by the original area to obtain engineering stress. The elastic modulus is then extracted as the maximum initial slope of this line, and a 0.2% strain offset is applied with this elastic modulus to find the yield stress. When post-processing shear tests, all exported reaction and displacement values are set to return data from parallel to the loading face rather than perpendicular to the face as in uniaxial compression and tension. For multiaxial tests, stress-strain curves in all loaded directions are calculated, and a further stress-strain curve which averages all loaded directions is also evaluated.

To effectively evaluate the elastic and plastic Poisson's Ratio values for metal foams, an incremental Poisson's Ratio was used. At each timestep, the x-displacements of all nodes that originally constituted the -x and +x faces of the material are averaged, and then a difference is

taken between the two. The same thing is done for y-displacements on the -y and +y faces, and these are taken as the x strains and y strains, which are then averaged to obtain a transverse strain. The difference between this transverse strain since the last time step is then divided by the applied z-strain since the latest timestep to obtain an incremental Poisson's ratio, $\Delta\nu$.

Equation 4

$$\Delta\nu = \frac{\Delta\varepsilon_{+x} + \Delta\varepsilon_{-x} + (\Delta\varepsilon_{+y} + \Delta\varepsilon_{-y})}{2} \cdot \frac{1}{\Delta\varepsilon_{z,applied}}$$

Elastic and plastic Poisson's ratio scalars are then estimated by averaging the Poisson's ratio values over each region. For biaxial tests, only the free direction is considered in all Poisson's ratio calculations, and for triaxial tests, Poisson's ratio data is left undefined.

Finally, to more easily identify patterns which relate the microstructure to its apparent macrostructural properties, the percentage of the material which has yielded is extracted at each time step. The percent yielded may be related to the ductility of the material. In comparison, many solid steels show a rapid plastification of the entire material beginning at the yield strain under uniaxial loading. This value is calculated by summing the number of elements which show a non-zero plastic strain at any of their integration points, and then dividing by the total number of elements in the material.

4.3.4 Summary of Assumptions

Numerous assumptions are made throughout the execution of the Metal Foams Simulator. Some are inherent in the ADINA program itself, such as the assumed accuracy of a given mesh. Other assumptions are based upon the absence of human error in inputting values. However, major assumptions made internally within the code of the Metal Foams Simulator itself are shown in Table 21.

Table 21: Table of major assumptions made internally within the Metal Foams Simulator.

Assumption	Explanation / Effect
<i>Geometry Generation</i>	
All regions within the domain except for voids are solid metal.	Microporosity is present in almost all manufacturing methods, so the simulation gives an apparently stiffer and stronger material than experiments would. Note that the microporosity may be partially accounted for by adjusting the material properties of the base metal.
Bilinear material model is sufficient for the solid metal.	For standard carbon steels, this assumption makes minimal difference. However, for any base material with a more complicated stress-strain curve, it may cause inaccuracies proportional to the nonlinearity of the actual behavior.
Kanvinde & Deierlein (2006) provide an adequate method for implementing element deletion	The Kanvinde & Deierlein algorithm is intended to predict fracture of a homogeneous solid steel. The assumption is that it is still valid for the small scales and microporosity present in foams.
The ' $r > l^*$ ' criterion in the Kanvinde & Deierlein fracture criterion may be safely ignored.	There was no way to implement this part of the algorithm, so it is assumed that the algorithm is still valid enough without this check (see section 4.3.2.1 Compression and Tension Testing).
Hollow spheres: the sphere radius, wall thickness, and weld radius are random with a truncated Gaussian distribution.	It is known that there is variance, but the distribution has not been precisely determined.
Hollow spheres: The Modified Mechanical Contraction Method provides a sufficiently accurate representation of the sphere stacking.	While a paper (Wouterse and Philipse 2006) showed good experimental match, that study was based upon marbles, and the hollow spheres method may be different.
Hollow spheres: The curved shape of the weld between spheres may be neglected.	The 'overlap' method represents the weld as a cusp (stress concentrator), and the 'cylinder' method represents it as a straight cylinder.
General closed-cell: The voids may be approximated as either cylinders or cylinders with hemispherical caps.	Different closed-cell manufacturing methods produce differently shaped voids. The accuracy of this assumption depends upon the specific foam being modeled.
General closed-cell: The void height and diameter are random with a truncated Gaussian distribution, and the orientation is random with a beta distribution.	It is known that there is variance, but the distribution has not been precisely determined, and may well differ between closed-cell manufacturing methods as well.
General closed-cell: The spatial distribution of voids may be represented as either uniform random or spaced at Gaussian random intervals.	Different closed-cell manufacturing methods produce differently arranged voids. The accuracy of this assumption depends upon the specific foam being modeled.
<i>Solving</i>	
Inserting centerline fixities to prevent rotation will not unduly introduce other stresses.	There are many ways by which a block of material might be restrained from rotation under service loads. It is believed that these centerline fixities will accomplish this task with the fewest side effects (such as undue stress concentrations or unrealistic constraints of deformities), but it does not eliminate them.
<i>Post-Processing</i>	
Averaging the displacements of an entire face and then comparing opposing faces is an adequate method of calculating Poisson's ratio.	The best method might be to compare and average the relative displacements of individual opposing points, but this is not possible with random geometries. The algorithm used may misinterpret certain geometrical changes as being or not being Poisson effects, though the averaging should cancel most of these.

Key Section Findings

Hollow spheres geometry is developed through a Modified Mechanical Contraction Method to compute a random close-packed sphere stacking. General closed-cell geometry creates either a Poisson point field or random close-packed stacking of "lanes" and then places randomly oriented and sized cylinders with optional hemispherical caps.

The foam is meshed with second-order tetrahedral elements, solved, and then raw displacements and reactions are tabulated to calculate both engineering and true stress, strain, Poisson's ratio, and percentage of elements yielded.

4.4 Results

Key Section Objectives

Validate the simulations as to their similarity to experimental results.

Establish the value and necessity of using a random structure in addition to random characteristics.

Describe results from several simulation matrices which investigated the effects of varying specific geometric parameters.

Demonstrate the ability for simulations to be used in material manufacture and design.

The following sections describe the several simulation sets which have been performed.

Each section begins with a table describing the input parameters used in the simulations (refer to section A.1.2 Definition of Input Variables for the meanings of each of the input parameters).

If multiple values were used, then curly braces "{}" are used to denote a set of values. Note that

features have been added to the Metal Foams Simulator as time has progressed, so some input parameters may not have existed yet at the time the simulations were executed. For the

purpose of reproducibility, however, all currently-available input parameters are listed with

values which will give the same results. As an example, multiaxial simulations were not available

during any of the simulations below, but setting the input parameter 'applied_nstrain=[00 -0.1]'

is the same thing as applying a -0.1 strain in the older version of the code, and so the former is

shown in the table.

4.4.1 Hollow Spheres Tests

Two validation tests and three simulation matrices were performed for hollow spheres simulations. First, an initial validation was performed to test the accuracy of the program against published experimental results. Once experimental tests could be performed on steel foam at the University of Massachusetts, a further validation test was performed. The three simulation matrices include one testing the effects of geometric randomness upon the elastic modulus, one evaluating post-yield behavior with various geometric parameters, and a final one investigating the sensitivity of yield stresses and elastic moduli to various geometric parameters.

4.4.1.1 Initial Validation

Table 22: Input Parameters used in the hollow spheres initial validation simulations.

Simulation Input Parameters		Geometric Input Parameters	
Name	Value	Name	Value
run_part	'all'	radius	0.75
run_location	'local'	radiusstddev	0.075
timeout	9600	thickness	0.05
name	{}	thicknessstddev	0.005
geom_type	'HS'	weld_type	'cylinder'
domain	[0 3; 0 3; 0 3]	weld_overlap	-
nsteps_elastic	20	weld_percent	-
nsteps_plastic	10	weld_max_length	0.025
timestepping	'ATS'	weld_radius	0.15
mesh_element_size	0.14	weld_radiusstddev	0
applied_nstrain	[0 0 -0.1]	wall_truncate	0.75
applied_shear	0	mcm_iterations	20
shear_direction	-	mcm_threshold	0.05
rand_seed	{}	mcm_init_placement	13
base_emodulus	200000	mcm_init_spacing	-
base_ystress	172	mcm_init_lattice	'urandom'
base_poisson	0.3	mcm_init_perturb_radius	0
base_pmodulus	500		
base_kanvinde_alpha	2.6		

Performed on a machine with 16 GB RAM and two 6-core AMD Opteron 2427 processors running at 2.2 GHz each

For hollow spheres validation, a simulation was performed for 1.5mm spheres with standard deviation of 5% and thickness of 0.05mm with standard deviation of 0.005mm, to compare with results from Gao et al (2008). Gao et al (2008) cite ranges of values which they

measured for sphere diameter and thickness; for the purpose of simulations, these ranges were assumed to be equivalent to four standard deviations. The 'cylinder' weld type was used for this simulation.

This validation showed yield strengths less than those reported experimentally. The experimental value was 3.1 MPa, while the simulation produced a yield stress of 2.3 MPa, resulting in a difference of 20%. However, this may also be explained by size effects. That is, the spheres that were cut along the edges of the material have a much lower strength than contiguous hollow spheres, and the simulation had many spheres cut in this manner. Andrews et al (2001) showed that size effects reduced the apparent strength of experimental specimens with dimensions less than 8-10 void diameters to a side. This simulation had lengths of roughly 2.5 void diameters to a side.

The simulation also showed a much higher elastic modulus than expected, at 2560 MPa rather than the experimental 114 MPa. A possible partial explanation for this is that the weld diameters were assumed to be 0.5mm for all spheres in the simulation. However, experimental studies (Gao, Yu and Zhao 2008) showed that the weld diameters vary from 0.08mm to 0.5mm. The smaller area of a 0.08mm weld diameter would provide a greater stress concentration to the sphere and thereby allow more compliance at the same applied displacement. The strong effect that weld diameter has upon the elastic modulus was shown in the study described in section 4.4.1.4 Structural Randomness Analysis, and it probably also affects strength in the same manner, but this was not tested.

The initial validation showed significant deviations, but those deviations have satisfactory explanations in either previous experimental research or in subsequent simulation studies. The simulations were therefore considered to be adequately accurate to merit their continued use in this research.

Further, the use of only scalar values made validation more difficult and more uncertain.

The next section describes validation to experimental results performed at the University of Massachusetts, in which simulations could be validated against a full stress vs strain curve as well as Poisson's ratio vs strain curve.

4.4.1.2 Validation to Experimental Results

Table 23: Input parameters used in hollow spheres validations to experimental results.

Simulation Input Parameters		Geometric Input Parameters	
Name	Value	Name	Value
run_part	'all'	radius	0.9315
run_location	'local'	radiusstddev	0.0475
timeout	9600	thickness	0.0832
name	{}	thicknessstddev	0.0125
geom_type	'HS'	weld_type	'overlap'
domain	{ [0 5.5; 0 5.5; 0 5.5], [0 6.25; 0 6.25; 0 6.25], [0 7; 0 7; 0 7] }	weld_overlap	0.04
nsteps_elastic	20	weld_percent	0.85
nsteps_plastic	20	weld_max_length	-
timestepping	'ATS'	weld_radius	-
mesh_element_size	{ 0.04 - 0.06 }	weld_radiusstddev	-
applied_nstrain	[0 0 -0.1]	wall_truncate	0.9315
applied_shear	0	mcm_iterations	30
shear_direction	-	mcm_threshold	0.01
rand_seed	{}	mcm_init_placement	21
base_emodulus	160000	mcm_init_spacing	-
base_ystress	210	mcm_init_lattice	'urandom'
base_poisson	0.3	mcm_init_perturb_radius	0
base_pmodulus	500		
base_kanvinde_alpha	2.6		

Performed on a machine with 76 GB RAM and four 6-core Intel Xeon E5645 processors running at 2.4 GHz each

Several simulations were performed in order to validate the full stress-strain curve of the simulations with those obtained experimentally. The 'overlap' weld type was developed and used in this study. The study also served the further purposes of validating the 'overlap' algorithm and investigating size effects within the simulations. One 7mm cube, two 6.25mm cubes, and several 5.5mm cubes were simulated. The larger the simulation, the longer it takes to solve and the more difficult it is to mesh successfully, so only one such simulation was performed. The 7mm cube run in this study took roughly three dozen attempts to generate a

continuous and meshable geometry, and took about 72 hours to run from preprocessing through postprocessing on the available 24-core machine.

All inputs were based upon microscopy studies when possible (see section 3.3.1.1 Hollow Spheres Foam). The base metal strength was based upon the experimental test performed (see section 3.3.2.1 Hollow Spheres Foam), and the elastic modulus was assumed to be the standard 200,000 MPa. However, based upon microscopy studies, a microporosity (that is, porosity within the sphere walls themselves) of 20% was estimated and therefore the base metal yield stress and elastic modulus were both reduced by this value. This assumed a linear relationship between relative density and material properties, which is not exactly accurate, but should be close at high relative densities.

The validation simulations showed increasing accuracy as simulations became larger (see Figure 48 and Figure 49). Similar to what was shown in experimental tests by Andrews et al (2001), smaller simulations have lower apparent strengths and stiffnesses. However, those experimental tests showed lower apparent strengths for anything less than a length of 8-10 void diameters to a side, equivalent to 16-20mm for these geometries. At 7mm therefore, the predicted strength should still be lower than the experimental, at least in the absence of other errors. This suggests that the simulations are overestimating the strengths and stiffnesses somewhat, as the 7mm simulation is actually slightly above the experimental in Figure 48.

No known published research has attempted to study the size effects upon Poisson's ratio. However, as is expected, the larger the simulation, the more accurate Poisson's ratio simulations become (see Figure 49). Nevertheless, even at 7mm, Poisson's ratio is still fairly inaccurate, showing a negative slope at a strain of 0.1 rather than positive. While the experimental data is noisy, there is a clear positive trend to the data until a strain of about 0.4,

and this pattern was seen on other Poisson's ratio tests as well. No simulations with Poisson's ratio have been performed past a compressive strain of 0.1.

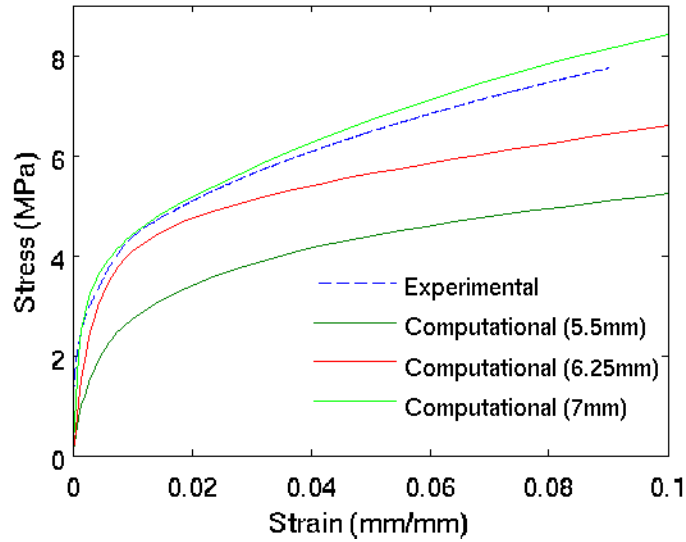


Figure 48: Stress-strain curves for hollow spheres validation to experimental data.

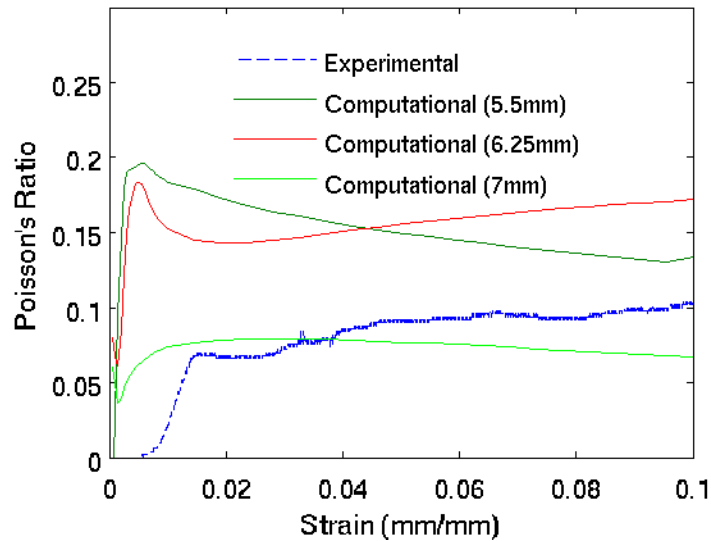


Figure 49: Poisson's ratio vs strain curves for hollow spheres validation to experimental data.

4.4.1.3 Post-Yield Behavior Simulation Matrix

Table 24: Input parameters for hollow spheres post-yield behavior simulation matrix.

Simulation Input Parameters		Geometric Input Parameters	
Name	Value	Name	Value
run_part	'all'	radius	{ 0.75, 1, 1.25, 1.5 }
run_location	'local'	radiusstddev	{ radius / 20 }
timeout	9600	thickness	{ 0.05 - 0.23 }
		<i>(variable was adjusted to result in overall relative densities of roughly 10%, 15%, and 20%)</i>	
name	{}	thicknessstddev	{ thickness / 10 }
geom_type	'HS'	weld_type	'cylinder'
domain	{ [0 4.5; 0 4.5; 0 4.5] - 0 9; 0 9; 0 9] }	weld_overlap	-
nsteps_elastic	20	weld_percent	-
nsteps_plastic	0	weld_max_length	{ thickness / 2 }
timestepping	'ATS'	weld_radius	0.43
mesh_element_size	{ 0.05 - 0.20 }	weld_radiusstddev	0
applied_nstrain	[0 0 -0.004]	wall_truncate	0.75
applied_shear	0	mcm_iterations	40
shear_direction	-	mcm_threshold	0.0435
rand_seed	{}	mcm_init_placement	{ 23 }
base_emodulus	200000	mcm_init_spacing	-
base_ystress	172	mcm_init_lattice	'urandom'
base_poisson	0.3	mcm_init_perturb_radius	0
base_pmodulus	500		
base_kanvinde_alpha	2.6		

Performed on a machine with 16 GB RAM and two 6-core AMD Opteron 2427 processors running at 2.2 GHz each

For the hollow spheres matrix, sphere size was varied from 1.5mm to 3mm in 0.5mm increments, and relative density was varied from approximately 10% to 20%, in 5% increments. Note that relative density cannot be itself set as input variable, so simulations were only targeted at specific relative densities and actual values were off by up to 3% from the target. Overall, specimens were cubes measuring 4.5 mm to each side. The sphere size was assumed to be a random variable with the given mean and a 5% standard deviation, and the relative density was adjusted by means of specifying the shell thickness, which was also assumed to be a random variable but with a 10% standard deviation. These variances were assumed based upon reported experimental values from Gao et al (2008). Parameters for the sphere stacking method were given to form the densest random stacking possible, as determined by manually experimenting with simulation parameters, which was equivalent to about a 55% stacking

density. A typical stress-strain curve and a graph of the percent of the material which has yielded is shown in Figure 50.

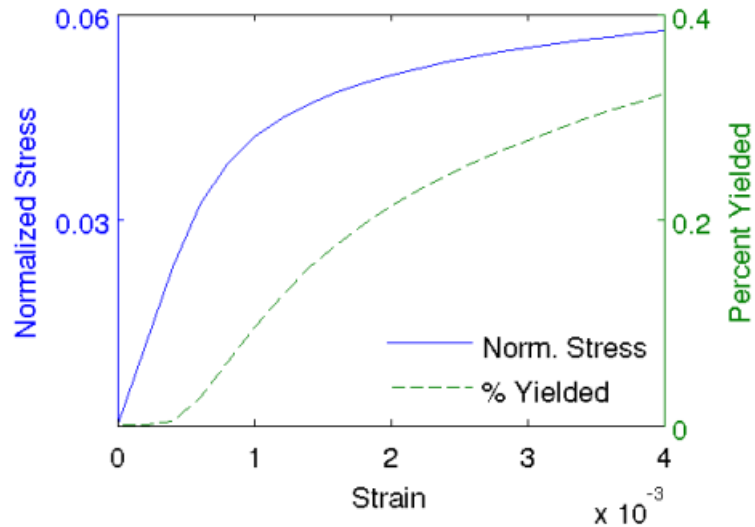


Figure 50: Sample results graph from the hollow spheres test matrix: normalized stress and percent of material yielded versus strain at 23% relative density. Note that stress is normalized by the yield stress of the base metal, 316L stainless steel.

Results show that, at a given relative density, the elastic modulus and yield strength both increase with smaller spheres, as shown in Figure 51. This may be explained by the sphere shell thicknesses in those smaller spheres being thicker in order to provide the extra mass. A thicker shell will provide more bending resistance, and plate bending is the primary strength mechanism in the material. Elastic modulus and yield strength are both affected by this strength increase approximately equally.

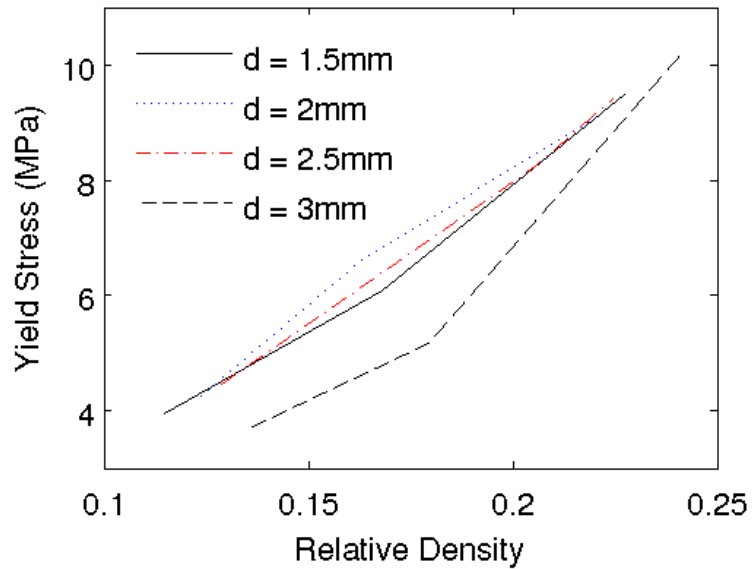


Figure 51: Yield stress vs relative density, showing a rough decrease in the yield stress as the sphere diameter increases. The elastic modulus plot shows a similar pattern.

The Poisson's ratio, however, shows a much more complicated behavior. Above a relative density of approximately 15-20%, the elastic Poisson's ratio is approximately equal to 0.32, and the plastic Poisson's ratio is approximately 0.30. Below 15-20%, however, the elastic Poisson's ratio slowly decreases from 0.16 to 0.14, and the plastic ratio slowly decreases from 0.18 to 0.16. Plots of these two different behaviors are shown in the sample graphs of incremental Poisson's ratio in Figure 52. It should also be noted that four simulations that were in the 15-20% relative density range had to be retried at least once due to the solver failing to converge at a strain of about 0.0012, equivalent to approximately the yield strain and the strain at which the Poisson's ratio curve begins approaching its plastic plateau.

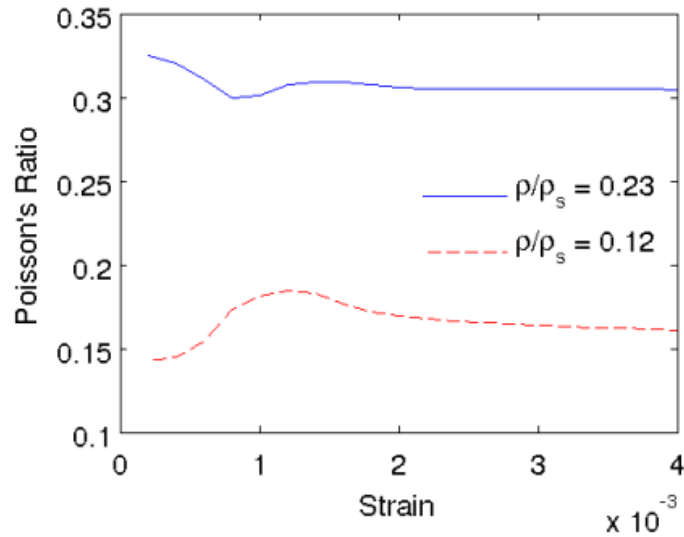


Figure 52: Sample results graph from the hollow spheres test matrix: incremental Poisson's Ratio, at a low relative density and a high relative density.

Fallet et al (2007) did experimental tests and two-dimensional FEM analyses to show that there exists a transition point in the relative density of hollow spheres foams at which a plastic hinge which forms along the weld circumference results in a softening behavior rather than a plateau behavior. With a weld radius of 0.43 mm, as was used in these simulations, they suggest that this transition point would be at a thickness to sphere diameter ratio of about 0.1. The ratio of this presumed transition seen in the three-dimensional simulations performed here is approximately 0.08-0.1, equivalent to 15-20% relative density. The close correlation suggests that this is indeed the phenomenon responsible for the change in behavior.

4.4.1.4 Structural Randomness Analysis

Table 25: Input parameters used in hollow spheres structural randomness analysis.

Simulation Input Parameters		Geometric Input Parameters	
Name	Value	Name	Value
run_part	'all'	radius	1
run_location	'local'	radiusstddev	{ 0, 0.05 }
timeout	1200	thickness	0.13
name	{}	thicknessstddev	{ 0, 0.013 }
geom_type	'HS'	weld_type	'cylinder'
domain	{ [0 7; 0 7; 0 8.66] , [0 6.54; 0 6.54; 0 7.86], [0 6.78; 0 6.78; 0 8.10] }	weld_overlap	-
nsteps_elastic	2	weld_percent	-
nsteps_plastic	0	weld_max_length	0.39
timestepping	'ATS'	weld_radius	0.35
mesh_element_size	{ 0.09 - 0.11 }	weld_radiusstddev	{ 0, 0.10 }
applied_nstrain	[0 0 -0.0004]	wall_truncate	{ 1 - 1.5 }
applied_shear	0	mcm_iterations	40
shear_direction	-	mcm_threshold	0.0263
rand_seed	{}	mcm_init_placement	-
base_emedulus	200000	mcm_init_spacing	2
base_ystress	172	mcm_init_lattice	'fcc'
base_poisson	0.3	mcm_init_perturb_radius	{ 0, 2, 1, 0.5, 0.25, 0.125 }
base_pmodulus	700		
base_kanvinde_alpha	100		

Performed on a machine with 16 GB RAM and two 6-core AMD Opteron 2427 processors running at 2.2 GHz each

A series of simulations as well as a statistical analysis were performed to evaluate the effect of the structural and material randomness of hollow spheres foams upon the homogenized elastic modulus of the foam. This section attempts to evaluate the efficacy of one of the most recent and detailed mathematical models of the elastic modulus of hollow spheres foams, which is based upon an face-centered cubic (FCC) sphere structure, as well as attempts to quantify the amount by which the random structure of the actual material affects the homogenized elastic modulus of the material. First, a second moment analysis is performed upon the aforementioned mathematical model, assuming random inputs. Then, the results of this analysis are extrapolated to a larger structure by means of establishing Voigt and Reuss bounds. In order to evaluate the effect of structural randomness, a series of simulations of an increasingly random structure are performed using the ADINA finite element analysis program.

Finally, a major reason that geometric randomness affects the macroscopic material properties is that, as randomness increases, the spheres end up with fewer other spheres in contact with them, and so fewer welds are present. Therefore, the threshold distance at which spheres are assumed to have a weld connecting them is varied in order to test this theory. All of these results are compiled and compared, and conclusions are made.

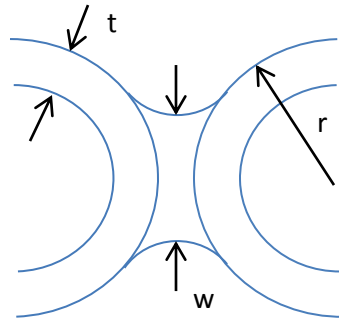


Figure 53: Drawing of the meaning of each of the variables used in describing hollow spheres foams.

While assuming that hollow spheres foams were adequately represented by a face-centered cubic structure, Gasser, Paun, and Bréchet (2004) proposed that the essential material parameters of hollow spheres foams for predicting effective macroscopic properties were the sphere outer radius (r), sphere shell thickness (t), and the radius of the weld neck between spheres (w), the precise meaning of which are shown in Figure 53. Through mathematical approximation, they suggested that the elastic modulus would be a function of t/r and w/r . Finally, they ran a series of simulations upon representative FCC unit cells of varying parameters using the ABAQUS finite element program. The team performed 25 realizations of simulations with varying shell thickness and sphere radius, using a representative unit cell with periodic boundary conditions, as shown in . Using curve-fitting to derive coefficients, they suggested that the following equation could be used to predict the effective macroscopic elastic modulus of a hollow spheres steel foam:

Equation 5

$$\hat{E} = \frac{E_c}{E_{c,s}} = \left[1.14 \cdot \left(\frac{w}{r}\right) + 0.587 \cdot \left(\frac{w}{r}\right) + 0.118 \right] \cdot \left(\frac{t}{r}\right) + \left[-30.1 \cdot \left(\frac{w}{r}\right) + 10.5 \cdot \left(\frac{w}{r}\right) + 0.826 \right] \cdot \left(\frac{t}{r}\right)$$

The variables r , t , and w are as described above. E_f is the effective elastic modulus of the foamed metal, which is then normalized by E_s , the elastic modulus of the solid base metal. This equation, shown as Equation 5, is not entirely accurate at predicting the elastic modulus of all foams, as it is an empirical equation calibrated only to a few experimental tests of materials with relative densities in the 4% to 8% range. For the particular foam tested experimentally at the University of Massachusetts (see section 3.3 Results), this equation predicts an elastic modulus of about 10,000 MPa, but tests showed a modulus of about 3,200 MPa. However, it is used in this section to help evaluate the effect of material randomness.

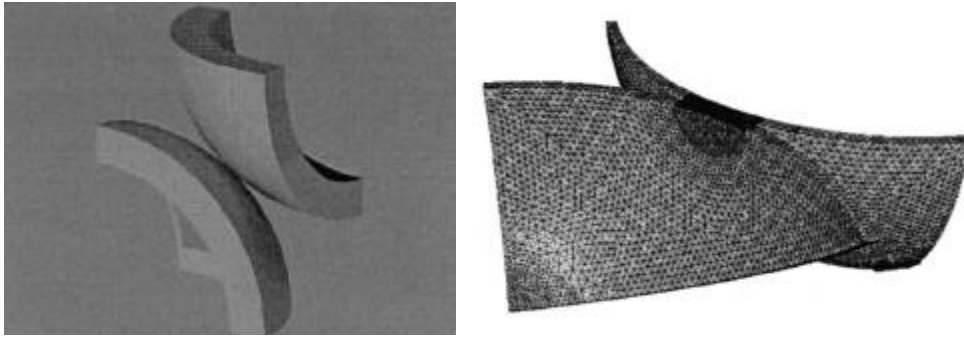


Figure 54: Images of the representative unit cells used in the Gasser, Paun, and Bréchet (2004) simulations used to develop Equation 5.

In an actual metal foam, the input parameters would not be deterministic; there is some variation inherent in the hollow spheres manufacturing process resulting in the input parameters varying across the material. Therefore, r , t , and w are set as random variables as follows. Capitalized letters are used to indicate random variables, and the mean values, indicated by the first number in each pair, are equivalent to a 20% relative density:

- $R \sim N(1, 0.05^2)$ mm
- $T \sim N(0.13, 0.013^2)$ mm

- $W \sim N(0.35, 0.1^2)$ mm

With no more specific information otherwise available, all variables are assumed to be of Gaussian distribution. The variances are based upon ranges experimentally determined by Gao et al (2008); the maximum and minimum values in the ranges that they reported are assumed to be approximately two standard deviations from the mean.

Analytically, it is not possible to calculate the mean and variance for Equation 5 given that the expected value of $1/R^n$ is not well-defined. Therefore, first- and second-order Taylor Series approximations of R are used instead. Much of this calculation is purely algebraic, but is based upon the formula that for a random Gaussian variable X , the expected value of X^2 is $\mu_X^2 + \sigma_X^2$, and the expected value of two independent Gaussian variables multiplied together is the expected value of each variable multiplied together. Calculating these results in the following equations:

Equation 6

$$\hat{E}_{first\ order} = 5.14 \cdot W^2 T + 0.587 \cdot WT + 0.118 \cdot T - 30.1 \cdot W^2 T^2 + 10.5 \cdot WT^2 + 0.826 \cdot T^2 - 15.42 \cdot W^2 T + 1.174 \cdot WT + 0.118 \cdot T - 20.4 \cdot W^2 T^2 + 31.5 \cdot WT^2 + 1.652 \cdot T^2 \cdot R^{-1}$$

Equation 7

$$\hat{E}_{second\ order} = \hat{E}_{first\ order} + 61.68 \cdot W^2 T + 3.522 \cdot WT + 0.236 \cdot T - 602 \cdot W^2 T^2 + 126 \cdot WT^2 + 4.956 \cdot T^2 \cdot R^{-2} - 2R + 1$$

Applying the expected value operator to each of these equations to find the mean ($E[\hat{E}]$) and variance ($E[(\hat{E} - \mu_{\hat{E}})(\hat{E} - \mu_{\hat{E}})]$) results in the following:

$$\hat{E}_{first\ order} \sim (0.1393, 0.0136^2)$$

$$\hat{E}_{second\ order} \sim (0.1411, 0.0422^2)$$

Finally, to confirm the accuracy of these results to the predictions of the formula model, a Monte Carlo simulation was performed upon the original \hat{E} equation, Equation 5, as derived by Gasser, Paun, and Brechet (2004). These simulations were only plugging in values to the mathematical equation, but with 100,000 iterations, they precisely resulted in the following:

$$\hat{E} \sim (0.1403, 0.0421^2)$$

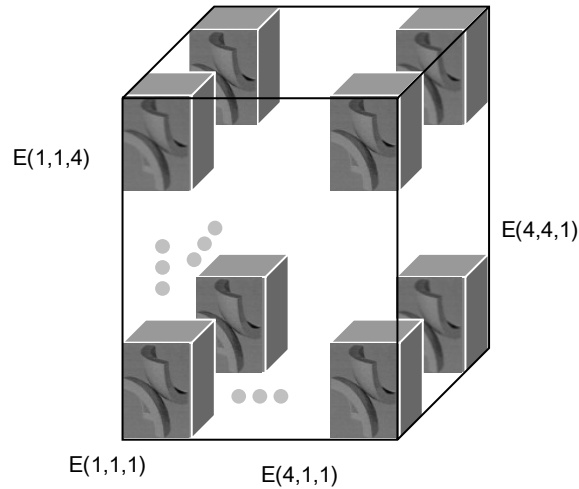


Figure 55: Diagram of the meaning of the matrix of unit cells

Therefore, the second-order Taylor Series approximation provides very precise results to Equation 5. The first-order Taylor Series approximation captures the mean value well, but does very poorly capturing the variance. However, it is still a marked improvement upon simply plugging in the mean values of R , T , and W , which results in $\hat{E} = 0.1377$.

The material properties vary spatially across a hollow sphere foam, so in order to represent this, the unit cell must be repeated several times over a volume. For this paper, a volume of $4 \times 4 \times 4$ unit cells was chosen, as shown in Figure 55. The small size was chosen as a result of computational power restrictions and because it was considered desirable for this analysis to have similar dimensions to the ADINA simulations to facilitate better comparisons.

Considering each unit cell to take up a volume of $1.0 \times 1.0 \times 1.41$ mm, an overall volume of $4.0 \times 4.0 \times 5.64$ mm was created, which is approximately the maximum size which can be simulated with available computing power in ADINA. As unit cells are used in this analysis, the voids within the material are inherently present in each unit cell, and therefore need not be

otherwise accounted for. Voigt and Reuss bounds on possible values may be derived either analytically by Taylor Series approximation, or through Monte Carlo simulation, as shown below:

Equation 8a and b:

$$\hat{E}_{Voigt} = \left[\frac{1}{V} \cdot \int_V E_{ijk} dV \right] = \left[\frac{1}{54} \cdot \sum_{i=1}^3 \sum_{j=1}^3 \sum_{k=1}^3 E_{ijk} \right] = 0.1224$$

$$\hat{E}_{Reuss} = \left[\frac{1}{V} \cdot \int_V \frac{1}{E_{ijk}} dV \right] = \left[\frac{1}{54} \cdot \sum_{i=1}^3 \sum_{j=1}^3 \sum_{k=1}^3 \frac{1}{E_{ijk}} \right] = 0.1403$$

As Voigt and Reuss bounds set the minimum and maximum possible mean values, the mean elastic modulus should therefore be between 0.1224 and 0.1403, assuming that the unit cell model is accurate.

To evaluate the accuracy of the unit cell model, several full-size simulations of an FCC stacking of hollow spheres were performed. Initially, two different types of simulations were performed: first, a completely deterministic simulation was performed with all spheres having radius, thickness, and weld radius equal to the mean values for each variable; second, the radius, thickness, and weld radius were allowed to take on their random values, with Gaussian distributions of mean and variance as used for the unit cell model.

In a pure FCC simulation, such as when all the spheres are deterministically the same size, spheres may simply be placed into the lattice and simulated welds used to connect them. The actual welds between the spheres in a real metal foam have solid circular cross-sections with concave sides which curve until they reach a tangent with the sphere. However, due to the difficulty of modeling such a shape, these welds are approximated by a straight cylinder connecting any spheres that are within some threshold distance of each other. As all spheres have exactly the same distance between them in this case, welds are created at all locations, finally resulting in a geometry as shown in Figure 56.

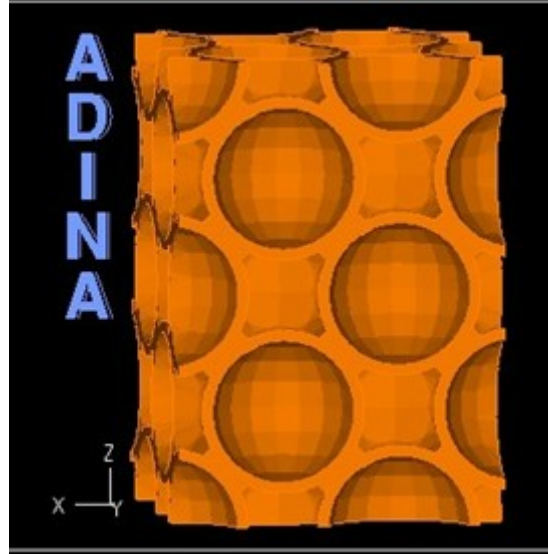


Figure 56: ADINA image of the geometry of a deterministic model

If the sphere sizes vary across the material, on the other hand, then the material can no longer be considered as a pure FCC structure, as there may be overlap between two adjacent spheres that have above average size. In order to correct this overlap, an algorithm normally used to generate a purely random stacking is employed.

The deterministic simulation results in an elastic modulus of 0.1418, which is approximately equal to the 0.1403 Voigt bound. Thirty Monte Carlo simulations were performed with random sphere radii, shell thicknesses, and weld radii (computational time: about 72 hours). Note that the structure of the hollow spheres is still considered to be nearly FCC for all simulations thus far. The results of these 30 simulations is a nearly Gaussian distribution, as shown in the normal probability plot of Figure 57, and the following mean and variance:

- $\hat{E}_{random\ inputs} \sim (0.0963, 0.0152^2)$

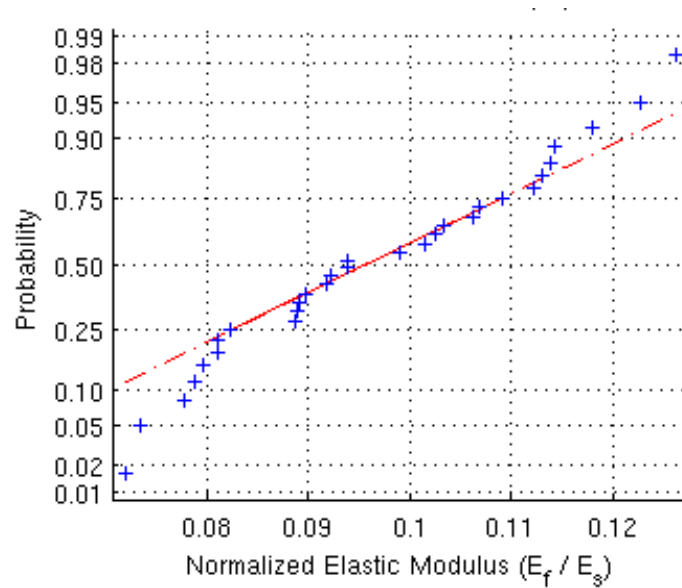


Figure 57: Normal probability plot, showing a nearly Gaussian distribution to the elastic modulus of 30 random samples.

One possible explanation for this decrease in the mean value of the elastic modulus is that the number of welds in the geometry decreases. If two adjacent spheres have smaller radii than the mean, then they may end up with more than 0.13 mm of space between them, which is considered to be the threshold value for when welds are assumed to have been created. To test this theory, that threshold value is increased to 0.39 mm, or three times the mean shell thickness of the spheres. A typical image of such a geometry with random inputs is shown in Figure 58. Running 30 of these simulations results in the following mean and variance:

- $\hat{E}_{random\ inputs} \sim (0.1329, 0.0087^2)$

This value is securely within the Voigt / Reuss bound range, and nearly 40% higher than the original random simulations, suggesting that, at the least, the absence or presence of welds between spheres plays a very major role in setting the elastic modulus of the material.

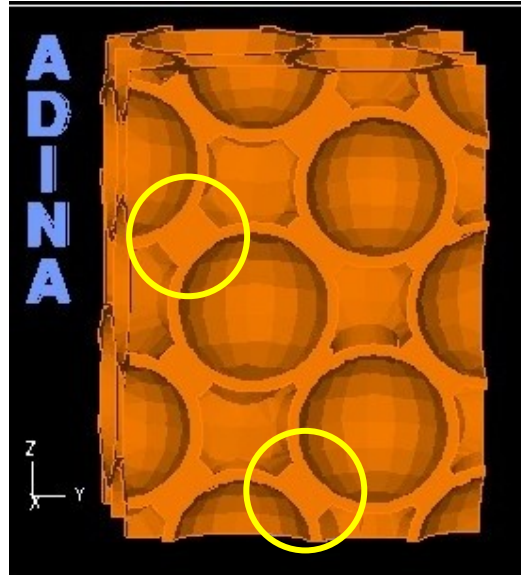


Figure 58: Typical image of a geometry with random inputs and a 0.39mm weld diameter. Note the particularly long welds, two of which are circled in yellow, which would not have been created with the 0.13mm threshold.

While simulations of FCC materials suggest that unit cell models are relatively accurate for these, actual hollow spheres foams have no such regular stacking pattern. To quantify this effect, an FCC structure is established as for the prior simulations, but then a random perturbation is applied to each sphere. This perturbation is defined by a radius about the FCC location of the sphere center, within which a new, uniformly random location for the sphere center is picked. Several ADINA simulations were performed with such random perturbations, with 10 simulations performed at each of five increasingly large perturbation radii. Further, this set of simulations was performed twice, once with a weld creation threshold of 0.13 mm and one, following the results of the FCC simulations, with a weld creation threshold of 0.39 mm. Note that the sphere radius, sphere thickness, and weld radius are all still considered as random variables as well. An image of a typical geometry generated with a 1mm random perturbation radius is shown in figure . The results for the means and variances at each perturbation radius, and for both weld creation thresholds, are plotted in Figure 60.

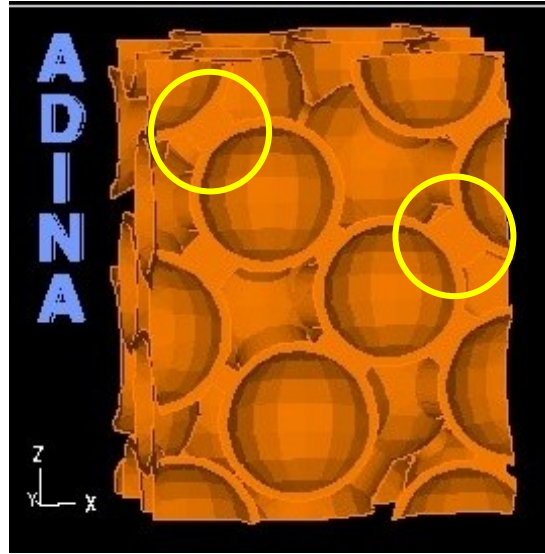


Figure 59: Image of a typical geometry generated with a 1mm random perturbation radius and a 0.39mm weld threshold. Note that there are two missing welds. There also some particularly long welds, two of which are circled in yellow, which would not exist with a 0.13mm weld threshold.

These mean values of elastic modulus decrease similarly over increasing perturbation radii for each of the weld thresholds, but there is a clear difference in magnitude displayed, with the higher weld threshold showing significantly higher stiffnesses. With the lower Voigt bound of 0.1224, the smaller weld threshold falls out of the range immediately, but the larger weld threshold remains within the range until a perturbation radius of 0.25 mm. Note that, for the 0.39 mm weld threshold, the number of welds does not start to decrease until a perturbation radius of 0.5 mm, which coincides with when the mean of the elastic modulus begins to rapidly decrease. This fact was verified by manually examining simulations and observing that the number of welds created by the geometry algorithm did not begin to decrease until higher perturbation radii. A perturbation radius of 2 mm is effectively a completely random structure, and hence the graphs appear to be forming asymptotes by about that point. Due to the small sample size of 10 at each data point, the standard deviations have a high error associated with them, but their general trends may still be analyzed. In these, the standard deviation of the

elastic modulus for the 0.13 mm weld threshold decreases with increasing perturbation radius, but for the 0.39 mm weld threshold remains relatively constant throughout.

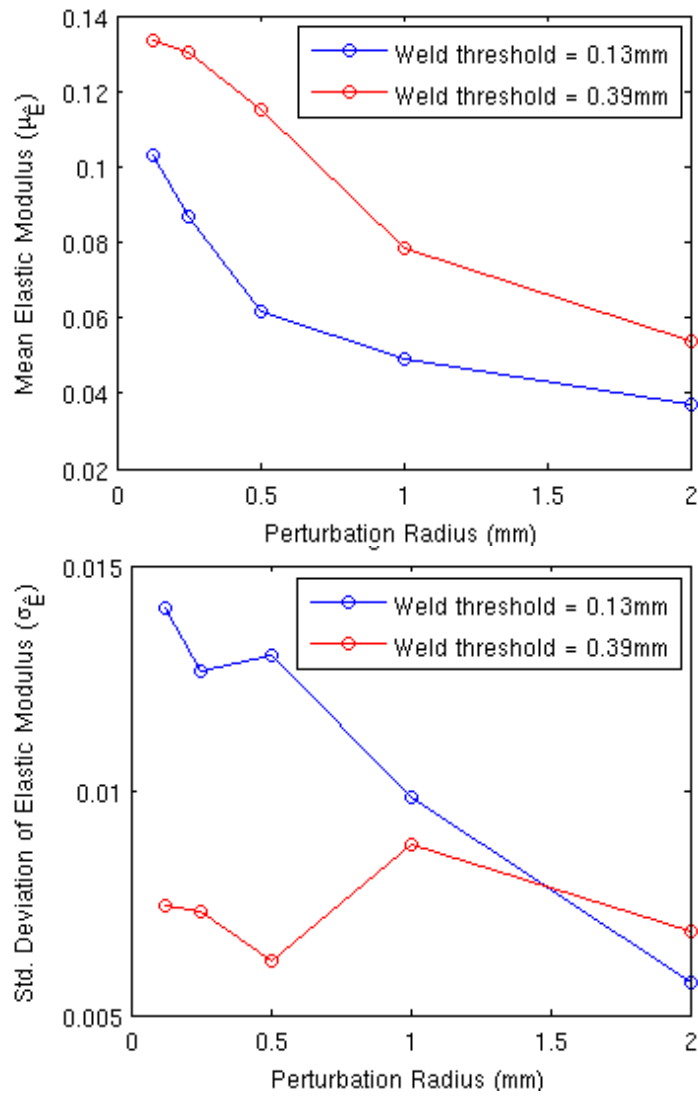


Figure 60: Mean values (top) and standard deviations (bottom) of the normalized elastic modulus for increasing perturbation radii.

Researchers have previously attempted to solve the problem of predicting an effective macroscopic elastic modulus for hollow spheres foams by means of assuming that the foam is equivalent to a regular stacking of hollow spheres and then deriving properties for unit cells. This section has attempted to expand and evaluate this idea by first examining the effect of random variable inputs upon the results of a mathematical model for an FCC unit cell proposed

by Gasser et al (2004). Then, these results were extended out to a three-dimensional matrix of random unit cells in order to establish Voigt and Reuss bounds for an effective macroscopic elastic modulus. This range was then compared against ADINA simulations performed of a deterministic FCC hollow spheres structure, an FCC structure with random material parameters, and a structure with randomly perturbed sphere center locations and random material parameters. After observing a rapid decrease in the elastic modulus with increasing randomness, one theory as to the cause was checked by increasing the maximum sphere spacing threshold requirement for a weld to be assumed. The mean and variance of all analyses are displayed in Table 26.

Table 26: Overall summary of all means and variances of elastic modulus for all representations of hollow spheres foams.

Geometry	Simulation Type	Weld Threshold = 0.13 mm		Weld Threshold = 0.39 mm	
		Mean	Variance	Mean	Variance
<i>Unit Cell</i>	1 st Order Taylor Series	0.1393	0.0136 ²	0.1393	0.0136 ²
	2 nd Order Taylor Series	0.1411	0.0422 ²	0.1411	0.0422 ²
	Monte Carlo	0.1403	0.0421 ²	0.1403	0.0421 ²
<i>Matrix of Unit Cells</i>	Voigt / Reuss Bounds	0.1224 < \bar{E} < 0.1403		0.1224 < \bar{E} < 0.1403	
<i>FCC ADINA Simulation</i>	Deterministic at Mean	0.1416	–	0.1416	–
	Random Input	0.0963	0.0152 ²	0.1348	0.0089 ²
<i>Randomly Perturbed ADINA Simulation</i>	0.125 mm Perturbation	0.1031	0.0141 ²	0.1337	0.0074 ²
	0.25 mm Perturbation	0.0866	0.0126 ²	0.1303	0.0073 ²
	0.5 mm Perturbation	0.0619	0.0130 ²	0.1153	0.0062 ²
	1 mm Perturbation	0.0492	0.0098 ²	0.0787	0.0088 ²
	2 mm Perturbation	0.0370	0.0057 ²	0.0541	0.0068 ²

Overall, the mean values for elastic modulus show strong agreement for unit cells up through the ADINA FCC simulation with deterministic inputs, all showing values of about $\mu_{\bar{E}} = 0.14$. However, once the input variables are randomized, the elastic modulus begins rapidly decreasing. This effect is only accentuated is randomness is introduced into the structure of the material by applying random perturbations. The greater the perturbation, the lower the elastic modulus was shown to be, eventually decreasing to 40% of the stiffness with no perturbations, or 25% of the fully deterministic stiffness. However, the variance predicted by the Gasser et al

equation, Equation 5, was shown by all simulations to be a sharp overestimate, at nearly eight times larger than the greatest variance observed in simulations. However, due to the small sample size of ten at nearly all data points, it is possible that this gap may decrease with further simulations.

In order to test the theory that the number of welds present has a strong effect upon the effective stiffness of the material, two sets of simulations were performed, one with a threshold of 0.13mm and the other with a threshold of 0.39mm at which welds were assumed to exist between spheres. In these simulations, making the input variables random only caused a 5% decrease in the stiffness, and applying random perturbations only decreased the stiffness to 40% of the deterministic strength. There was also only a very minimal (less than 10%) decrease in stiffness observed as long as welds were still intact, which was the case up until a random perturbation radius of 0.25 mm (as verified from examining internal simulation data). These results seem to support the theory that the loss of weld connections is indeed a very major cause, though certainly not the exclusive cause, of the loss of stiffness in the system as randomness increases.

These results suggest that, while mathematical models based upon regular periodic stackings of hollow spheres are certainly useful, they are likely to overestimate the actual effective stiffness of the material. The major reason for this is that regular stacking patterns assume that all weld connections between spheres are intact, which has been shown to be unlikely given the random characteristics and structure of the material. Therefore, future mathematical models should be based upon truly random stacking patterns of the hollow spheres, or at the least, should include some adjustment for the loss of weld connections inherent in a manufactured hollow spheres foam.

Later microscopy studies (see section 3.3.1.1 Hollow Spheres Foam) showed that there are indeed many spheres which are located near to each other but between which there is no physical connection. It was not possible to quantify this effect, but qualitatively, its existence was confirmed, as shown by example in Figure 61.

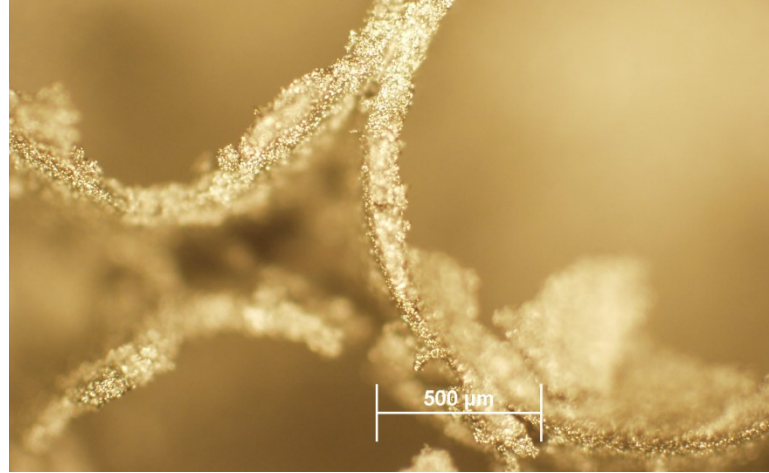


Figure 61: Microscopy image showing the two spheres on the left near to each other, but having no physical connection.

4.4.1.5 Sensitivity Analysis for Compression Tests

Table 27: Input parameters used in hollow spheres sensitivity analysis for compression tests.

Simulation Input Parameters		Geometric Input Parameters	
Name	Value	Name	Value
run_part	'all'	radius	{ 0.83, 0.93, 1.03 }
run_location	'local'	radiusstddev	0
timeout	9600	thickness	{ 0.073, 0.083, 0.093 }
name	{}	thicknessstddev	0
geom_type	'HS'	weld_type	'overlap'
domain	[0 6.25; 0 6.25; 0 6.25]	weld_overlap	{ 0.03, 0.04, 0.05 }
nsteps_elastic	20	weld_percent	0.85
nsteps_plastic	10	weld_max_length	-
timestepping	'ATS'	weld_radius	-
mesh_element_size	{ 0.05 - 0.065 }	weld_radiusstddev	-
applied_nstrain	[0 0 -0.1]	wall_truncate	0.93
applied_shear	0	mcm_iterations	30
shear_direction	-	mcm_threshold	0.0001
rand_seed	{}	mcm_init_placement	{ about 33 }
base_emodulus	160000	mcm_init_spacing	1.82
base_ystress	{ 132, 210, 303 }	mcm_init_lattice	{ 'urandom', 'fcc' }
base_poisson	0.3	mcm_init_perturb_radius	0
base_pmodulus	500		
base_kanvinde_alpha	2.6		

Performed on a machine with 76 GB RAM and four 6-core Intel Xeon E5645 processors running at 2.4 GHz each

Using the hollow spheres validation simulation described in section 4.4.1.2 Validation to Experimental Results as the basis point, a sensitivity analysis was performed to explore the effects of varying specific microstructural parameters. The varied parameters are those which could be adjusted in the actual manufacturing process, including base metal yield strength, sphere diameter, sphere shell thickness, and sphere overlap distance. The last represents and is physically equivalent to the amount of pressure applied during the sintering process.

Three points were simulated for each parameter in order to acquire sensitivities: the central value, one slightly below, and one slightly above. Sensitivities were defined by first-order central differences normalized to the central value of elastic modulus of yield stress (see Equation 9 and Equation 10, respectively, where p is the varied parameter).

Equation 9

$$E_{norm} = \frac{E_{upper} - E_{lower}}{(p_{upper} - p_{lower}) \cdot E_{central}}$$

Equation 10

$$f_{y,norm} = \frac{f_{y,upper} - f_{y,lower}}{(p_{upper} - p_{lower}) \cdot f_{y,central}}$$

At each point, one simulation was performed with a deterministic, face-centered cubic (FCC) geometry (see Figure 62), and two were performed with random geometries. All other parameters were set as deterministic. It is important to note that when varying the sphere diameter or the sphere shell thickness, this also changed the relative density of the material, so some of the change in mechanical properties is due to there simply being more or less mass within the volume. Further, the relative density of a specimen with a random geometry is lower than that with a face-centered cubic geometry.

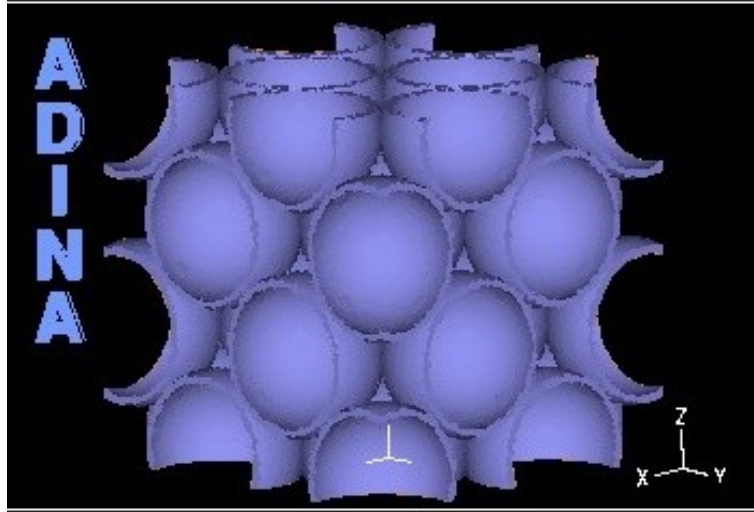


Figure 62: Sample image of a deterministic, face-centered cubic geometry used in the sensitivity analysis simulations.

In the results, it was observed that the variation was close to linear for most parameters over the range simulated, though became noticeably non-linear when varying the sphere diameter, as can be seen from the graphs in Figure 63. Providing an alternative view of the data, results are shown in Table 28 normalized to the base foam properties. All results for random simulations should be taken with some doubt as to their precision as only two random simulations were run for each parameter set.

As was expected, changing the yield stress of the base metal had a negligible effect upon the elastic modulus, and a close to 1:1 linear relationship with effective foam yield stress. Sphere diameter adjustments strongly affected the relative density as well, but nevertheless showed that smaller spheres have slightly higher strengths than larger spheres. This is expected since the overall foam strength is highly dependent upon the bending stress in the sphere walls. The shell thickness results are very close to proportional with the change in relative density. The weld overlap, however, has negligible effects upon the relative density, yet shows strong effects upon the foams' elastic moduli and yield stresses. It is believed that the lower strengths and stiffnesses in the random upper-bound simulations for weld overlap are anomalies of

randomness and that more simulations would show an average higher than the base values, as is seen in the FCC simulations. From these results, it may be suggested that stronger and stiffer foams should be manufactured by using spheres that are as small as possible and using higher compression during sintering (so as to increase the weld overlap).

Table 28: Normalized results data from sensitivity analysis, normalized to the base value.

Varying	Bound	Value	Relative Density		Elastic Modulus		Yield Stress	
			FCC	Random	FCC	Random	FCC	Random
Base Yield Stress (MPa)	Lower	0.63	1.00	1.00	1.00	0.99	0.66	0.69
	Base	1.00	1.00	1.00	1.00	1.00	1.00	1.00
	Upper	1.45	1.00	1.00	1.00	0.91	1.41	1.17
Sphere Diameter (mm)	Lower	0.89	1.13	1.06	1.25	0.94	1.25	1.04
	Base	1.00	1.00	1.00	1.00	1.00	1.00	1.00
	Upper	1.11	0.73	0.82	0.49	0.51	0.43	0.74
Shell Thickness (mm)	Lower	0.88	0.88	0.86	0.88	0.82	0.89	0.91
	Base	1.00	1.00	1.00	1.00	1.00	1.00	1.00
	Upper	1.12	1.11	1.08	1.12	1.14	1.11	1.20
Weld Overlap (mm)	Lower	0.75	0.99	0.98	0.89	0.89	0.88	0.92
	Base	1.00	1.00	1.00	1.00	1.00	1.00	1.00
	Upper	1.25	1.00	0.96	1.10	0.90	1.10	0.97

By utilizing these sensitivity results from computational simulations, the optimal material characteristics for a desired combination of elastic modulus and yield stress may be determined. This set of simulations only provides enough data to reliably obtain first-order sensitivities near to 14% relative density (see Table 29). However, with more such simulations it would be possible to determine the material properties needed in order to achieve any mechanical properties within the range afforded by the hollow spheres method. Complete scaling laws could be developed, and the important dependent parameters could be determined.

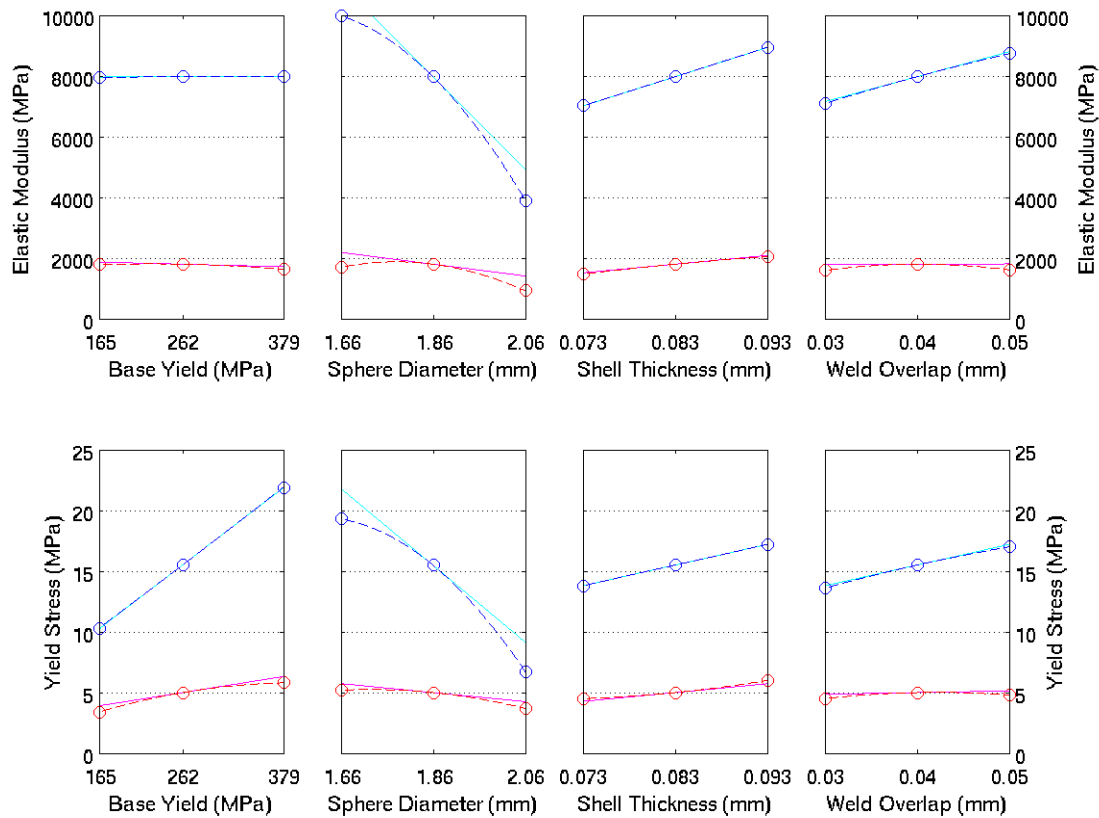


Figure 63: Graph of all simulations performed in sensitivity analysis. Blue points are FCC simulations; red points are the average of the two random simulations performed at each point. The first-order central difference slopes are shown as solid lines, and the second-order curve fits are shown as dashed lines.

Experimental and computational studies in this thesis have shown that the scaling laws proposed by Gibson and Ashby (2000) and several others, which are based solely upon relative density are imprecise and provide, at best, only rough ballpark estimates for material properties. However, if other important parameters are identified, new and more precise scaling laws could be developed. Should an organization desire a material with a certain set of physically possible properties, they could simply consult the formula and determine the manufacturing parameters needed to achieve them.

Table 29: First-order central difference results from sensitivity analysis, normalized about the base value shown.

Varied Parameter	Base Value	Elastic Modulus (E_{norm})		Yield Stress ($f_{y,norm}$)	
		FCC	Random	FCC	Random
Base Yield Strength	262 MPa	0.000	0.000	0.004	0.002
Sphere Diameter	1.86 mm	-1.91	-1.08	-2.04	-0.75
Shell Thickness	0.083 mm	12.08	15.96	10.97	14.68
Weld Overlap	0.04 mm	10.31	0.56	10.97	2.77

4.4.2 Gasar Tests

While the code itself groups gasar and PCM foams as the same, they have been split in two within this results discussion. This section describes those simulations intended to model gasar steel foams, which includes one set of validation tests and one study of post-yield behavior.

4.4.2.1 Initial Validation

Table 30: Input parameters used in gasar initial validation simulations.

Simulation Input Parameters		Geometric Input Parameters	
Name	Value	Name	Value
run_part	'all'	n_voids	{ 38, 53, 32}
run_location	'local'	ab	0.5
timeout	2400	c	4.0
name	{}	abstddev	0.1
geom_type	'Lotus'	cstddev	0.5
domain	[0 5; 0 5; 0 5]	theta	0
nsteps_elastic	20	phi	0
nsteps_plastic	0	thetastddev	0
timestepping	'ATS'	phistddev	0
mesh_element_size	0.18	include_hemi_caps	true
applied_nstrain	[0 0 -0.004]	minimum_dist	0.2
applied_shear	0	void_placement	'urandom'
shear_direction	-	lane_init_radius	-
rand_seed	{}	lane_perturb_rad	-
base_emodulus	200000		
base_ystress	172		
base_poisson	0.3		
base_pmodulus	500		
base_kanvinde_alpha	2.6		

Performed on a machine with 16 GB RAM and two 6-core AMD Opteron 2427 processors running at 2.2 GHz each

Results for the gasar geometry were validated using experimental results published by

Ikeda, Aoki, and Nakajima (2007), as no gasar material was available to test. Three 304L stainless

steel gasar foams of 50%, 63%, and 70% relative density were used to validate the general closed cell simulation. For these simulations, a mean void transverse diameter of 1mm was assumed with a standard deviation of 0.1mm, and a mean void height of 4mm with a 0.5mm standard deviation. All voids were oriented deterministically parallel to the z-axis and the minimum void spacing was 0.2mm. These values were based upon rough measurements of published images (Ikeda, Aoki and Nakajima 2007). Different relative densities were achieved by varying the number of voids. As expected because of size effects, the simulation showed yield strengths below the experimentally-reported values, as shown in Table 31. However, all simulated yield strengths were consistently 11 to 14% below the experimental, suggesting that the simulation's yield values may be validated as accurate to within at least 15 percent.

Due to restrictions in available computing power, the maximum size model that could be simulated was only 3-4 void diameters in length on each side. However, accurate experimental results have been shown to require samples that are at least 6-8 void diameters in length on each side (Andrews, et al. 2001). They show a dramatic drop-off in effective macroscopic strength and stiffness beginning at an edge length of 3-4 void diameters. This is due to a combination of edge effects, where voids located along an edge will reduce the material's strength more than fully interior voids, and scale effects, where the size of the voids are large enough relative to the sample size that individual voids affect the effective material properties to a non-trivial degree. Therefore, assuming that the simulations are correctly representing the physics of the metal foam, the simulations should give lower strength values than those reported experimentally due to the difference in the size of the samples. Further, other errors may arise in that, while the original base metal is known, the amount by which its properties may have been altered during the foaming process is unknown.

Table 31: Gasar foam validation using gasar experimental values. Partially adapted from research by Ikeda, Aoki, and Nakajima (2007).

Relative Density	Experimental Yield Stress (MPa)	Simulation Yield Stress (MPa)
50%	90	80
63%	115	99
70%	130	109

4.4.2.2 Post-Yield Behavior Simulation Matrix

Table 32: Input parameters used in the gasar post-yield behavior simulation matrix.

Simulation Input Parameters		Geometric Input Parameters	
Name	Value	Name	Value
run_part	'all'	n_voids	{ 3 - 41 }
		<i>(variable was adjusted to result in relative densities of 80%, 90%, and 95%)</i>	
run_location	'local'	ab	{ 1.0, 1.5, 2.0 }
timeout	2400	c	{ 2 - 8 }
		<i>(variable was adjusted to result in elongation ratios, c : ab, of 2:1, 3:1, and 4:1)</i>	
name	{}	abstddev	0
geom_type	'Lotus'	cstddev	0
domain	[0 10; 0 10; 0 10]	theta	0
nsteps_elastic	20	phi	0
nsteps_plastic	0	thetastddev	0
timestepping	'ATS'	phistddev	0
mesh_element_size	{ 0.42 - 0.5 }	include_hemi_caps	true
applied_nstrain	[0 0 -0.004]	minimum_dist	0.2
applied_shear	0	void_placement	'urandom'
shear_direction	-	lane_init_radius	-
rand_seed	{}	lane_perturb_rad	-
base_emodulus	200000		
base_ystress	172		
base_poisson	0.3		
base_pmodulus	500		
base_kanvinde_alpha	2.6		

Performed on a machine with 16 GB RAM and two 6-core AMD Opteron 2427 processors running at 2.2 GHz each

Similar to the simulation matrix performed for hollow spheres foams (see section 4.4.1.3 Post-Yield Behavior Simulation Matrix), a set of simulations was performed to determine the post-yield behavior of gasar foams. In addition to the relative densities varying from 80% to 95%, the ratio of void height to transverse diameter was also varied from 2:1 to 4:1, which are plausible ranges for producible gasar foams. All voids were oriented deterministically parallel to the z-axis, which is approximately accurate, and all input variables were set to be deterministic. All simulations were performed with cubic specimens approximately 5 mm to a side. An

example of a typical geometry generated in this simulation matrix is shown in Figure 64. Figure 65 shows sample output graphs from one run at 80% relative density, 2:1 elongation ratio, and 1.5mm transverse void diameter.

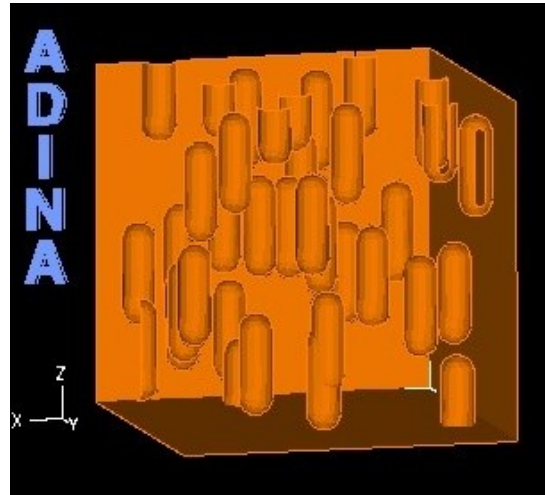


Figure 64: Image of a typical geometry generated during the post-yield behavior simulation matrix.

Among the most important material variables, both the yield stress and the elastic modulus were observed to increase as the voids were elongated, as shown in Figure 66. For a fixed relative density of 80%, the simulations show that the elastic modulus is approximately 4% larger and the yield stress is approximately 8% larger at a 4:1 ratio compared to a 2:1 ratio. Note that while this is a strong advantage for gasar foams, the foams are anisotropic and it is expected that their strength and stiffness will be lower when force is applied perpendicular to the voids' orientation. This phenomenon may be explained by the elongated pores providing a more straight and direct stress path through the material as well as providing less opportunity for bending behavior within the material compared to non-elongated pores. In contrast, the long, relatively flat walls of the voids in the transverse direction would provide long beam-like structures which may be highly susceptible to bending.

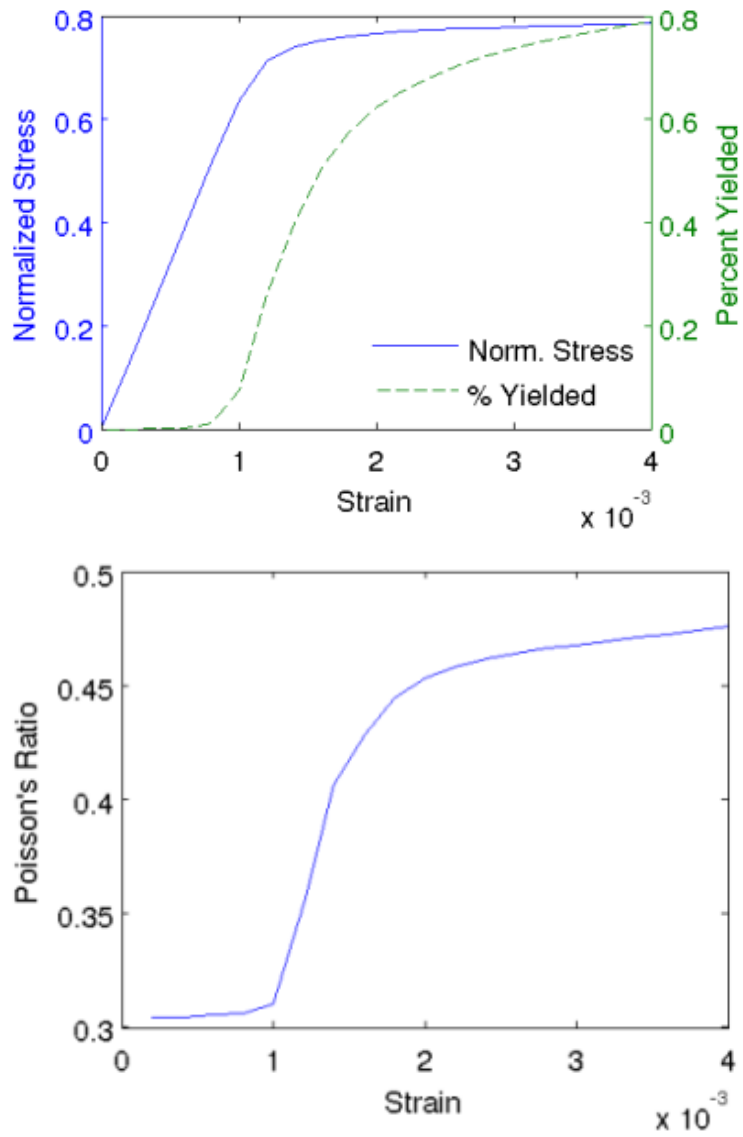


Figure 65: Sample output graphs from gasar simulation matrix: normalized stress and percent of material yielded vs strain (left); incremental Poisson's Ratio vs strain (right). Note: Stress is normalized to the yield stress of the base metal, 304L stainless steel.

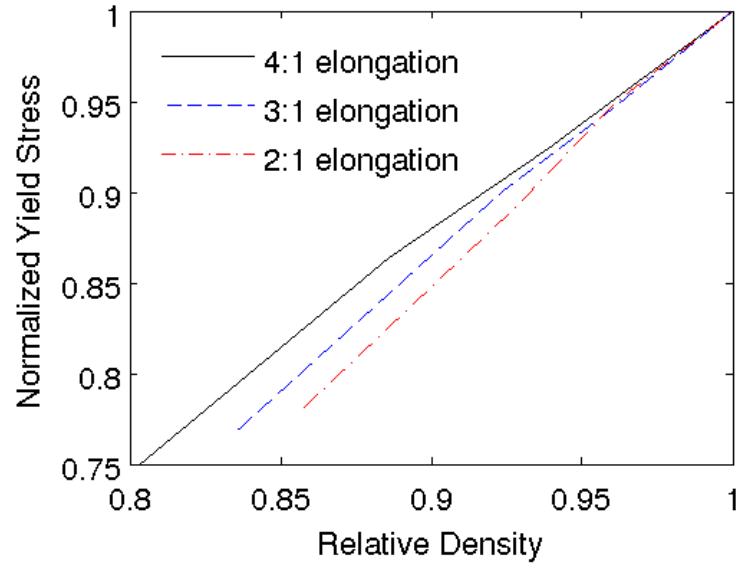


Figure 66: Yield stress vs relative density, showing increased yield stress with greater void elongation. A similar pattern may be seen for elastic modulus.

As the relative density of the gasar foams is decreased, the elastic Poisson's ratio increases slightly, from 0.3 to about 0.32, and the plastic Poisson's ratio, measured at the time step immediately after the yield point, decreases from 0.5 to about 0.42, as shown in Figure 67. Further, the amount of strain required to fully transition from elastic to plastic plateaus increases. The decrease in the plastic Poisson's ratio may be attributed to the material's voids collapsing and the material's volume crushing. The longer transition period is demonstrated by the graph of the percentage of the material yielded, which increases more slowly with lower relative densities. As less of the material is actually yielded at the apparent macroscopic yield point, the Poisson's ratio is also more elastic-like at such lower densities. The effect of elongating the cylinders is less apparent, but the transition period between elastic and plastic Poisson's ratio becomes slightly sharper and the plastic Poisson's ratio becomes slightly larger.

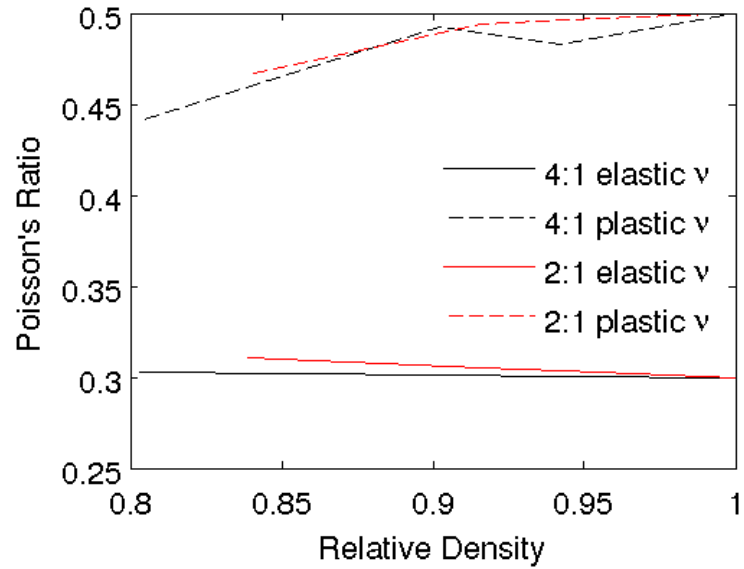


Figure 67: Poisson's Ratio versus relative density, showing an increasing plastic Poisson's Ratio and decreasing elastic Poisson's Ratio as the relative density increases.

4.4.3 PCM Tests

As experimental PCM material was only acquired in the last two months of this research, only one set of simulations was performed for PCM foams, and these were tests only to validate the simulations against the PCM foam.

4.4.3.1 Validation to Experimental Results

Table 33: Input parameters used in the PCM validations to experimental results.

Simulation Input Parameters		Geometric Input Parameters	
Name	Value	Name	Value
run_part	'all'	n_voids	15
run_location	'local'	ab	0.35
timeout	9600	c	5.1
name	{}	abstddev	0.06
geom_type	'Lotus'	cstddev	0.22
domain	[0 2; 0 2; 0 2]	theta	0
nsteps_elastic	20	phi	0
nsteps_plastic	10	thetastddev	0
timestepping	'ATS'	phistddev	0
mesh_element_size	0.03	include_hemi_caps	true
applied_nstrain	[0 0 -0.1]	minimum_dist	0
applied_shear	0	void_placement	'urandom'
shear_direction	-	lane_init_radius	-
rand_seed	{}	lane_perturb_rad	-
base_emedulus	200000		
base_ystress	1050		
base_poisson	0.3		
base_pmodulus	5000		
base_kanvinde_alpha	2.6		

Performed on a machine with 76 GB RAM and four 6-core Intel Xeon E5645 processors running at 2.4 GHz each

All geometric input parameters for the PCM validation simulations were based upon microscopy measurements (see section 3.3.1.2 PCM Foam). Weight and volume measurements were used to determine the relative density of 34%. No microporosity was assumed, as microscopy images were inconclusive as to whether microporosity is present. MER Corporation never stated the type of steel used in the manufacturing, so the base yield stress was completely unknown. In these simulations, the base yield stress was determined by means of calibrating the simulation's resultant yield stress to be equal to the experimentally measured yield stress. Doing so suggested that the base metal yield stress should be roughly 1150 MPa.

Experimental characteristics were evaluated in two steps: one test for elastic modulus, and one for yield stress. Plotting both along with the simulation results has little meaning, so a comparison of scalar values is shown in Table 34.

Table 34: Comparison of elastic modulus and yield stress values for PCM validation simulations.

	Elastic Modulus (MPa)	Yield Stress (MPa)
Simulation	68,000	395
Experimental	59,000	349

Key Section Findings

Hollow spheres, gasar, and PCM steel foams are validated to be accurate within 10-20% of experimental results.

The gasar post-yield simulation matrix shows that increasing the void elongation also increases the yield stress of the macroscopic material. The hollow spheres simulations show a rapid transition between Poisson’s ratio behaviors at approximately 15-20% relative density.

The use or absence of a random structure in hollow spheres foam is shown to result in a difference in elastic modulus of over 50%, largely due to the loss of welds as the structure becomes increasingly random, reinforcing the importance of utilizing a random geometry in simulations.

A sensitivity analysis study for hollow spheres foams shows that simulations may be used to develop formulae that predict the behavior of steel foams and could allow designers to determine necessary manufacturing parameters in order to achieve a set of desired material properties.

CHAPTER 5 SUGGESTED FUTURE WORK

5.1 Introduction

This thesis describes recent experimental and computational research to measure the compressive, tensile and shear properties of steel foam. More work is required, however, to encourage the structural engineering industry to begin using steel foam as a viable material in construction. This additional work includes both material research to better understand the mechanical, thermal, and other properties of the steel foam material, as well as applications research such as prototyping and demonstration projects to prove the real-world value of steel foam. The two pursuits must go hand-in-hand, but as this thesis has focused upon the former, suggestions will likewise focus on the same.

This research has proven computational simulations to be a viable and cheaper alternative to repeated experimental testing. However, simulations must still be calibrated and proven experimentally, so further work in both is necessary. A prioritized list of recommended future work which could be done immediately in a follow-up project is shown in Table 35. A more general prioritized list of recommended longer-term tasks is shown in Table 36. Detailed descriptions of each task and the necessary associated work are discussed in the following text.

Table 35: Prioritized list of recommended work which could be immediately performed as a follow-up project to this thesis

Priority	Task Description	Reason for Priority
1	Experimental connection testing – perform tests to simulate connections by wood screws, bolts, or other methods	Components need to be attached somehow
2	Simulation validation to shear tests	Code's there and tests are done
3	Simulation sensitivity analysis for gasar foams	Gasar is the most promising foam
4	Development of new testing standards – especially following up on tension test standard development	This will be essential for encouraging industry to use foam
5	Experimental thermal testing – even if just with a simple controlled heat source and thermometer	It is one of the best selling points that the material has multiple uses
6	Experimental cyclic testing – high-cycle testing	This is important for sandwich panels
7	Experimental strain rate testing	Impact energy absorption uses
8	Add new features to simulation code – strain rate, thermal, and/or densification, as technical feasibility permits	Simulating tests that will have been done is important
9	As many simulation sensitivity analyses as possible	They're what designers will use

Table 36: Prioritized list of longer-term tasks for encouraging industry to begin using steel foams.

Priority	Task Description	Reason for Priority
1	Testing other steel foams – especially gasar foams	They are the most promising foams for structural applications
2	Experimental connection testing	Components need to be attached somehow
3	Simulation validations	They are the lifeblood for proving the viability of simulations that don't need calibration
4	Simulation sensitivity analyses for gasar foams	Gasar is the most promising foam
5	Development of new testing standards	This will be essential for encouraging industry to use foam
6	Experimental thermal and other non-mechanical testing	It is one of the best selling points that the material has multiple uses
7	Experimental cyclic testing – low-cycle fatigue	Energy absorption applications, such as earthquakes, need this
8	Experimental strain rate testing	Impact and blast applications
9	As many simulation sensitivity analyses as possible	They're what designers will use
10	Add densification testing feature to simulation code	It's essential for energy absorption
11	Add strain rate testing feature to simulation code	Impact and blast absorption uses
12	Add thermal testing feature to simulation code	Multiple uses of steel foams
13	Experimental cyclic testing – high-cycle fatigue	Bridge and sandwich panel uses
14	Experimental creep testing	Less essential, but should be tested
15	Experimental multi-axial testing	Difficult, but potentially important
16	Add other features to simulation code – connections, cyclic, creep, torsional shear, other non-mechanical simulations	Less important, but they would be useful bonus items to simulate

5.2 Experimental

Key Section Objectives

Describe possibilities for future experimental work in this research project.

Suggested experimental work includes developing new testing standards, performing more types of tests, and testing different types of steel foams.

5.2.1 Develop New Testing Standards for Metal Foams

Thus far, only one testing standard has been created for metal foams: ISO/DIS 13314, for uniaxial compression testing. As shown by previous research in the field, methods of performing tests and data to report were rather arbitrary before the completion of this standard; it was rare for even properties such as elastic modulus to be reported (see section 2.2.1 Experimental Material Properties). Further, industry will want to be certain that numbers they see from different tests and different foams are comparable, and that the testing procedures have been stringently reviewed.

According to Dr. Ulrich Krupp at the University of Applied Sciences in Osnabrück, Germany, there is an active committee attempting to develop a tensile testing standard for metal foams (U. Krupp 2011). Future research should follow up upon this attempt, continue to encourage the committee, and provide further suggestions.

Tension tests are the most important next step, but further committees should also be assisted or assembled to develop testing standards for shear, multiaxial, and connection testing as well. Further testing, however, may well be required before such standards can be developed, as the shear testing performed as part of this thesis is the first shear testing of any steel foam known by the author to have been performed thus far. Further literature review should be completed to look for such tests that may have been performed upon metal foams other than steel.

5.2.2 More Testing Types

The research in this thesis has only involved compression, tension, and shear testing. While hollow spheres metal foams have thus far proven to be unlikely candidates for many structural applications, roughly forty-five more 52mm x 55mm x 250mm samples are available for testing at the University of Massachusetts. At the very least, further testing of hollow spheres foams can provide a template for methods by which to test other types of steel foams. To that end, connection, strain rate, thermal, and other testing are suggested.

5.2.2.1 Connection Testing

No matter how steel foam is used in applications, it will need to be attached to other materials, giving connection testing particular importance. Previous experience in testing has provided some guidance as to connections which might be possible for hollow spheres steel foams. For example, welding of the available hollow spheres foam was attempted by the University of Massachusetts Mechanical Engineering Department Machine Shop staff, but proved impossible with known techniques. Rather than weld, the steel foam simply melted under standard steel welding methods, despite attempting multiple types of welding, ruling out this type of connection as at least immediately most practical. See Figure 68 for an image of possible methods of connecting metal foams.

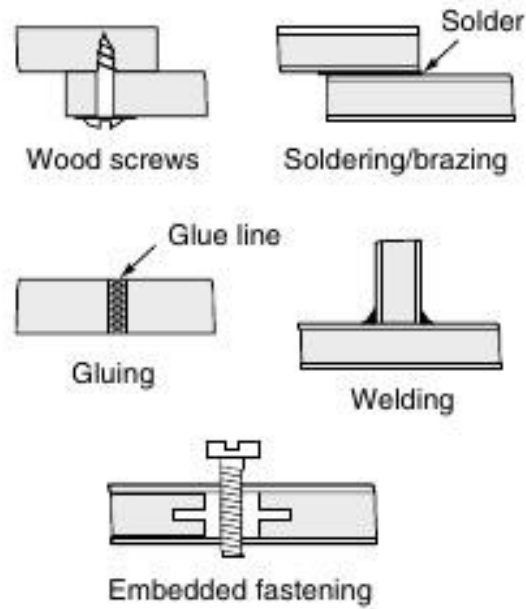


Figure 68: Image of possible methods of joining metal foams, as diagrammed in (Ashby, et al. 2000)

Further, uniaxial testing has shown that the material is actually stronger in shear than in tension, and even the cheapest solid steel bolts will be stronger in all failure modes than the steel foam. This suggests that bolted connections can be assumed to fail in a net tensile fracture mode. Some connection of bolted connections may be valuable to confirm this assumption, but this need only be minimal testing. Further, machining holes in the hollow spheres foam may not be possible.

Wood screws or other self-tapping screws, however, may prove to be a promising method of connection, as the material is heterogeneous and on the same order of strength as timber products. Such connections might look very similar to wood connections, and so such standards should be referenced in the testing of these connections.

Another valuable type of connection testing is that based upon epoxy. A finger joint connection, such as that which was actually used for tension tests, should be the first priority in this testing. The tension test procedure (see section 3.2.3 Tension Testing) has already been

proven. However, instead of having a reduced cross-section in the center of the specimen, it could be left as a straight rectangle, and the point at which the connection fails could be measured. Such a test should also be repeated with the end regions both confined and unconfined. In the unconfined mode, it may be expected that the specimen will fail partially in tension, with the foam opening up near the end regions, as was seen in an early experimental test (see Figure 69). In the confined mode, which would be roughly equivalent to having "multiple fingers", the specimen should fail in a purely shear mode.

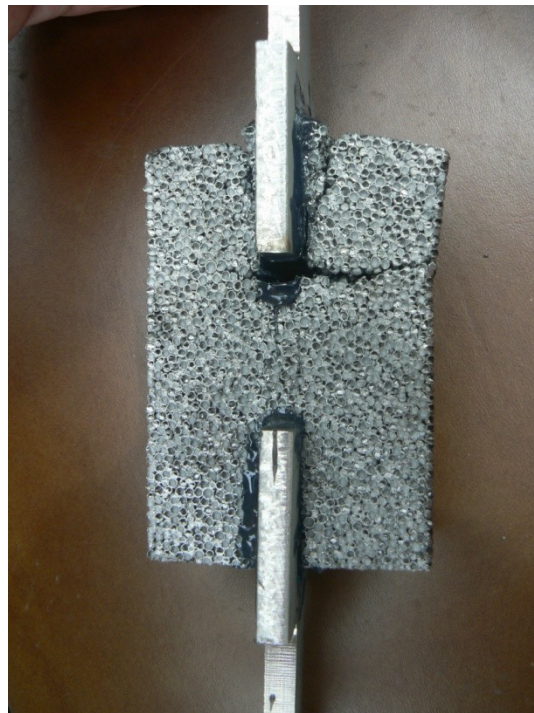


Figure 69: Image of an early experimental test, which should be equivalent to an unconfined connection test of a "single finger" joint.

5.2.2.2 Cyclic Testing

Hydraulic testing machines are capable of simulating many repeated cycles of loading. As the hollow spheres foam has shown itself to yield at nearly the same strength in compression as in tension, high-cyclic testing may be of value to simulate service loads in a structure such as a sandwich panel. The tension specimen, as described in section 3.2.3 Tension Testing, has both

tensile and compressive capacity, so it could be directly used in such testing. The only thing to make sure of would be that the epoxy used has sufficient cyclic load capacity so that it doesn't fail first.

Steel foams in general have very strong potential in earthquake energy absorption and other applications involving repeated plastic deformation. Hollow spheres foams, however, have very minimal inelastic capacity in tension, meaning that any low-cycle fatigue applications for hollow spheres must be in compression-only applications. Unidirectional low-cycle fatigue, while of some value, should be placed at a much lower priority, as testing such as strain rate testing (see next section) should provide much more valuable results. If other types of steel foams which have more tensile ductility are acquired, then bidirectional low-cycle fatigue should be considered a very high priority. In such a case, the tests would be very relevant to potential applications.

In contrast, high-cycle fatigue remains within the elastic range, and would be relevant to applications such as sandwich panels in roof, floor, or wall components. These are applications for which hollow spheres foams are potentially well suited. The available hollow spheres foam has a fairly uniform yield stress in tension and compression, so such high-cycle fatigue tests could be symmetric and provide very high value.

5.2.2.3 Strain Rate Testing

A promising application for steel foam, and particularly for lower-capacity foams such as hollow spheres, may be explosive energy absorption. Previous researchers have performed some limited testing in these regards (Cardoso and Oliveira 2010), (Park and Nutt 2002), but not upon sintered hollow spheres foams. Such testing would require the use of a high-speed hydraulic testing machine or split Hopkinson bar test machine to achieve strain rates necessary

for dynamic effects. However, existent compression platens designs could be used, and the same procedure as previous compression tests without the extensometer could be reused (see section 3.2.2 Compression Testing). This would be essentially following ISO/DIS 13314 but with higher strain rates.

5.2.2.4 Creep Testing

Several potential applications for steel foam involve its use as structural panels of various forms. If it is to be used in long-term service positions such as these, where there would be permanent dead loads, then understanding the creep behavior of steel foam is essential. While tensile creep may also prove important, documenting compressive creep is more imminently important. For this, ISO 7850 ("Cellular Plastics, Rigid - Determination of Compressive Creep") may prove a good template. The standard is not highly detailed, but suggests dimensions (50mm x 50mm x 40mm) which are very reasonable for the available hollow spheres steel foam, and testing conditions such as long-term sustained stresses, which should be possible with available equipment. However, since solid steel experiences only minimal creep, preliminary tests may show this to be a negligible characteristic.

5.2.2.5 Multiaxial Testing

True triaxial testing requires capacities not commonly available in multiaxial testing machines. However, a confined compression test may be more easily possible, and deserves further investigation. It is possible that using some type of fiber wrap, such as that used in reinforcing concrete, may provide effective confinement while still allowing longitudinal strain. Such a possibility deserves investigation, as applications such as earthquake fuses are likely to be confined and this would certainly provide higher strength capacity for the material. The previously-used compression procedures could be re-used in this test (see section 3.2.2

Compression Testing), just adding confinement to the specimen and using a cylindrical shape to the specimen.

5.2.2.6 Non-Mechanical Testing

Among the most unique and marketable characteristics of steel foam are the various non-mechanical advantages that it gives. Steel foam will probably always be more expensive than solid steel due to its difficulty of manufacture. However, if designers could combine sound absorption, thermal insulation, and vibration isolation into one structural component, that may be economically viable. Few experiments have been performed to evaluate these properties. Vibration and sound absorption would likely require specialized equipment. Regardless, thermal insulation could be measured non-destructively with simply a controlled heat source on one end of a sample and an accurate thermometer on the other. Research should first be performed upon available testing standards for non-mechanical properties in order to determine appropriate procedures.

5.2.3 Testing Different Steel Foams

Two different steel foams have been tested over the course of this research, though each is extreme in its mechanical properties. The hollow spheres foam, having an ultimate stress of less than 6 MPa in tension and shear, are too weak to use in most structural applications. The PCM foam then is as strong as many solid steels, but is very brittle and therefore exhibits few of the energy absorption advantages that would make the added cost of steel foam worthwhile. It was not possible to acquire other types of steel foam during this research thus far, but further attempts should be made.

MER Corporation in Tucson, Arizona may provide a good option through their methods of manufacturing gasar foams. Based upon previous research involving gasar foams (Hyun, et al.

2005), (Shapovalov and Boyko 2001), gasar foams seem to provide a good intermediary strength and can be manufactured in continuous processes. Therefore, gasar foams have potential strong promise in commercial structural applications.

Other potentially useful types of steel foam include powder metallurgy, composite hollow spheres and powder metallurgy, or slip reaction foam sintering. The last has been the research of only Aachen University in Switzerland, so while it provides great advantages in that it can be foamed at room temperature, the method may be too far from commercial development at this point (Angel, Bleck and Scholz 2004). The composite hollow spheres and powder metallurgy option is being extensively researched at North Carolina State University under the direction of Dr. Rabiei. This method can only be produced in a long batch process, and so may be undesirable (Rabiei and Vendra 2009). Powder metallurgy is a well-proven method, a variant of which is already used in the commercial manufacture of solid steels with unique crystal structures. The method is also capable of producing steel foams in potentially advantageous relative densities (Park and Nutt 2000). Therefore, while it is a batch production method, it is probably the best option for structural engineering applications after gasar foams.

Key Section Findings

The most valuable future experimental work in this project includes helping to develop new testing standards, performing further types of testing, and evaluating steel foams produced by other manufacturing methods.

5.3 Computational

Key Section Objectives

Identify new features that should be added to the simulation code, including briefly explaining the changes that will be necessary to implement those new features.

Discuss further simulations which should be performed using the Metal Foams Simulator.

The development of the Metal Foams Simulator has been a core focus of this thesis, and it has reached a highly developed state. However, there is certainly more which could and should be added or refined. The core of the code is fully functional, so it is unlikely that any changes will require a major re-structuring of the code. The only potential very major change would be if ADINA proves to be too limited in functionality, and switching to another FEA program becomes desirable.

There are always potential efficiency improvements. Some, such as parallelizing the geometry generation code, would be helpful but also overly time-consuming to implement, particularly since the geometry generation code has required the most continuous refinements throughout this project. Others, such as fine-tuning the mesh element size, make a big difference but are of necessity a continuous and unending optimization process.

One area that should be optimized is the post-processing code, which currently is slow to extract its data and convert it to a format more usable by MatLab, and grows exponentially slower on larger simulations. Several improvements have already been made to this code, but there is still definite room for improvement. For example, parallelizing the reading and parsing of ADINA's .txt output files would be extremely valuable, as this is the slowest point in post-processing and currently only uses one processor. The best method of accomplishing this task would likely be to first split the .txt files into multiple smaller files, and then launch independent `sed` processes upon each of these smaller files simultaneously. There are also a couple of loops in this post-processing code which could be edited to be run in parallel.

5.3.1 New Features

Potential new features to the code generally involve adding new testing types. Features should be added to allow the simulation of any tests that may be performed experimentally, as

well as some that may not be possible to perform experimentally. One of the greatest advantages of computational simulations is that they allow for simulations that are either impossible or cost-prohibitive to perform experimentally. In descending order of likely value, these potential new simulated tests could include densification, connection, strain rate, thermal, cyclic, creep, torsional shear, and then other non-mechanical tests.

5.3.1.1 Densification Tests

In all compression tests, or even in shear tests, contact between the walls of voids strongly affects the behavior of the material. However, in finite element packages, implementing contact physics is a very difficult problem, and one which has not yet been addressed in the simulation code. In ADINA, which requires the internal ID numbers of potential contact surface pairs to be specified in order to activate its contact code, there may not be a practical solution to implementing this. There is no way to either predict or extract what ID number will be assigned to any given surface in the ADINA geometry. It is possible that some future version of ADINA may provide a solution, but the nature of such a solution cannot be predicted.

The other option is the more daunting task of converting the code to use a different finite element package which may provide a better solution to contact physics. Converting the code would require changes to all functions which write ADINA script, as every finite element package uses its own script language. Further, any functions which parse ADINA output would also require some modification to read data from files of a different format.

5.3.1.2 Strain Rate Testing

Strain rate simulations require considering dynamic effects in the physics of the materials. Currently, simulations apply displacements progressively, but the physics are pseudo-

static. Adding dynamic effects in ADINA is only a checkbox in the analysis options, which would need to be enabled, though it is unclear whether this would provide a sufficiently accurate analysis. Additionally, the mass of the materials involved would have to be set accurately. Since it has no effect upon pseudo-static analyses, the mass of the material was never actually set in the current code. The biggest change in the code would involve minor reworking of the timestep setting in ADINA. In the current code, timestepping is always based on a total time of 1, and then divided into the number of desired steps. The total time would have to be adjusted to set the desired speed of displacement application correctly.

5.3.1.3 Thermal Testing

Thermal testing is a non-mechanical test that does not involve force stresses or strains, so it would require some significant modification to post-processing code in addition to boundary conditions and loading profiles. It may also require detailed modeling of air flow and convection. Much of this would likely be implemented through if/then statements at the beginning of boundary condition setting and then again at the beginning of post-processing, where the existing code would be set to execute for everything except thermal tests, and then some new code only for thermal tests would be executed as the other option.

5.3.1.4 Connection Testing

Connection testing would require some important changes to the code, but no extensive reworking of the code. Any connection, whether bolted, screwed, welded, or epoxied would involve the use of some amount of a different material. Therefore, a second material definition would need to be created early in the input file. The geometry of that connection would have to be created, though this should be placed after the entire steel foam geometry generation has been completed. At that point, a bolt hole could be created by boolean

subtraction of a cylinder, for example, or the shape of a weld could be created. Any weld or epoxy would require simulating a rigid link between the steel foam and the connection material, the most effective method of which would be to use the "glue mesh" functionality of ADINA. This functionality enforces nodal compatibility between two surfaces, and the ID numbers of bodies should be known within the code, so this should be possible to use. The greatest restriction in connection simulations would likely be model size, as many connections would require a large volume of material in order to provide useful strength. Larger volumes of steel foam require significantly more memory and processing power, likely rendering some connections prohibitive to simulate in the absence of a supercomputer.

5.3.1.5 Cyclic Testing

ADINA provides two mechanisms which could allow for cyclic simulations, and it is difficult to predict which would prove the superior method. The first method involves running each part of the cycle as a separate simulation and setting new loading profiles each time the simulation restarts. The second method would be for ADINA to apply the entire cyclic pattern internally, though postprocessing would be highly complex. The decision as to which method is superior would be based upon going through both procedures manually and determining how much time difference there would be between the two, and looking at the automatically generated ADINA script files to determine complexity and ability to implement through the simulation code.

Running each part of the cycle separately would likely be simpler to implement in the code, but would probably require more computational time to perform. Within the code, it would require implementing a simple loop starting in the load application section of the pre-processing, and ending at the point where post-processing data is stored to the MatLab results

file. Then, a new function would have to be written to store and pass on the data about what loads should be applied at which step of the cycling, and then to compile the results data from all previous steps of the cycling into usable form. The data storage and passing section would be able to use the same variables that are currently used to drive the simulation; it would only issue a new set of these variables at each step of the cycle, though it would skip the geometry generation and meshing portions of the code as that only needs to be done once. However, ADINA would also need to save the data on current strains at all nodes and then re-apply those at each restart. Data compilation would involve calculating both net and cumulative (sum of absolute values) of stress and strain values. Therefore, results files for cyclic simulations would have to be extended to contain a few more variables than other tests in order to include both types of results. However, while this coding work would likely be simpler, the simulation would likely require more computational time than if the entire cyclic loading were applied through ADINA.

The second method for implementing cyclic testing would be to set ADINA to perform the entire cyclic loading in one simulation. In this, ADINA would internally be calculating both the net and cumulative stresses and strains, and the postprocessing code would have to be extended to extract all of these results. Code changes would include adding a cyclic load profile and then applying that to nodes, possibly requiring a user-defined function to be written in ADINA's FORTRAN code language.

Note that, in both methods, a particular difficulty would be in tensile cycles where local material failure occurs. In the first method, failure thresholds would either need to be assumed to uniformly decrease as the number of cycles increases, or some method of tracking and then passing back to ADINA the cumulative stresses on elements would have to be found for the element deletion mechanism to properly function. In the second method, the only way for the

element deletion function to operate would be for ADINA to internally track cumulative stresses and make these values accessible to the element deletion function. Either way, properly dealing with this problem may be impossible.

5.3.1.6 Creep Testing

ADINA offers material models and analyses specifically designed to simulate creep physics. The simulations would involve replacing the current elastic material model with a creep model, and then applying loads as forces rather than displacements. The only required change to post-processing would be that stress vs strain curves would become no longer useful, and should instead be replaced by time vs strain graphs. The different types of stresses, such as bending stresses, involved in the macroscopic compression or tension of steel foams may well lead to very different creep behaviors than found in solid steel. Solid steel only experiences creep at high temperatures, so a microstructural simulation would only represent creep when the solid steel has exceeded its activation energy. Such a simulation would have value, particularly in applications where the steel foam was being used as a thermal insulator or where fire ratings were important. However, it would not represent any low-temperature creep, which may occur but would require new constitutive modeling instead.

5.3.1.7 Torsional Shear Testing

The torsional shear test, as specified by ASTM E143, will be much more complicated to implement as it requires multiple changes to the geometry and load application algorithms, as well as very awkward manipulation of ADINA. First, the geometry must be cylindrical. In the hollow spheres simulations, the algorithm currently generates the sphere stacking and then intersects a rectangular prism shape with it to create the cut sphere walls. This rectangular prism shape would need to be switched to a cylinder instead. The original sphere stacking could

still be performed in a rectangular prism shape. For the general closed-cell simulations, voids are currently placed randomly within a rectangular prism domain and then subtracted from a solid body that filled that same domain. The most important change would be to set the solid material to be a cylinder instead of the prism. Though not necessary, the voids could also be set to only be placed within that cylindrical domain; if left unchanged, then the voids outside the cylinder would just be subtracting empty space from empty space and so would do no harm.

The loading and boundary conditions would then need to be changed. The boundary conditions would be simple in that the base of the cylinder could be completely fixed, rather than fixing primarily only the one direction perpendicular to the face as is done in the uniaxial tests. The loading, on the other hand, would need to be applied so as to provide pure torsion. This would require writing an entirely new algorithm for load application, as the load vector would have to be based upon an auxiliary node located at the center of the circle. All applied displacement loads would have to be perpendicular to a radius emanating from this point, with a magnitude proportional to their distance from this point. This requires modifying the mechanism used to specify loads in the code.

Finally, postprocessing would require significant modification. Stress and strain would have to be based upon the auxiliary point center of the cylinder's cross-section as the load application. However, ADINA does not have a simple way to use an auxiliary point in the exporting of reaction and displacement data. Therefore, significant calculations will be necessary in MatLab, including determining effective stress and strain vectors at the faces of the material. This will require more data to be exported by ADINA as well as significantly more processing of the data once imported into MatLab.

5.3.1.8 Other Non-Mechanical Testing

ADINA only has built-in material and computational models for thermal analyses. However, computational analyses of vibration transmission and sound absorption would also be potentially valuable, as steel foams do exhibit advantageous characteristics in these areas. Elastic material models with high-speed dynamic load applications could potentially accomplish some of this, but other finite element packages may also provide simpler methods of performing such simulations. The precise nature of changes necessary for these other non-mechanical simulations cannot be predicted, but it would be worth investigating how possible their implementation might be.

5.3.2 Geometry Improvements

Some improvements that may possibly be proven necessary for accuracy are described in this section. The current code, out of necessity, makes numerous simplifying assumptions (see section 4.3.4 Summary of Assumptions), mostly relating to the geometry of the material, and it may turn out that one or more of these simplifications cause excessive error.

One possible inaccuracy is in the general closed-cell simulations, which represent a void by a cylinder with optional hemispherical caps. In real gasar foams, the main bodies of these voids have a relatively constant diameter, but the voids come to a sharper point on either end. If these sharper points prove to cause large stress concentrations, then the hemispherical caps will have to be changed. The void is currently generated by subtracting one cylinder body and two sphere bodies from the simulated block. Another, more representative body will have to be used, or perhaps developed through the rotation of a two-dimensional sketch.

Another inaccuracy in the general closed-cell simulation is that the orientation of the voids in a fabricated gasar piece varies geometrically, becoming less aligned with the direction

of foaming nearer to the edges of the material. Currently, the simulation code has the capability to vary the orientation of voids, but it can only do so in a random fashion. There is no mechanism in the code to vary any material characteristics based upon geometric location, excepting a simple algorithm for preventing the overlap of voids, though this could be changed.

Inaccuracies are also present in the hollow spheres simulation, one of the greatest of which is that sphere walls are currently assumed to be of uniform thickness within any given hollow sphere. It is likely that the sphere thickness is somewhat random and also generally thicker nearer to the welds. Representing this geometry with full accuracy is certainly impractical and would provide only minimal benefit, but greater accuracy may be necessary. By the current method of generating a sphere geometry, subtracting one sphere body from another larger sphere body, creating any surface roughness would be extremely difficult. However, a relatively simple improvement could be to set the sphere that is subtracted to be somewhat off-center from the larger sphere, thereby resulting in one side of the sphere wall being thicker than the other.

Many other improvements to the geometries are possible, and could prove to be valuable, though what might be necessary cannot be predicted. Examples are described above, and other changes might require either more or less coding effort.

5.3.3 Simulation Validation

Simulations are only as good as their correlation to experimental results. Therefore, a continuing task is to validate and calibrate the simulations to such experimental results. Unfortunately, few precise values are available in published literature. Of those that are available, some validation tests have already been performed, as described in section 4.4

Results. However, the best source for precise validation data is through the complete experimental data available from tests performed at the University of Massachusetts.

After further tests are performed experimentally, equivalent computational simulations should be performed. The biggest unavoidable sources of error in this task are currently a result of the limited computing power available and difficult boundary and loading conditions.

Computational simulations are performed on samples that are much smaller (volumetrically, 1/100 to 1/1000) than the sample being experimentally tested. Size effects, as discussed by Andrews et al (2001), result in the material appearing artificially weaker. However, even with errors such as this, results should be close. If they are not, then input parameters to the simulation can be tuned, and certain model geometry and meshing characteristics may be edited to increase accuracy and reconcile the differences.

Several important input parameters are not precisely known and may be tuned to achieve more accurate results. Generally, the relative density of a sample may be determined accurately, but the precise distribution of mass within the material is difficult to measure. In hollow spheres simulations, this is particularly apparent in the ratio between material in the welds versus in the sphere walls. To adjust this while keeping the relative density constant, one could increase either the diameter or the length of the welds, and then the thickness of the sphere walls, for example. In the general closed-cell simulations, the adjustment is primarily in the number versus the size of the voids, as well as in adjusting the shape of the voids (height versus diameter). Further, both types of simulation have several random variables. Increasing the standard deviation of the sphere wall thickness, weld diameter, void dimensions, or void orientations may also have an effect upon the simulation results. For example, just a few hollow spheres with thinner sphere walls may decrease the macroscopic elastic modulus, despite

holding the mean wall thickness constant. This effect would be due to those thinner spheres being significantly more compliant.

5.3.4 Simulation Test Matrices

Some test matrices have already been performed to determine specific aspects of the mechanical behavior of steel foam. Future test matrices should focus on determining further mechanical properties, such as shear or tensile responses, and if functional access is gained to a supercomputer, then some previous test matrices could be repeated with larger sample sizes. As new features are added and debugged, such as the ability to perform connection tests or creep tests (see section 5.3.1 New Features), then simulation matrices of these should also be performed.

The most promising steel foams are likely gasar foams (see section 5.2.3 Testing Different Steel Foams), so simulations should likewise focus upon gasar foams as much as possible. However, gasar foams are expected to exhibit different properties depending upon whether pores are oriented longitudinally or transversely to the direction of load application, and so simulations with both orientations should be performed to examine the difference.

Some steel foams, however, may show more promise for specific applications. For example, hollow spheres steel foams may be better for sandwich panels. Therefore, simulations of loading scenarios relevant to sandwich panels should be performed, such as shear simulations.

Finally, the long-term goal of the simulations is to allow fabricators to select geometric properties based upon desired mechanical properties, such as yield stress or elastic modulus. To this end, one simulation matrix has been performed demonstrating this capability in the form of a sensitivity analysis for hollow spheres steel foams (see section 4.4.1.5 Sensitivity Analysis for

Compression Tests). Further such sensitivity analyses should be performed for other types of steel foams and other types of loading regimes, such as uniaxial tension in gasar foams.

Key Section Findings

Further new testing types should be added to the simulations, including densification, connection, strain rate, and thermal tests. Further improvements should also be made as needed to the geometry generation in the code.

While simply more simulations are better, priority should be placed upon calibrating the code to further types of steel foam and the execution of more testing matrices including sensitivity analyses.

CHAPTER 6 CONCLUSIONS

While steel foam holds strong promise as a structural engineering material, the relationship between its microstructural characteristics and mechanical properties has remained poorly understood. This research has sought to rectify this problem through a regimen of experimental tests as well as the simulation of matrices of tests through a novel program capable of representing the random structure of multiple types of steel foams.

Experimental Tests

Experiments have tested the available 14% relative density hollow spheres foams and the 34% relative density PCM foam in both uniaxial compression and tension, attempting to follow relevant testing standards as closely as possible. Compression tests, both of full-size samples and of reduced specimens brought out to densification have been performed upon hollow spheres foams, while the PCM foam was tested to brittle failure with pores oriented both longitudinally and transversely. Tension coupons have demonstrated the tensile yield and ultimate strengths of both foams. In some of the first shear tests of any steel foam, the hollow spheres foam has also been tested to ultimate shear failure. Specific conclusions from experimental testing include:

- Previous experimental research has focused almost exclusively upon uniaxial compression testing.
- Hollow spheres foam:
 - The hollow spheres foam is a very effective energy absorber, having a densification strain of roughly 0.65 and an ultimate stress of 260 MPa.
 - Behavior up until yield is nearly identical in compression, tension, and shear, with a yield stress of roughly 3.5 MPa.
 - Tension and shear showed an ultimate stress of about 4.5 MPa.

- Poisson's ratio is highly variable, ranging from about 0 to 0.3 in a non-linear manner.
- PCM foam:
 - The PCM foam is essentially a lightweight solid steel replacement, though it is very brittle.
 - The pore orientation makes roughly a 10% difference in compressive strength, and a 40% difference in tensile strength.
 - In compression, the material yielded at a stress of between 350 and 410 MPa, and then failed in brittle fracture at close to 500 MPa.
 - In tension, no yield point was observed, but fracture occurred at between 100 and 160 MPa.

Computational Simulations

A computer program, the Metal Foams Simulator, has been developed which utilizes MatLab and the ADINA finite element analysis program to create two types of random steel foam geometries, hollow spheres or general closed-cell, apply loading and boundary conditions to the specimen, solve, and then perform postprocessing to extract effective macroscopic mechanical properties of the material. Specific conclusions from computational simulations include:

- Previous modeling attempts have proven imprecise, particularly when considering any large range of foam parameters.
- Metal Foams Simulator
 - Validation tests of hollow spheres, PCM, and gasar foams have shown accuracy to within 20% of experimental results, with increasing accuracy as simulation size was increased.

- A statistical analysis of the effects of a random microstructure upon simulation results showed that randomness may decrease the macroscopic stiffness of the material by up to 70% compared to deterministic simulations, demonstrating the value of including randomness in any simulations.
- Hollow spheres simulations accurately demonstrated a plastic hinging effect in a sudden transition between two different Poisson's ratio behaviors, further validating the simulations.
- Gasar simulations showed a strong effect of pore elongation upon the strength of the foam, suggesting that materials with elongated pores are likely to be advantageous in structural engineering applications, where strength is important.
- A sensitivity analysis of hollow spheres foams showed the potential of computer simulations to determine the manufacturing parameters necessary to produce a steel foam of arbitrary desired mechanical properties.

Overall Conclusions

Through this experimental and computational research, guided by the requirements of potential future structural applications, a greater understanding of the mechanical properties of steel foam has been reached and a new tool has been placed into the hands of researchers and manufacturers alike in the form of a simulator for random microstructures. Research must continue upon steel foams, and some suggestions have been provided to this end, but this research has brought the steel industry one step closer to being able to add a potentially valuable new structural material to its arsenal.

APPENDIX METAL FOAMS SIMULATOR USER GUIDE

A.1 Launching the Program

The Metal Foams Simulator is a MatLab program consisting of one .m file which has several dozen functions performing the various tasks of the program. However, it also depends upon extensive use of several external programs, including the ADINA FEA system and various UNIX programs. There are two methods by which the Metal Foams Simulator may be executed: either as a standalone program, or by passing its main function a series of parameters. The program is optionally capable of utilizing remote solvers, such as a supercomputer job queue. The details of launching the Metal Foams Simulator are described in full below.

A.1.1 System Requirements

The Metal Foams Simulator was originally designed and tested upon three modern Linux machines. Based upon this original design, there are three sets of system requirements with which the program is known to function properly, listed in Table 37. However, the Simulator should also run adequately on many other machines, so also listed in Table 37 are the systems upon which the programmer believes the Simulator should work, but makes no guarantees to that effect.

Table 37: System requirements for the Metal Foams Simulator.

Requirement	Known To Work On	Believed to Work On
Linux Operating System	CentOS 5.7 Red Hat Enterprise Linux 5.3 Debian Sid 2010-2012	Any sane operating system on which all of the below programs can run
MatLab	v7.11.0 (R2010b) v7.10.0 (R2010a) v7.8.0 (R2009a)	v7.0+
ADINA FEA	v8.5.4	v8.5.x v8.5+ with minor code debugging for changes in the ADINA scripting language
Sane SH shell	bash v3.2.25 or v4.2.20	SH, BaSH, or CSH (any versions)
GNU sed	v4.1.5 or v4.2.1	Any version
GNU grep	v2.5.1 or v2.10	Any version
GNU coreutils	v5.97 or v8.13	Any version ('rm' and 'cat' are required)
For remote solvers: SSH (Secure SHell)	OpenSSH v4.3p2 with OpenSSL v0.9.8e, or OpenSSH v5.9p1 with OpenSSL v1.0.0e	Any sane SSH system having both 'ssh' and 'scp' executables

In addition to the above stated requirements, it is recommended that the computer used have maximal RAM, CPU speed, and hard disk space consistent with intense engineering applications. The better the system, the faster the simulations will run, and the larger the simulations (more elements) that will be possible to run. However, please refer to MatLab and ADINA manuals for minimum and suggested system requirements.

A.1.2 Definition of Input Variables

Up to 38 input variables are required to run the Simulator, defining all aspects of the simulation, with a minimum of 4 input variables required for program execution. If pre-processing is to be performed, then an additional 31 variables are required for general closed-cell simulations, or an additional 34 variables are required for hollow spheres simulations. Table 38 lists all variables, explanations of what they do, the possible values they may take on, and when they are required. See section A.1.4 Parametric Execution for the meaning of the "Param. #" column. The basic geometric parameters are illustrated visually in Figure 70 and Figure 71 for hollow spheres and general closed-cell geometries, respectively. An example set of parameters for a hollow spheres simulation and for a general closed-cell simulation are included in Table 39.

Table 38: Input variables for the Metal Foam Simulator, including possible values and an explanation of their meaning.

Input Variable	Param. #	Possible Values	Explanation of Variable's Meaning
<i>The following input variables are required ALWAYS</i>			
run_part	1	'all', 'pre', 'pre+solve', 'solve', 'solve+post', 'post', 'post_graphs'	Specifies which parts of the simulation should be run. 'all' = pre processing, solving, and post processing; 'pre' = pre processing only; 'pre+solve' = pre processing and solving only; 'solve' = solving only; 'solve+post' = solving and post processing only; 'post' = post processing only; 'post_graphs' = (re)generate the results graphs from the ".mat" results file. Note that 'post_graphs' is run as part of any post processing, but is provided as a separate option should a user only wish to perform that part of the processing.
run_location	2	'local', [name of remote machine]	The location where the solver should be run, or where the results data should be retrieved from.
timeout	3	Non-zero positive integer	(unit: seconds) The amount of time external programs will be given to either write something to their log file or exit. After this idle time, the external program will be automatically killed with a 'kill -9' command, and the Simulator run will end with an error code.
name	4	Any valid string	The type of geometry which this simulation corresponds to. Note that there are actually only two options here; 'HS' and 'CompHS-low' are internally identical, as are 'Lotus', 'PM', and 'CompHS-high'. The additional values are provided only for the user's reference.
<i>The following input variables are required only if run_part='pre', run_part='pre+solve', or run_part='all'</i>			
geom_type	5	'HS', 'CompHS-low', 'Lotus', 'PM', 'CompHS-high'	The type of geometry which this simulation corresponds to. Note that there are actually only two options here; 'HS' and 'CompHS-low' are internally identical, as are 'Lotus', 'PM', and 'CompHS-high'. The additional values are provided only for the user's reference.
domain	6	3x2 matrix of real numbers	The extreme coordinates of the rectangular prism domain to be simulated, given in the form of $[x_{min} \ x_{max}; y_{min} \ y_{max}; z_{min} \ z_{max}]$.
nsteps_elastic	7	Non-negative integer	Minimum number of time steps to perform in the range of 0.0-0.01 strain magnitude.
nsteps_plastic	8	Non-negative integer	Minimum number of time steps to perform in the range of 0.01-applied_strain strain magnitude.
timestepping	9	'ATS', 'TLA-S', 'Manual'	The time stepping algorithm to use. 'ATS' and 'TLA-S' are both automatic methods in which ADINA will automatically try a smaller timestep if the current timestep fails to converge. In 'Manual', only exactly the number of timesteps specified in nsteps_elastic and nsteps_plastic will be run.
mesh_element_size	10	Non-negative real number	The length of the body geometry mesh elements to apply. A smaller number means a finer mesh.
applied_strain	11	Real number	The uniaxial strain to apply. Negative means compression, positive means tension. In ADINA, this is applied as a displacement on the top face of the specimen.
rand_seed	12	Non-negative integer	This is simply a random seed passed to Matlab. All other parameters being equal, two simulations with the same seed will give identical results.
plot_disp	13	true, false	Whether to display various plots of the geometry during pre-processing. Does not affect post-processing.
base_emodulus	14	Non-negative real number	The elastic modulus to use for the base metal in the simulation.
base_ystress	15	Non-negative real number	The yield stress to use for the base metal in the simulation.

Input Variable	Param. #	Possible Values	Explanation of Variable's Meaning
base_poisson	16	Real number between -0.5 & 0.5	Poisson's ratio to use for the base metal in the simulation.
base_pmodulus	17	Real number	The plastic (hardening) modulus to use for the base metal in the simulation.
base_kanvinde_alpha	18	Non-negative real number	The value of the Kanvinde and Deierlein alpha parameter for use in element deletion during tension simulations.
<i>The following input variables are required only if preprocessing AND geom_type='Lotus', geom_type='PM', or geom_type='CompHS-high'</i>			
n_voids	19	Non-negative integer	Number of voids to place in the geometry.
ab	20	Non-negative real number	Average axis length of the prolate or oblate ellipsoid along the circular dimension (i.e. the diameter)
c	21	Non-negative real number	Average axis length of the prolate or oblate ellipsoid along the long dimension (i.e. the height)
abstddev	22	Non-negative real number	Standard deviation of 'ab', as defined above. A normal distribution truncated at 0 is assumed.
cstddev	23	Non-negative real number	Standard deviation of 'c', as defined above. A normal distribution truncated at 0 is assumed.
theta	24	Real number between 0 and π	Average orientation of the 'c' axis in spherical coordinates (z elevation) (0 = vertical, $\pi/2$ = horizontal).
phi	25	Real number between 0 and 2π	Average orientation of the 'c' axis in spherical coordinates (x-y axis) (0 = projection parallel to the +x axis, $\pi/2$ = projection parallel to the +y axis).
thetastddev	26	Non-negative real number	Standard deviation of 'theta', as defined above. A beta distribution with a range of π is assumed.
phistddev	27	Non-negative real number	Standard deviation of 'phi', as defined above. A beta distribution with a range of π is assumed.
minimum_dist	28	-1, real number	The minimum distance (thickness of solid material) to enforce between voids. A value of -1 means to not enforce any minimum (allow voids to completely overlap).
<i>The following input variables are required only if preprocessing AND geom_type='HS' or geom_type='CompHS-low'</i>			
radius	19	Non-negative real number	Average outer radius of spheres.
radiusstddev	20	Non-negative real number	Standard deviation of 'radius', as defined above. A normal distribution truncated at 0 is assumed.
thickness	21	Non-negative real number	Average thickness of sphere walls.
thicknessstddev	22	Non-negative real number	Standard deviation of 'thickness', as defined above. A normal distribution truncated at 0 is assumed.
weld_type	23	'overlap', 'cylinder', 'matrix'	The type of weld to apply between spheres. 'overlap' means to overlap the walls of the spheres by 'weld_overlap'. 'cylinder' means to generate a cylinder of average radius 'weld_radius' between spheres that are less than 'weld_max_length' apart from each other. 'matrix' means to fill the entire space between spheres with solid material. (Only relevant if 'weld_type' = 'overlap') The maximum amount by which to overlap spheres. An overlap of 'thickness'/2 implies that sphere walls will be at most coincident between neighboring spheres. Note that due to a restriction in the algorithm used, the value given here is the target value, and is the maximum that will be possible, but the full value given may not be achieved in all connections (particularly for smaller domains).
weld_overlap	24	Non-negative real number	(Only relevant if 'weld_type' = 'cylinder') Maximum distance between sphere outer walls within which to create a connecting cylinder (i.e. assume that spheres farther apart than this are not connected).
weld_max_length	25	Non-negative real number	If 'weld_type' = 'cylinder': Average radius of connecting cylinders to generate between spheres. If 'weld_type' = 'overlap': The percentage of the radius over which two spheres are in contact within which a cylinder will be generated.
weld_radius	26	Non-negative real number	

Input Variable	Param. #	Possible Values	Explanation of Variable's Meaning
weld_radiusstddev	27	Non-negative real number	(Only relevant if 'weld_type' = 'cylinder') Standard deviation of 'weld_radius', as defined above. A normal distribution truncated at 0 is assumed.
wall_truncate	28	Non-negative real number	Amount by which to truncate the domain on all sides after having generated the full geometry. This is important to ensure that boundary conditions, loads, and results calculations include an adequate number of points. Without truncating, these would end up only including single points at the tips of the spheres.
mcm_iterations	29	Positive integer	Number of iterations to perform in the Modified Mechanical Contraction Method (MMCM) calculations for setting up the random geometry. More iterations are more accurate, but slower.
mcm_threshold	30	Real number between 0 and 1	Percent of spheres which are allowed to be overlapping before incrementing to the next iteration. A smaller percentage is more accurate, but slower and occasionally impossible to achieve.
mcm_init_placement	31	Non-negative real number (see explanation)	If 'mcm_init_lattice' = 'fcc': the spacing between the centers of neighboring spheres (= 'radius'*2 for tightly packed) If 'mcm_init_lattice' = 'urandom': number of spheres to place as an absolute number (if positive integer) or as a percentage of the number of spheres which would be in a simple cubic arrangement (if non-integer positive real number)
mcm_init_lattice	32	'urandom', 'fcc'	Initial arrangement in which to place the sphere centers before beginning the MMCM iterations. 'urandom' means uniform random placement across the domain (Poisson point field). 'fcc' means face-centered cubic.
mcm_init_perturb_rad	33	Non-negative real number	(Only relevant if 'mcm_init_lattice' = 'fcc') The maximum magnitude by which to randomly perturb the sphere centers after initial placement and before MMCM iterations begin.

Note that for all variables except 'timeout', the program does not care or even ask what units are used, but the unit system *must* be consistent. A common consistent system is millimeters, megapascals, Newtons, and seconds.

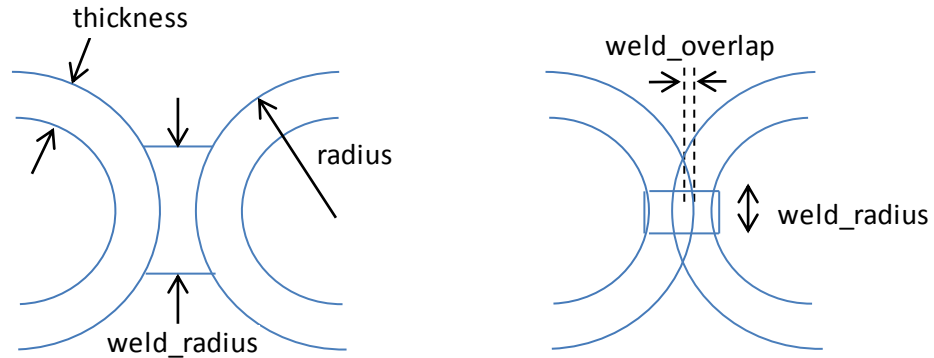


Figure 70: Simplified diagrams demonstrating the geometric meaning behind hollow spheres input parameters. *Left:* with 'weld_type' = 'cylinder'. *Right:* with 'weld_type' = 'overlap'.

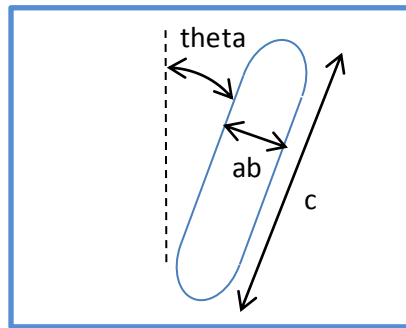


Figure 71: Simplified diagram of the geometric meaning behind general closed-cell input parameters. Note that 'phi' would be the rotation into the plane on the above diagram.

Table 39: Example of working input parameter sets for a general closed-cell and a hollow spheres simulation.

Input Parameter	General Closed-Cell Geometry	Hollow Spheres Geometry
run_part	'all'	'pre+solve'
run_location	'local'	'local'
timeout	4800	9600
name	'Gasar-example'	'HS-example'
geom_type	'PM'	'HS'
domain	[0 2; 0 2; 0 2]	[0 6.25; 0 6.25; 0 6.25]
nsteps_elastic	20	20
nsteps_plastic	10	20
timestepping	'ATS'	'ATS'
mesh_element_size	0.04	0.06
applied_strain	-0.1	0.1
rand_seed	140	121
plot_disp	false	False
base_emedulus	160000	160000

Input Parameter	General Closed-Cell Geometry	Hollow Spheres Geometry
base_ystress	827	172
base_poisson	0.3	0.3
base_pmodulus	500	500
base_kanvinde_alpha	2.6	2.6
n_voids	13	-
ab	0.35	-
c	10	-
abstddev	0.1	-
cstddev	5	-
theta	1.571	-
phi	0	-
thetastddev	0	-
phistddev	0	-
minimum_dist	0	-
radius	-	0.9315
radiusstddev	-	0.0475
thickness	-	0.0832
thicknessstddev	-	0.0125
weld_type	-	'overlap'
weld_overlap	-	0.04
weld_max_length	-	-1
weld_radius	-	0.85
weld_radiusstddev	-	-1
wall_truncate	-	0.9315
mcm_iterations	-	30
mcm_threshold	-	0.01
mcm_init_placement	-	23
mcm_init_lattice	-	'urandom'
mcm_init_perturb_rad	-	-1

A.1.3 Standalone Execution

The first of the methods for executing the Metal Foams Simulator is to run it as a standalone .m file. Open up the `Metal_Foams_Simulator.m` file in an editor, and scroll to the section labeled `USER EDITABLE`, beginning at line 30. After a couple of commented notes, a series of variables is presented. These variables are all of the input parameters as described above. Comments are located to the right of each parameter repeating a basic description of each. Edit the values assigned to each of these variables and run the program by calling the function `Metal_Foams_Simulator` without command line parameters from the MatLab command window. Note that before reading the input variables, the program clears the MatLab memory, so while input variables may be set equal to any valid MatLab formulae, they

may not refer to anything in memory. Do not edit anything below the input variables within the file, as noted by the commented warning messages.

A.1.4 Parametric Execution

The Metal Foams Simulator may also be executed by means of passing command line parameters. The “Param. #” column in Table 38 refers to the order in which parameters must be passed to the Simulator program, and this same order is also reflected and noted in the input variables list within the `Metal_Foams_Simulator.m` file. The number of parameters that need to be passed varies depending upon whether preprocessing inputs are required, and if so, whether the simulation is for an ‘HS’ / ‘CompHS-low’ or a ‘Lotus’ / ‘PM’ / ‘CompHS-high’ type of metal foam. The number of parameters is checked upon launch, and an error code will be returned if the number is incorrect. If any parameters are passed to the Simulator, then it will ignore any input variables within the `Metal_Foams_Simulator.m` file and use the parameters passed to it instead.

This parametric launch method allows a user to execute the Simulator using a wrapper script. Following the UNIX convention, the Simulator returns a single integer parameter as an exit code, equal to 0 if the Simulator completed successfully, and equal to a non-zero positive integer if some error or problem prevented the program from completing. Therefore, a wrapper script may execute the Metal Foams Simulator through a command such as the following:

```
while Metal_Foams_Simulator(param1, param2, ...)  
    [do action for when errors occur, such as repeating  
    with a smaller mesh_element_size value]  
end
```

This parametric method is the recommended method of launching the Metal Foams Simulator, particularly if more than one simulation will be desired. Various unpredictable

problems may occur during execution of a given simulation run, particularly involving being unable to mesh the geometry, which may occur frequently.

A.1.5 Using a Remote Solver

To use a remote solver, it must first be added. Due to the complexity and variability in how different remote solver systems work, this must be added to the code manually; see section A.5.3 Adding a Remote Solver for details on how to do this.

Once a remote solver is added, a slightly different procedure will be required to run the program. The Simulator has no means of monitoring the solving process for its progress and completion, so the program must be run in two separate parts. First, it must be run with 'run_part' = 'pre+solve', which will preprocess on the local machine, and then upload the solver input file (the `.dat` file) to the remote machine and add it to the run queue there. Then, when the solution is complete, run the Simulator with 'run_part' = 'post' to download the solution (the `.por` files) from the remote solver and postprocess on the local machine. Note that the `[name]_internal.mat` file generated during preprocessing will be necessary in order to postprocess the solution file, so it can not be deleted. See section A.2.2 Interrupting and Continuing Execution, for more details on requisite intermediary files.

A.2 User Interface

Once the Metal Foams Simulator starts, there is nothing that the user can do other than cancel a run. However, a significant amount of status information is constantly dumped to the screen in the form of both text and status bars in order to inform the user about the program's progress towards completion. Should the user cancel, or electively only run part of the program, then there are certain requirements for successfully continuing the execution.

A.2.1 Status Information

During execution, status information is displayed both in the form of text scrolling through the command window, as well as one or two status bars on screen, as shown in Figure 72. All text that is output to the log file of any external program, such as any time ADINA is run, is copied to the command window. This gives the most detailed information about what ADINA is currently doing. Further, during the “Solving” phase of the run, this is the only source for status information as ADINA is the only active program at that time. MatLab monitors this output to ensure that it does not remain idle for more than the time specified in the ‘timeout’ input parameter. If an error occurs, the Metal Foams Simulator will pick out any error message from the log file, and display both it and a brief English explanation of the error before exiting.

During all phases of execution, at least one status bar is displayed on screen, showing general information about the progress of the program through preprocessing, solving, or postprocessing. The status bar itself is only an estimate, but text is also displayed above the status bar showing the current task being performed, such as “Applying loads and boundary conditions,” or “Extracting nodal response data from results file (timestep #3).” The title bar of the status window shows which phase of execution the program is in and which the status bar represents. During the preprocessing phase with ‘geom_type’ = ‘HS’ or ‘geom_type’ = ‘CompHS-low’, the program will display a second status bar, showing the current status of the Modified Mechanical Contraction Method iterations.

Each phase of execution—preprocessing, solving, and postprocessing—is treated as a separate process within the Metal Foams Simulator. Should a simulation run be interrupted either by the user or by some other error during any one of these phases, that phase will be left in a corrupted state and cannot be resumed. However, any completed phases are saved, and a partially complete run may be resumed by restarting at the corrupted phase. The essential files needed for resuming each phase are listed in Table 40.

Table 40: Files required for resumption of Simulator runs.

Phase to be Resumed	Files Needed For Resumption	What the Files Are
Preprocessing ('pre')	n/a	n/a
Solving ('solve')	[name]_internal.mat [name].dat	Internal Simulator database ADINA solver input file
Postprocessing ('post')	[name]_internal.mat [name]*.por	Internal Simulator database ADINA results file(s)
Postprocessing graphs ('post_graphs')	[name]_results.mat	Simulator results database

A.3 Interpreting the Results

The Metal Foams Simulator dumps very large amounts of results data upon completion of a run, including data in three different forms: a MatLab database, several graphs, and ADINA results files. Each contains different information, processed to different extents. The below sections describe each results file and how to interpret it.

A.3.1 MATLAB Results File

The most central portrayal of the results is within the MatLab results file, [name]_results.mat. Within this file are about 35 variables representing the stress, strain, Poisson's ratio, and other values at each time step of the simulation, as well as several scalar values as available such as yield stress and elastic modulus. Table 41 lists all of the variables present in this file, their meanings, and the basic theory of how they're calculated.

Table 41: Table of variables present in the Simulator's [name]_results.mat file.

Variable Name	Description	Theory of Calculation
Name	Name of the run	Same as the input parameter
no_cylinders	Number of cylinders created in hollow spheres geometry (between spheres)	Simple count during geometry generation
no_spheres	Number of hollow spheres created in hollow spheres geometry	Simple count during geometry generation
no_voids	Number of voids created in the general closed-cell geometry	Simple count during geometry generation
no_timesteps	Number of timesteps run	Number of timesteps extracted from the .por files
relative_density	Relative density of the material	Total volume of all mesh elements divided by domain volume
s_bilinear_elastic_modulus	Scalar: elastic modulus in the bilinear approximation (engineering)	Secant slope between the origin and the yield point
s_bilinear_hardening_modulus	Scalar: hardening modulus in the bilinear approximation (engineering)	Secant slope between the yield point and the point where the slope increases above that at the yield point
s_bilinear_yield_strain	Scalar: strain at the yield point (engineering)	Equal to s_yield_strain_eng
s_bilinear_yield_stress	Scalar: stress at the yield point (engineering)	Equal to s_yield_stress
s_elastic_modulus_eng	Scalar: elastic modulus (engineering)	Maximum v_zstressstrain_modulus_eng between origin and yield point
s_elastic_modulus_true	Scalar: elastic modulus (true)	Maximum v_zstressstrain_modulus_true between origin and yield
s_elastic_poisson_eng	Scalar: Poisson's ratio in the elastic range (engineering)	Average v_poissons_ratio_eng in elastic range
s_elastic_poisson_true	Scalar: Poisson's ratio in the elastic range (true)	Average v_poissons_ratio_true in elastic range
s_hardening_modulus_eng	Scalar: hardening modulus (engineering)	Minimum v_zstressstrain_modulus_eng between the yield point and the densification point
s_hardening_modulus_true	Scalar: hardening modulus (true)	Minimum v_zstressstrain_modulus_true between the yield point and the densification point
s_plastic_poisson_eng	Scalar: Poisson's ratio in the post-elastic range (engineering)	Average v_poissons_ratio_eng between yield point and densification point
s_plastic_poisson_true	Scalar: Poisson's ratio in the post-elastic range (true)	Average v_poissons_ratio_true between yield point and densification point
s_yield_strain_eng	Scalar: strain at yield point (engineering)	0.1% offset of elastic modulus
s_yield_strain_true	Scalar: strain at yield point (true)	0.1% offset of elastic modulus
s_yield_stress_eng	Scalar: stress at yield point	0.1% offset of elastic modulus
s_yield_stress_true	Scalar: stress at yield point	0.1% offset of elastic modulus
v_force	Vector: force in z-direction	Sum of reactions along top of geometry
v_percent_yielded	Vector: Percent of material which has yielded	Percent of elements which have plastic strain > 0
v_poissons_ratio_eng	Vector: Poisson's ratio between timesteps (engineering)	Average transverse strain divided by z-strain between timesteps
v_poissons_ratio_true	Vector: Poisson's ratio between timesteps (true)	Average transverse strain divided by z-strain between timesteps
v_xstrain_eng	Vector: engineering strain in x direction	Engineering strain at each timestep
v_xstrain_true	Vector: true strain in x direction	True strain at each timestep
v_ystrain_eng	Vector: engineering strain in y direction	Engineering strain at each timestep

Variable Name	Description	Theory of Calculation
v_ystrain_true	Vector: true strain in y direction	True strain at each timestep
v_zstrain_diff_eng	Vector: differential between strain values in z direction (engineering)	Differential of v_zstrain_eng
v_zstrain_diff_true	Vector: differential between strain values in z direction (true)	Differential of v_zstrain_true
v_zstrain_eng	Vector: engineering strain in z direction	Engineering strain at each timestep
v_zstrain_true	Vector: true strain in z direction	True strain at each timestep
v_zstress_eng	Vector: engineering stress in z direction	Engineering strain at each timestep
v_zstress_homogenized	Vector:	
v_zstress_true	Vector: true stress in z direction	True strain at each timestep
v_zstressstrain_modulus_eng	Vector: stress-strain modulus between timesteps (engineering)	Differential of v_zstress_eng divided by v_zstrain_diff_eng
v_zstressstrain_modulus_true	Vector: stress-strain modulus between timesteps (true)	Differential of v_zstress_true divided by v_zstrain_diff_true

A.3.2 Generated Graphs

Based upon the data saved in the [name]_results.mat file, several graphs are generated upon completion of a Simulation run. Just as the Simulator itself doesn't care what units are used in the input parameters, so too are no units listed on the graphs. Each graph is automatically scaled and saved in color in three file formats: .fig (MatLab editable graph), .eps (Encapsulated PostScript), and .tif (Uncompressed Tagged Image File Format). Table 42 contains a description of the content of each of the graphs.

Table 42: Table of results graphs generated by the Simulator.

Graph File Name	Description
[name]_BilinearAndStress_vs_Strain_eng.[ext]	Bilinear approximation z-stress and actual z-stress plotted against z-strain (engineering)
[name]_PercentYielded_vs_Strain_eng.[ext]	Percent of material yielded plotted against z-strain (engineering)
[name]_PoissonsRatio_vs_Strain_eng.[ext]	Poisson's ratio plotted against z-strain (engineering)
[name]_PoissonsRatio_vs_Strain_true.[ext]	Poisson's ratio plotted against z-strain (true)
[name]_Stress_vs_Strain_eng.[ext]	Z-stress plotted against z-strain (engineering)
[name]_Stress_vs_Strain_true.[ext]	Z-stress plotted against z-strain (true)
[name]_StressStrainModulus_vs_Strain_eng.[ext]	Z-stress-strain modulus plotted against z-strain (engineering)
[name]_StressStrainModulus_vs_Strain_true.[ext]	Z-stress-strain modulus plotted against z-strain (true)

A.3.3 ADINA Results Files

The most raw form of the results is contained in the ADINA results files. These are all the files named [name]_#.por, where each .por file contains 20 timesteps worth of data,

restricted to this number in order to ensure that the system upon which the simulation was run will have enough memory available to open each results file. During postprocessing, the Simulator opens each of these files in non-graphics mode and exports raw nodal and elemental data into a text format, which MatLab can then process further. However, the files can also be opened in ADINA's graphical mode by a user in order to explore the results further. For example, after opening the file, the user could generate contour plots of strain, or view stress paths by means of a vector plot. See the ADINA user manual for further details of what may be done with .por files.

A.4 Troubleshooting

There are many things which can go wrong during a run. This section describes common problems and possible resolutions for each.

A.4.1 Index of Exit Codes

The Metal Foams Simulator will issue any of several exit codes, depending upon the success of the run, which program failed, and what exactly the error is. The Simulator does significant error trapping in an attempt to prevent the program from ever crashing without cleaning up and returning an exit code. See Table 43 for a listing of all possible exit codes and their meaning. For all exit codes, a brief description of the meaning of the code will also be printed to the MatLab command line and saved in the file `ERROR.log` in the run directory.

Table 43: Table of exit codes issued by the Metal Foams Simulator, including their meanings and troubleshooting references.

Exit Code	Meaning of Exit Code	For Troubleshooting, See:
0	Successful run; no errors were encountered and the program completed all segments requested.	n/a
1-999	Error in an external program, such as ADINA, sed, etc. Error codes in this range are returned unedited from those issued by the external program, so please see the manual for the given external program as to the meaning of the error code.	The manual pages for the external program.
1000	User-initiated interrupt (i.e. the "Cancel" button was pressed).	n/a
1001	An attempt was made to run the Simulator with parameters, but the wrong number of parameters were passed for the given settings.	Sections A.1.4 and A.1.2 of this user guide.
1002	An input file which was required to run an external program did not exist.	Section A.2.2 of this user guide
1003	An external program encountered an error during execution.	Common problems A.4.2.1 through A.4.2.4, and the manual for the external program.
1004	An external program seems to have frozen during execution; either it failed to create its log file, or the log file wasn't written to for at least the number of seconds set in the 'timeout' input parameter.	Common problems A.4.2.5 through A.4.2.7, and the manual for the external program
1005	During preprocessing, ADINA failed to generate the NASTRAN file required by the Simulator in order to parse nodal IDs for load and boundary condition application.	ADINA logs for details of cause, and ADINA manual for fixes.
1006	During postprocessing, ADINA failed to generate the .txt data output files required by the Simulator in order to import any results data.	Common problems A.4.2.8.
1007	An invalid 'run_location' input parameter was passed; either during solving or post-processing, the Simulator couldn't figure out how to post a job or retrieve results.	Sections A.1.5 and A.5.2 of this user guide.
1008	A required database file (either [name]_internal.mat or [name]_results.mat) could not be found during either solving or postprocessing.	Section A.2.2 of this user guide.
1009	During preprocessing of the hollow spheres geometry, the Modified Mechanical Contraction Method was unable to generate a valid geometry (it reached a maximum number of iterations, based upon the 'timeout' input variable, while trying to eliminate contacts between spheres).	Common problems A.4.2.9.
1010	The directory associated with the 'name' input parameter does not exist, and the user did not request preprocessing to be performed.	Section A.2.2 of this user guide.
1011	During preprocessing, ADINA must not have meshed the full body, as there are no nodes present on at least one entire face of the geometry.	Common problems A.4.2.10.
1012	For the preprocessing of hollow spheres foams, an invalid initial lattice was passed in the 'mcm_init_lattice' input parameter.	Section A.1.2 of this user guide.
1013	An external program looks like it completed successfully (it printed a defined exit trigger to its log file), but it didn't exit and 'kill -9' commands failed to kill it.	Manual for the external program.

A.4.2 Common Problems

Below are frequent problems which the author of the Metal Foams Simulator has encountered but has been unable to correct in the program's code.

A.4.2.1 Exit code 1003: Error during execution of external program scp.

This program is only run if a remote solver is selected. Check the logs for the `scp` program (see the `logs` subdirectory), but it probably means that either the internet connection is down or the automatic login details have changed. Check the internet connection for the local machine as well as for the remote machine being run upon.

If a login error occurred, it is likely that either the local private key has been changed or the public key on the remote machine has been deleted (such as if the remote home directory was wiped). See section A.5.3 Adding a Remote Solver for details on how to use the `ssh-keygen` and `ssh-copy-id` commands to reestablish automatic login.

A.4.2.2 Exit code 1003: “UVAL” error during execution of ADINA.

This error occurs about halfway through a meshing process and seems to have something to do with the geometry generated and the Delauney meshing algorithm that the Metal Foams Simulator uses. The author has been unable to pin down the cause of the problem, but it only seems to occur on very complicated geometries. It doesn't seem to be an inherent problem with any particular settings, so just pick a different random seed and try again.

A.4.2.3 Exit code 1003: “Overdistorted elements” error during execution of ADINA.

This error is frequently seen for hollow spheres geometries using `'weld_type' = 'overlap'`. It seems to have to do with particularly slender elements which get created in the region between where spheres just begin to overlap and where the cylinder geometry is created. Experiment with the `weld_radius` value to try and correct this. Values between 0.75 and 0.85 seem to work best. If this error still continues, change the `weld_type` to the `'cylinder'` algorithm, which, while less physically accurate, meshes much more easily.

A.4.2.4 Exit code 1003: “Unable to mesh” error during execution of ADINA.

This is by far the most common error observed during Simulator runs. It means that the mesh is too coarse and ADINA’s mesher algorithm was not able to automatically refine problem areas enough to create any mesh. The `mesh_element_size` input parameter probably needs to be reduced. A good rule of thumb seems to be that elements must be at most 70% of the shell thickness in a hollow spheres geometry, or half the diameter of a void in a general closed-cell geometry. If the `mesh_element_size` is very close to its maximum, then it may also work to simply try again with a different random seed.

A.4.2.5 Exit code 1004: Timeout during ADINA solving.

During solving, there are three possibilities: (1) the ‘timeout’ is too short to run a normal single iteration, (2) one particular iteration took an unusually long time, or (3) ADINA actually froze. In the author’s experience, (3) is extremely rare. Experience suggests that setting the ‘timeout’ to be roughly 50% larger than the time it takes to run a single normal iteration works well and captures any unusually long iterations (this is wall clock time, so what that time is depends on the number of elements and the particular machine being run upon). Rerun the ‘solve’ segment with a longer ‘timeout’.

A.4.2.6 Exit code 1004: Timeout during ADINA postprocessing.

Either the ‘timeout’ is too short for ADINA to load a single .por file and then export its raw data, or ADINA actually froze. In the author’s experience, the former is far more common. Fortunately, when this error occurs, it’s in the very beginning of a postprocessing process, so just rerun the ‘post’ segment of the run with a longer ‘timeout’.

A.4.2.7 Exit code 1004: Timeout during execution of external program `scp`.

This program is only run if a remote solver is selected. Check the logs for the scp program (see the 'logs' subdirectory), but there are two possible reasons for this:

- 1) SSH could not automatically login, and appeared to "freeze" since it was expecting the user to type a password. In order for the Simulator's remote solver option to work, it *must* be able to login automatically via SSH, and scp is simply a program that copies a file over an SSH connection. See section A.5.3 Adding a Remote Solver for details of how to use the `ssh-keygen` and `ssh-copy-id` programs to enable automatic login.
- 2) Your internet connection was too slow to transfer a file before the 'timeout' was reached. Either find a faster internet connection, or increase the 'timeout' input parameter.

A.4.2.8 Exit code 1006: ADINA fails to generate .txt postprocessing files.

This probably means that the hard drive is full. ADINA 8.5 oddly does not throw an error if the hard drive of the machine it's being run upon fills up during a solver run, nor does it throw an error when opening an incomplete `.por` file for postprocessing. However, the next files to be created by the Metal Foams Simulator are these postprocessing `.txt` files, which will not be successfully created if the hard drive is full. There shouldn't be any other reason for this error.

A.4.2.9 Exit code 1009: Hollow spheres geometry generation timeout.

If there are too many spheres to fit into the domain given, this error will be thrown. Reduce the 'mcm_init_placement' value and try again.

A.4.2.10 Exit code 1011: The Simulator believes that ADINA did not mesh a full body.

The Simulator did not find any nodes on at least one of the six sides of the domain, probably meaning that ADINA did not mesh the full body. In a hollow spheres geometry, this can happen if there are either too few spheres, which then leaves at least one lone sphere unconnected with the rest of the geometry, or if one sphere, usually located in a corner, ends up unconnected to the rest of the body. Increase the 'mcm_init_placement' value and try again.

In a general closed-cell model, particularly with no 'minimum_dist' set, this can mean that a couple of voids have completely cut off a corner of the geometry from the rest of the specimen. Try again with a different random seed, or possibly with fewer 'no_voids' or a non-zero 'minimum_dist'.

A.5 Editing the Code

The code for the Metal Foams Simulator is extensively commented. However, the overall coding philosophy is harder to glean from simply reading comments. This section attempts to convey those overarching conventions, as well as to address a few specific details which may require more explanation than is present in the comments. The latter includes details about adding a new remote solver, how the status tracking system (status bars, etc.) works, and how the interface between MatLab and ADINA works.

A.5.1 Coding Conventions

Comments:

- *Long comments:* Immediately above every function declaration is located a one or two sentence description of what that function does and how it goes about doing it. Similar short descriptions are also located immediately above major or particularly complex loops or conditional statements.

- *Short comments:* If a particular line is unusually complicated or seems it would difficult to follow, then at the end of that line, a comment is added with a phrase or sentence explaining what the line does.

Variable names:

All variables are entirely lower-case.

- *Major variables:* Major variables, such as input parameters and those passed between functions are given descriptive names, entirely lower case, with individual words separated by underscores.
- *Counting variables:* Variables that serve no purpose other than counting, particularly those used in a loop, are given single letter names such as 'i', 'j', 'k'.
- *Temporary variables:* Other temporary variables are given a prefix of 'temp_'. No temporary variables are ever passed to other functions.
- *Results variables:* In order to keep the [name]_results.mat database as human-readable as possible, variables expressing simulation results follow the same conventions as major variables, but also add a prefix of 's_' for scalar values and 'v_' for vectors.

Function names: (see also section A.5.2 Code Structure)

All function names have a capitalized first letter (at least).

- *Main function:* The main function is named `Metal_Foams_Simulator`, the same as the file name as per MatLab's conventions.
- *Segment master functions:* These are given the full names of the segment, such as `Preprocess_part*()`, `Solve()`, and `Postprocess()`.

- *Segment subfunctions*: To keep these organized, an abbreviated name of the segment is prefixed to these function names: `Pre_*()`, `Sol_*()`, and `Post_*()`.
- *Helper functions*: These are prefixed as `Help_*()`.

A.5.2 Code Structure

The general philosophy here is to have no one function be longer than about 150 lines, and to have a tiered structure. Higher tiers mostly manage data and call subfunctions; they do very little processing themselves. Except for a few helper functions in common to all segments, functions are kept isolated to pertaining to only one of the three code segments (preprocessing, solving, postprocessing). Below is a more detailed description:

- *Main function* (`Metal_Foams_Simulator()`): The main function is named the same as the file name, as per MatLab conventions. This function does no data processing at all. It only stores the input parameters to appropriate variable names and then calls the appropriate segment master functions.
- *Segment master functions* (`Preprocess_part*()`, `Solve()`, `Postprocess()`, `Postprocess_graphs()`): These are the functions that run a particular segment of the code from beginning to end. They do some data processing, but mostly call subfunctions. Note that preprocessing actually has three master functions, of which only two are called. First, either `Preprocess_part1_HS()` or `Preprocess_part1_CC()` is called, depending upon whether the hollow spheres geometry or general closed-cell geometry was selected. Then, `Preprocess_part2()` is called.

- *Segment subfunctions* (`Pre_*()`, `Sol_*()`, `Post_*()`): Performing the actual data processing work, these various functions are the meat of the program.
- *Helper functions* (`Help_*()`): These functions may be called by any function in any segment, and perform various helper tasks, such as cleanup tasks upon an exit or error, or providing a framework for running external programs.

A.5.3 Adding a Remote Solver

Remote machines all work differently, particularly if it has a job queue, so it is far more practical to require the user to write a simple block of code specific to the remote machine that he or she wishes to use. Further, automatic login will need to be set up for the remote machine, as there is no practical way to forward an interactive password prompt from an external program through MatLab.

Two functions will need to be written: one which copies input data to the remote machine and runs the solver on that machine, and the other which copies output (postprocessing) data from the remote machine upon completion of a run. Both of these functions are located at the end of the Metal Foams Simulator code, and are named `Sol_remote#()` and `Post_remote#()`, respectively, where the '#' should be replaced with the numerical label of the remote machine. One example (`Sol_remote1()` / `Post_remote1()`) is provided, and templates for four further remote machines are already created in the file as labels 2, 3, 4, and 5. One label will be used for each remote machine.

A.5.3.1 `Sol_remote#()`

```
exitcode = Sol_remote#(name)
```

Taking the run name as its only argument, and expected to return an "exitcode" value, this is the function that copies all necessary data to the remote machine and then initiates the

solve operation. At the very least, it must copy the `[name].dat` file, and then somehow run the ADINA solver executable. Depending upon the specific nature of the remote system, further files may be necessary in order to add the solve operation to a job queue, for example.

The author recommends that `scp -v` and `ssh -v` programs be used if at all possible, as they are the most secure and stable methods available for copying files and running commands. Note that the `-v` switch tells the program to run in verbose mode, outputting all data about what it's doing to the screen (or, more preferably, to a log file if the program is run piped to a file). Screen output may be piped to a file by adding `> [filename].log` to the end of a command. Please see the manuals for those two programs, or any other program deemed more appropriate, for specific instructions on how their commands should be run.

External programs can be run in either of two ways: directly using MatLab's `unix()` function, or with the aid of the `Help_run_external_program()` function in the Metal Foams Simulator. The latter provides a framework which first checks for the existence of a required input file and then executes the external command. As the command runs, it monitors the progress of that external command by watching a log file, exiting upon a successful completion, or throwing an error if either the program times out or displays a line that begins with the text 'Error' or 'Alert'. This helper function therefore takes care of tracking exit codes and looking for any errors that may occur, allowing for more effective automation of the Simulator. MatLab's `unix()` function would execute the same command, but without any of the above added benefits.

At the end of the function, an `exitcode = 0;` line should be present, which returns the code saying that this function has completed successfully.

A.5.3.2 Post_remote# ()

```
exitcode = Post_remote#(name)
```

Like Sol_remote# (), this function takes only the run name, and is expected to return an exitcode. The function should not do anything other than copy the results data back, and possibly do any cleanup which the remote solver machine requires. It is also recommended that the function copy back any log files to help with any necessary debugging. As for Sol_remote# (), the use of the scp -v and ssh -v external programs is suggested.

At the end of the function, an exitcode = 0; line should be present, which returns the code signaling that this function has completed successfully.

A.5.3.3 Automatic Login

As MatLab is not capable of interfacing with an interactive program, login to the remote machine must somehow be automatic. One method of doing this is to include the password in plaintext within the command. However, the suggested method is by using a public key / private key login. If using the ssh and scp programs, this is accomplished by the user manually running the following commands within their user account *once* (do not include them in the Simulator code):

```
ssh-keygen -A
```

```
ssh-copy-id [remote_username]@[address_of_remote_machine]
```

The first command will generate a public-private key pair, and the second will copy it to the account on the remote machine which the Simulator should automatically log into. This is a completely secure method. Please see the manuals for each of those programs for further details on advanced options.

A.5.4 Status Tracking System

The status tracking system, consisting primarily of the various status bars displayed throughout execution, is highly integrated within the code for the Metal Foams Simulator and therefore worth a special mention. These status bars are based upon MatLab's `waitbar()` function. In order to track their handles, some limited data is stored in global variables, or 'application data'.

At the beginning of each segment master function, for preprocessing, solving, and postprocessing, status bars are created using a `waitbar()` command. The handle to that `waitbar` is then stored as application data using the function `setappdata(0, 'wbar', [handle])`, so that it can be accessed and updated by other functions. Further, a 'Cancel' button is added, which is set to run the command `setappdata(0, 'exitcode', 1000)` upon being pressed. That is, it sets a global 'exitcode' variable to the user-initiated abort code.

There are then several spots within various subfunctions or loops which update the text and completion progress for that status bar by using the handle listed in the global variable. When any update occurs, the code also checks that global 'exitcode' variable, and initiates clean abort procedures by running the `Help_abort()` function if it find that variable set to a value of '1000'.

Upon the completion of segment master functions, the active status bars are deleted and their handles cleared from global variables. Note that because the `waitbars` have 'Cancel' buttons, they must be *deleted* and cannot simply be closed, or they will be a memory leak until MatLab is restarted. The `Help_abort()` function clears every global variable and runs an additional `delete()` function to ensure that all `waitbars` are removed.

A.5.5 ADINA Interface

The interface between MatLab and ADINA operates based upon writing script files using MatLab and then running them as the input to the ADINA external program. Data is retrieved by making ADINA export tab-delimited raw results data as a file, and then importing that results file into MatLab. When ADINA is run, the `Help_run_external_program()` function is used, which always sets ADINA to output all of its command line output to a log file. It also monitors that log file, displaying all text to the screen and monitoring it for errors or successful completions.

Most operations performed in input files, such as creating spheres, Boolean geometry operations, meshing, and outputting tab-delimited results data, should be available in any finite element analysis program. However, a special workaround was necessary for the retrieval of relative density data. For this only, the `Help_run_external_program()` function is *not* used, and ADINA is run directly, with its output piped to the `sed` external program. The input file tells ADINA to calculate the total volume of all meshed elements in the geometry, and `sed` searches for the resultant text in the output, reporting that number directly back to the Simulator.

BIBLIOGRAPHY

- Adler, J., G. Standke, and G. Stephani. "Sintered open-celled metal foams made by replication method - manufacturing and properties on example of 316L stainless steel foams." *Proceedings of the Symposium on Cellular Metals and Polymers (CMAp)*. Fürth, Germany: Deutsche Forschungsgemeinschaft (DFG), 2004. 89-92.
- Andrews, E. W., G. Gioux, P. Onck, and L. J. Gibson. "Size effects in ductile cellular solids. Part II: experimental results." *International Journal of Mechanical Sciences* 43 (2001): 701-713.
- Angel, S., W. Bleck, and P.-F. Scholz. "SlipReactionFoamSintering (SRFS) - process: production, parameters, characterisation." *Proceedings of the Symposium on Cellular Metals and Polymers (CMAp)*. Fürth, Germany: Deutsche Forschungsgemeinschaft (DFG), 2004. 85-88.
- Ashby, M. F., A. G. Evans, N. A. Fleck, L. J. Gibson, J. W. Hutchinson, and H. N. G. Wadley. *Metal Foams: A Design Guide*. Boston, MA: Butterworth Hamilton, 2000.
- Banhart, J. "Manufacture, Characterisation, and Applications of Cellular Metals and Metal Foams." *Progress in Materials Science* 46 (2001): 559-632.
- Banhart, J., and H. Seeliger. "Aluminium foam sandwich panels: Manufacture, metallurgy and applications." *Advanced Engineering Materials* 10 (2008): 93-802.
- Bao, H., and B. Han. "Transmission loss of metallic foams for the local resonance." *3rd International Conference on Bioinformatics and Biomedical Engineering, iCBBE 2009*. Beijing, 2009. 5163700.
- Brown, J. A., L. J. Vendra, and A. Rabiei. "Bending properties of Al-steel and steel-steel composite metal foams." *Metallurgical and Materials Transactions A Online*, no. 1 July 2010 (2010).
- Cardoso, A., and B. Oliveira. "Study of the use of metallic foam in a vehicle for an energy economy racing circuit." *Materialwissenschaft und Werkstofftechnik* 41, no. 5 (2010): 257-264.
- Chi, W. M., A. M. Kanvinde, and G. G. Deierlein. "Prediction of ductile fracture in steel connections using SMCS criterion." *Journal of Engineering Mechanics*, 2006: 171-181.
- Coquard, R., D. Rochais, and D. Baillis. "Conductive and radiative heat transfer in ceramic and metal foams at fire temperatures." Edited by K. G. Wakili. *Fire Technology*, no. Special issue: "Materials in Fire" (2010).
- Daxner, T., R. W. Tomas, and R. D. Bitsche. "Mechanics of semi-expanded hollow sphere foams." *MetFoam 2007: Proceedings of the 5th International Conference on Porous Metals and Metallic Foams*. Montreal, Canada, 2007. 169-172.
- Degischer, H.-P., and B. Kriszt. *Handbook of Cellular Metals: Production, Processing, and Applications*. Weinheim, Germany: Wiley-VCH, 2002.

- Deshpande, V., and N. A. Fleck. "Isotropic constitutive models for metallic foams." *Journal of the Mechanics and Physics of Solids* 48 (2000): 1253-1283.
- Fallet, A., L. Salvo, and Y. Brechet. "Metallic Hollow Spheres Foam: Structure and Mechanics." *Proc. of the 5th Int. Conf. on Porous Metals and Metallic Foams*. Montreal, Canada: IMI (Canada), 2007. 343-346.
- Fathy, A., A. Ahmed, and H. Morgan. "Characterization and optimization of steel foam produced by slip casting process." *MetFoam 2007: Proceedings of the 5th International Conference on Porous Metals and Metallic Foams*. Montreal, Canada, 2007. 161-164.
- Fazekas, A., R. Dendievel, L. Salvo, and Y. Brechet. "Effect of microstructural topology upon the stiffness and strength of 2D cellular structures." *International Journal of Mechanical Sciences* 44 (2002): 2047-2066.
- Franeck, J., and G. Landgraf. "Determination of linear and non-linear mechanical properties of sintered hollow-sphere structures." *Proceedings of the Symposium on Cellular Metals and Polymers (CMAp)*. Fürth, Germany: Deutsche Forschungsgemeinschaft (DFG), 2004. 139-142.
- Friedl, O., C. Motz, H. Peterlik, S. Puchegger, N. Reger, and R. Pippan. "Experimental investigation of mechanical properties of metallic hollow sphere structures." *Metallurgical and Materials Transactions B* 39, no. 1 (2007): 135-146.
- Gao, Z. Y., T. X. Yu, and D. Karagiozova. "Finite element simulations on the mechanical properties of MHS materials." *Acta Mech Sin* 23 (2007): 65-75.
- Gao, Z. Y., T. X. Yu, and H. Zhao. "Mechanical behavior of metallic hollow sphere materials: experimental study." *Journal of Aerospace Engineering* 21, no. 4 (2008): 206-216.
- Gasser, S., F. Paun, and Y. Brechet. "Finite elements computation for the elastic properties of a regular stacking of hollow spheres." *Materials Science and Engineering A* 379 (2004): 240-244.
- Gauthier, M. "Structure and properties of open-cell 316L stainless steel foams produced by a powder metallurgy-based process." *MetFoam 2007: Proceedings of the 5th International Conference on Porous Metals and Metallic Foams*. Montreal, Canada, 2007. 149-152.
- Gibson, M. F., and L. J. Ashby. *Cellular Solids: Structure and Properties*. London: Oxfordshire Press, 1997.
- Goehler, Dr. Hartmut, interview by Dr. Sanjay R. Arwade. *Foam Order* (12 15, 2010).
- Gohler, H., P. Lothman, U. Waag, H. Schneidereit, and E. Bernhard. "Manufacture and properties of hollow sphere structures in sound absorbing applications." *Cellular Metals and Metal Foaming Technology (a.k.a. MetFoam 2001)*. Germany: MIT Verlag, 2001. 391-396.

- Hanssen, A., O. Hopperstad, M. Langseth, and H. Ilstad. "Validation of constitutive models applicable to aluminium foams." *International Journal of Mechanical Sciences* 44 (2002): 359-406.
- Hipke, Thomas, interview by Stephan Szyniszewski. *Professor, Fraunhofer Institute in Chemnitz* (2011).
- Hoffman, Gernot. *Distance Between Line Segments*. July 11, 2005. <http://www.fh-ohmden.de/~hoffmann/xsegdist03072004.pdf> (accessed July 1, 2011).
- Hyun, S.-K., J.-S. Park, M. Tane, and H. Nakajima. "Fabrication of lotus-type porous metals by continuous zone melting and continuous casting techniques." *MetFoam 2005: 4th International Conference on Porous Metals and Metal Foaming Technology*. Kyoto, Japan: Japan Institute of Metals (JIMIC-4), 2005.
- Ikeda, T., T. Aoki, and H. Nakajima. "Fabrication of lotus-type porous stainless steel by continuous zone melting technique and mechanical property." *Metallurgical and Materials Transactions A* 37A (2007): 77-86.
- Kansal, A. R., S. Torquato, and F. H. Stillinger. "Computer generation of dense polydisperse sphere packings." *The Journal of Chemical Physics* 117, no. 18 (2002): 8212-8218.
- Karagiozova, D., T. X. Yu, and Z. Y. Gao. "Modeling of MHS cellular solid in large strain." *International Journal of Mechanical Sciences* 48 (2006): 1273-1286.
- Karagiozova, D., T. X. Yu, and Z. Y. Gao. "Stress-strain relationship for metal hollow sphere materials as a function of their relative density." *Transactions of the ASME* 74 (2007): 898-907.
- Kari, S., H. Bergerm, R. Rodriguez-Ramos, and U. Gabbert. "Computational evaluation of effective material properties of composites reinforced by randomly distributed spherical particles." *Composite Structures* 77 (2007): 223-231.
- Kepets, M., T. J. Lu, and A. P. Dowling. "Modeling of the role of defects in sintered FeCrAlY foams." *Acta Mech Sin* 23 (2007): 511-529.
- Khan, A. *Continuum theory of plasticity*. New York City: Wiley, 1995.
- Khayargoli, P., V. Loya, L. P. Lefebvre, and M. Medraj. "The impact of microstructure on the permeability of metal foams." *CSME 2004 Forum*, 2004: 220-228.
- Kostornov, A. G., O. V. Kirichenko, N. P. Brodnikovskii, Y. A. Guslienko, and V. N. Kli menko. "High-porous materials made from alloy steel fibers: production, structure, and mechanical properties." *Powder Metallurgy and Metal Ceramics* 47, no. 5-6 (2008): 295-298.
- Kremer, K., A. Liszkiewicz, and J. D. Adkins. *Development of Steel Foam Materials and Structures*. Government Report, Delaware Center for Manufacturing and Advanced Materials, Fraunhofer USA, Washington, D.C.: US DOE and AISI, 2004.

- Krupp, U., et al. "Development of a standard for compression testing of cellular materials." *MetFoam 2007: Proceedings of the 5th International Conference on Porous Metals and Metallic Foams*. Montreal, Canada, 2007. 407-410.
- Krupp, Ulrich, interview by Brooks H. Smith. *MetFoam Standardization* (September 20, 2011).
- Kujime, T., S.-K. Hyun, and H. Nakajima. "Mechanical properties of lotus-type porous carbon-steel by continuous zone melting." *MetFoam 2005: 4th International Conference on Porous Metals and Metal Foaming Technology*. Kyoto, Japan: Japan Institute of Metals (JIMIC-4), 2005. 525-528.
- Kwon, Y. W., R. E. Cooke, and C. Park. "Representative unit-cell models for open-cell metal foams with or without elastic filler." *Materials Science and Engineering A* 343 (2002): 63-70.
- Lee, B.-K., I. Jeon, and K.-J. Kang. "Compressive characteristics of WBK truss cores." *MetFoam 2007: Proceedings of the 5th International Conference on Porous Metals and Metallic Foams*. Montreal, Canada, 2007. 177-180.
- Lefebvre, L., Banhart, J., Dunand, D. "Porous Metals and Metallic Foams: Current Status and Recent Developments." *Advanced Engineering Materials* 10 (2008): 775-787.
- Levine, B. "A new era in porous metals: Applications in orthopaedics." *Advanced Engineering Materials* 10 (2008): 788-792.
- Lim, T.-J., B. Smith, and D. L. McDowell. "Behavior of a random hollow sphere metal foam." *Acta Materiala* 50 (2002): 2867-2879.
- Losito, O., Barlettam D., and V. Dimiccolim. "A wide-frequency model of metal foam for shielding applications." *IEEE Transactions on Electromagnetic Compatibility* 52 (2010): 75-81.
- Lu, T., and C. Chen. "Thermal transport and fire retardance properties of cellular aluminium alloys." *Acta Materiala* 47 (1999): 1469-1485.
- Miller, R. E. "A continuum plasticity model for the constitutive and indentation behaviour of foamed metals." *International Journal of Mechanical Sciences* 42 (2000): 729-754.
- Muriel, J., A. Sanchez Roa, W. Barona Mercado, and H. Sanchez Sthepa. "Steel and grey iron foam by powder metallurgical synthesis." *Suplemento de la Revista Latinoamericana de Metalurgia y Materiales* S1, no. 4 (2009): 1435-1440.
- Nakajima, H., T. Ikeda, and S. K. Hyun. "Fabrication of lotus-type porous metals and physical properties." *Cellular Metals: Manufacture, Properties, Applications: 3rd International Conference on Cellular Metals and Metal Foaming Technology*. Berlin, Germany: Metall Innovation Technologie MIT, 2003. 191-203.

- Neugebauer, R., T. Hipke, J. Hohlfeld, and R. Thümmeler. "Metal foam as a combination of lightweight engineering and damping." Edited by R. F. Singer, C. Körner, V. Altstädt, & H. and Münstedt. *Cellular Metals and Polymers*. Fürth, Germany: Deutsche Forschungsgemeinschaft (DFG), 2004. 13-18.
- Neville, B. P., and A. Rabiei. "Composite metal foams processed through powder metallurgy." *Materials and Design* 29 (2008): 388-396.
- Nishiyabu, K., S. Matsuzaki, and S. Tanaka. "Effectiveness of micro porous metal metal components with functionally graded structures." *MetFoam 2005: 4th International Conference on Porous Metals and Metal Foaming Technology*. Kyoto, Japan: Japan Institute of Metal (JIMIC-4), 2005. 325-328.
- Oechsner, A. *Multifunctional Metallic Hollow Sphere Structures : Manufacturing, Properties and Application*. Springer, 2009.
- Oechsner, A. "Numerical Simulation of Thermal and Mechanical Properties of Sintered Perforated Hollow Sphere Structures (PHSS)." *AIP Conference Proceedings* 1177 (2009): 16-30.
- Park, C., and S. R. Nutt. "Anisotropy and strain localization in steel foam." *Materials Science and Engineering A* A299 (2001): 68-74.
- Park, C., and S. R. Nutt. "PM synthesis and properties of steel foams." *Materials Science and Engineering A* A288 (2000): 111-118.
- Park, C., and S. R. Nutt. "Strain rate sensitivity and defects in steel foam." *Materials Science and Engineering A* A323 (2002): 358-366.
- Rabiei, A., and L. J. Vendra. "A comparison of composite metal foam's properties and other comparable metal foams." *Materials Letters* 63 (2009): 533-536.
- Reisgen, U., S. Olschok, and S. Longerich. "Laser beam welding of open-porous metallic foams for application in cooling structures of combined cycle power plants." *Journal of Engineering for Gas Turbines and Power* 132, no. 5 (2010): 1-5.
- Reyes, A. "Constitutive modeling of aluminum foam including fracture and statistical variation of density." *European Journal of Mechanics A / Solids* 22 (2003): 815-835.
- Sanders, W. S. *Mechanical behavior of closed-cell and hollow-sphere metallic foams*. D.Sc. Thesis, Boston: Massachusetts Institute of Technology, 2002.
- Sanders, W. S., and L. J. Gibson. "Mechanics of BCC and FCC hollow-sphere foams." *Materials Science and Engineering A* A352 (2002): 150-161.
- Shapovalov, V., and L. Boyko. "Gasar - a new class of porous materials: syntheses, structure, properties, and potential applications." *2nd International Conference on Cellular Metals and Metal Foaming Technology*. Bremen, Germany: Metall Innovation Technologie MIT, 2001. 201-208.

- Shirzadi, A., Y. Zhu, and H. Bhadeshia. "Joining ceramics to metals using metallic foams." *Materials Science and Engineering A* 496 (2008): 501-506.
- Speich, M., W. Rimkus, M. Merkel, and A. Oechsner. "Large deformation of metallic hollow spheres." *Materials Science Forum* 623 (2009): 105-117.
- Stephani, G., et al. "Iron-based cellular structures - status and prospects." *MetFoam 2005: 4th International Conference on Porous Metals and Metal Foaming Technology*. Kyoto, Japan: Japan Institute of Metals (JIMIC-4), 2005.
- Tang, H. P., J. L. Zhu, J. Y. Wang, Y. Ge, and C. Li. "Sound absorption characters of metal fibrous porous foams." *MetFoam 2007: Proceedings of the 5th International Conference on Porous Metals and Metallic Foams*. Montreal, Canada, 2007. 181-183.
- Torquato, S. *Random Heterogeneous Materials: Microstructure and Macroscopic Properties*. New York City: Springer, 2002.
- Tuchinsky, L. "Novel fabrication technology for metal foams." *Journal of Advanced Materials* 37, no. 3 (2007): 60-65.
- Verdooren, A., H. M. Chan, J. L. Grenestedt, M. P. Harmer, and H. S. Caram. "Fabrication of low-density ferrous metallic foams by reduction of ceramic foam precursors." *Journal of Materials Science* 40 (2005a): 4333-4339.
- Verdooren, A., H. M. Chan, J. L. Grenestedt, M. P. Harmer, and H. S. Caram. "Fabrication of low-density ferrous metallic foams by reduction of chemically bonded ceramic foams." *Journal of the American Chemical Society* 89, no. 10 (2005b): 3101-3106.
- Weise, J., G. B. D. Silva, and N. Salk. "Production and properties of syntactic steel and iron foams with micro glass bubbles." 2010.
- Wouterse, A., and A. P. Philipse. "Geometrical cluster ensemble analysis of random sphere packings." *The Journal of Chemical Physics* 125, no. 19 (2006): 194709-194719.
- Xu, S., M. Bourham, and A. Rabiei. "A novel ultra-light structure for radiation shielding." *Materials and Design* 31 (2010): 2140-2146.
- Zhao, C. Y., T. J. Lu, H. P. Hodson, and J. D. Jackson. "The temperature dependence of effective thermal conductivity of open-celled steel alloy foams." *Materials Science and Engineering A* 267 (2004): 123-131.